Alma Mater Studiorum – Università di Bologna

DOTTORATO DI RICERCA IN

Ingegneria Elettronica, Telecomunicazioni e Tecnologie dell'Informazione

Ciclo XXXI

Settore Concorsuale: 09/F1
Settore Scientifico Disciplinare: ING-INF/02

DESIGN OF NOVEL SYSTEMS FOR POSITION INDEPENDENT ENERGY AND DATA TRANSFER

Presentata da: **ALEX PACINI**

Coordinatore Dottorato:
Prof. Alessandra Costanzo

Supervisore:
Prof. Alessandra Costanzo

Co-Supervisori:
Prof. Franco Mastri
Ing. Diego Masotti

Esame Finale Anno 2019

This page was intentionally left blank.

Abstract

This thesis proposes a theoretical and experimental framework for the modeling, analysis and design of a complete energy and data transfer system, which provides constant performances independently of the receiver position.

The energy transfer is considered for industrial scenarios, which require high powers and efficiencies, as well as for biomedical implants, which have high distances but do not require necessarily high efficiency. In the former, the method provides a constant received voltage, independent of the load and position in one direction of the receiver and without any feedback loop. It is based on a geometrical optimization of an inductive link composed of three coils and on resonant inverters and rectifier, respectively in class EF and E, operating at 6.78 MHz. Furthermore, it enables to passively localize the receiver, without requiring its involvement. In the latter, the proposed solution enables to power small implants without knowing their orientation.

The high throughput data transfer is intended for the industrial scenario, where it integrates in a single system with the power link and enables every part to connect and cooperate with each other. It employs consumer hardware and provides bandwidths of over 100Mb/s, independently of the position and with high resistance to interference.

This page was intentionally left blank.

Sommario

Questa tesi propone un quadro teorico e pratico per la modellazione, l'analisi e il progetto di un sistema completo per il trasferimento di energia e dati indipendente dalla posizione del ricevitore.

Il trasferimento di energia è trattato sia per scenari industriali, che richiedono alte potenze ed efficienze, sia per quelli di impianti biomedicali, che presentano distanze significative ma non necessitano di particolari efficienze. Nel primo caso, il metodo proposto consente una tensione al ricevitore costante, indipendente dalla posizione, in una direzione, e dal carico del ricevitore, senza nessuna necessità di controllo in retroazione. Si basa sulla ottimizzazione geometrica di un link induttivo composto da tre spire e su inverter e rettificatore risonanti, in classe EF ed E, rispettivamente, funzionanti a 6.78 MHz. Consente inoltre di localizzare il ricevitore in maniera passiva e indipendente dal ricevitore. Nel secondo caso, la soluzione proposta consente di alimentare dispositivi impiantabili indipendentemente dalla loro rotazione.

Il trasferimento dei dati a banda larga si inserisce nello scenario industriale, integrandosi in un unico sistema di potenza e dati, con la possibilità anche di interagire tra loro. Attraverso l'uso di hardware di consumo, consente bande superiori a 100Mb/s, indipendentemente dalla posizione, con ottima resistenza alle interferenze.

This page was intentionally left blank.

Contents

Concept Map

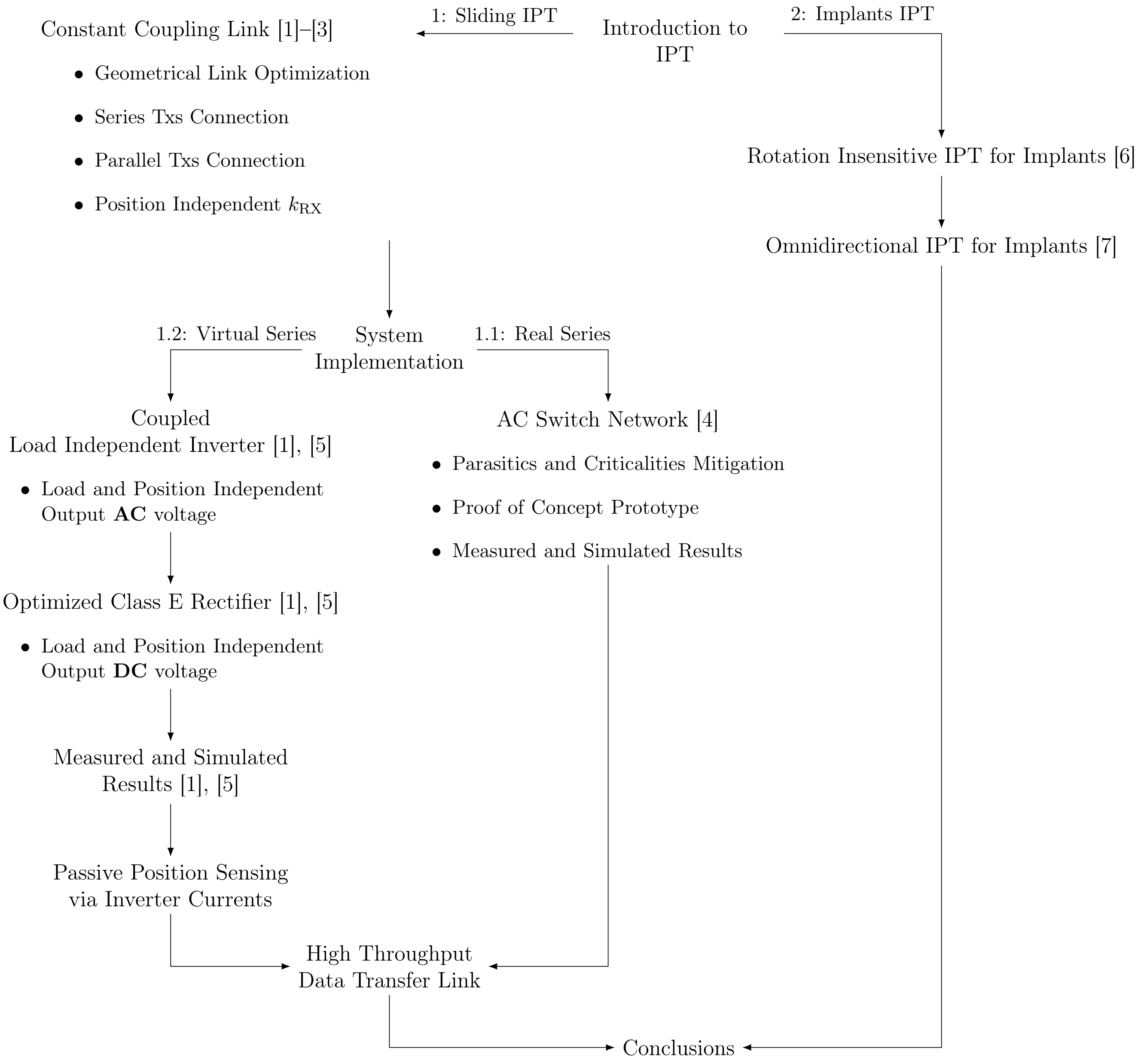
Introduction to IPT
1: Sliding IPT
2: Implants IPT
Constant Coupling Link [1]–[3]
• Geometrical Link Optimization
• Series Txs Connection
• Parallel Txs Connection
• Position Independent k_{RX}
Rotation Insensitive IPT for Implants [6]
Omnidirectional IPT for Implants [7]
System Implementation
1.2: Virtual Series
1.1: Real Series
Coupled Load Independent Inverter [1], [5]
• Load and Position Independent Output **AC** voltage
AC Switch Network [4]
• Parasitics and Criticalities Mitigation
• Proof of Concept Prototype
• Measured and Simulated Results
Optimized Class E Rectifier [1], [5]
• Load and Position Independent Output **DC** voltage
Measured and Simulated Results [1], [5]
Passive Position Sensing via Inverter Currents
High Throughput Data Transfer Link
Conclusions

This page was intentionally left blank.

Chapter 1

Introduction to Wireless Power Transfer

"It is easier to resist at the beginning than at the end."

- Leonardo da Vinci -

"The transmission of power without wires will very soon create an industrial revolution and such as the world has never seen before," Tesla wrote in a 1906 letter to George Westinghouse [8].

He was a great visionary, but a bit ahead of his time. The technologies and especially the mentalities were not ready for such a revolution. He demonstrated his ability to send power wirelessly over short distances in his laboratory in Colorado Springs [8], but he failed in his main goal to scale up the effort and transmit power everywhere without cables.

For about a hundred years, and by the time his power tower in Wardecliffe in fig. 1.1 came crashing down, people forgot about the technology. Recently, though, some researcher and engineers started investigating and thinking how to dust off his vision and Wireless Power Transfer (WPT) or also Contact-less Energy Transfer (CET) systems have become more widely developed and investigated. They open to new possibilities of supplying mobile devices with electrical energy by eliminating cables, connectors, contacts, while increasing reliability and mobility and reducing maintenance

Figure 1.1: Nikola Tesla planned to use this immense tower to send power through the air.

of such systems in critical applications such as aerospace, biomedicine and robotics. They offer, for example, a major advantage in clean rooms applications, where the contacts would bring additional dust and require additional care.

A large number of technologies are available for the Contact-less Energy Transfer, and these are described with few common synonyms:

- Contact-less Energy Transfer (CET),
- Contact-less power transfer (CPT),
- Wireless Energy Transfer (WET),
- Wireless Power Transfer (WPT).

Semantically they are equivalent and in this thesis they refer to any means capable to transfer energy without cables, but some researchers like to express two different scenarios: with Contact-less they refer to near-to-contact systems, therefore where the distance is short and much smaller than the system used to transfer that energy, while with Wireless they refer to longer distances.

Various techniques are divided according to the distance and the medium used for energy transfer, see fig. 1.2:

- Acoustics-based WPT [9], [10];
- Electromagnetically-based (EM) Far Field WPT [11]–[18]:
    - Light-based WPT [10];
    - Far Field RF [18];
- Mid-Field EM [19];
- Near-Field [10], [15], [16]:
    - Capacitive-based WPT;
    - Inductive Power Transfer (IPT).

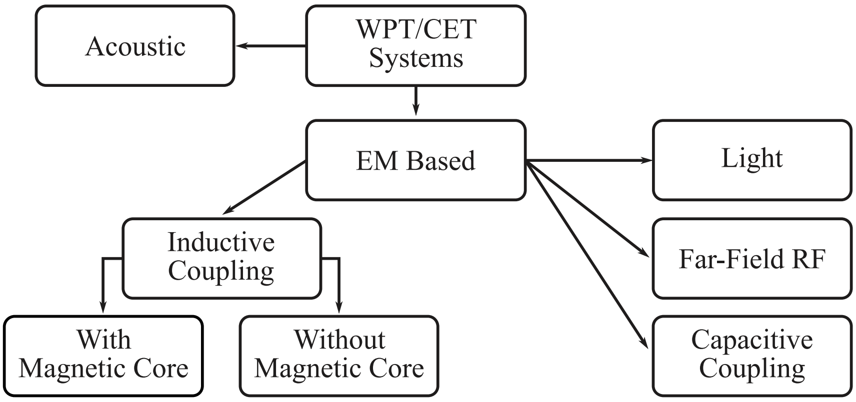

Figure 1.2: The classification of WPT systems [10]

1.1 Introduction to Inductive Power Transfer

This work focuses on the principle of Inductive Power Transfer, which is a Near Field WPT technique.

In 2007, Marin Soljačić and his colleagues at MIT, published an article in Science [20] describing hardware capable to transfer 60 W to an incandescent lamp using power transferred between two coils separated by more than 2 meters. The distance was over 8 times the radius of the coil, using self-resonant inductive coils and obtaining around 40% of efficiency. This was not the first attempt of IPT, but obtained lot of press coverage due to the large distance and made the Wireless Power Transfer (WPT) topic widespread.

Quite differently from popular belief, Wireless Power Transfer is today a mature technology and has its roots even before Tesla [21]–[23]. From the time of Ampere and Faraday and the founding of electric engineering based on their laws, the idea of wireless transmission of power has always been a goal.

At high frequencies, the works of Hertz where energy from a spark was coupled from one loop to another resulted in the modern radio systems, propagating power over large distances but with extremely low efficiencies. Indeed, while propagating, the wave increases its surface, distributing the power over it.

On the other hand, Faraday's work led to direct current (dc) and alternating current (ac) machines which were greatly enhanced by the invention of the induction machine by Nikola Tesla. Those machines converts electrical energy in mechanical one, by rotating a rotor using energy supplied from a stator through inductive coupling. Here, the efficiency is high, but the coupling distance is small and very constrained.

Experiments to couple power to moving trains were not successful, but low-power signals could be transferred, and so the myth was propagated that wireless power transfer over large distances with a coupling that was tolerant of misalignment and air-gap size, and was unaffected by dirt, water, ice, or chemicals was not practically possible. Signals-yes, power-no, and this categorization persisted for more than 100 years.

One of the first attempts to transfer power and energize an Electric

Figure 1.3: Opportunity charge bus in Genoa: in 2002 eight full electric buses were equipped with a 60 kW IPT® Charge.

Vehicle (EV) inductively, was done in 1894 by Hutin and Le-Blanc, powered by an approximately 3-kHz ac generator (U.S. Patent 527857). More recently, in 1972, Otto proposed an inductively powered vehicle using a 10 kHz and 10 kW force commutated SCR inverter [22]. His work proposed two copper conductors buried in the road and distant 20 cm, each carrying a current of 2000 A in opposing directions. Yes, 2000 A. Unsurprisingly, no parts of those experiments now remain.

Academic interest in IPT-powered EVs picked up in the late 1970s when, for example, Bolger, Ross, and others began publishing papers on electric highway systems [24]–[28].

In 1986, Kelly and Owens proposed powering aircraft entertainment systems using wires under the carpet in the passenger bay of an aircraft with essentially no controller [29].

Then, considerable effort has been done by people at the University of Auckland, in New Zealand, by John Boys, Andrew Green and Grant Covic.

In 1991, Boys and Green designed an IPT system potentially suitable for materials handling and other applications (U.S. Patent 5293308), which is the result of the work in IPT systems over the previous 20 years and represents a systematic approach to systematically design an IPT system. They licensed the patent to Daifuku Co. Ltd. in Japan, a company who makes pickup systems for clean rooms, and to Conductix-Wampfler GmbH, with the Inductive Power Transfer part now separated in IPT Technology GmbH, a company that designs opportunity Inductive Power Charging for Electric Vehicles. An important and innovative part of this work was the *decoupling controller* [30], which consisted of a boost converter after the rectifier. When there was no load, the switch of the converter was maintained shorted and was de-facto detuning the receiver, without showing any reactive load to the transmitter. From that on, they continued developing the system and achieved impressive results [22], [23]. Their technology is behind the buses in fig. 1.3, which is one of the first opportunity charge platforms and is running since 2002 in Genova, Italy.

1.1.1 Basics of Inductive Power Transfer

In a diagram of one of Tesla's wireless power experiments, the energy was transferred inductively using resonant coils [31]–[41], as in fig. 1.4.

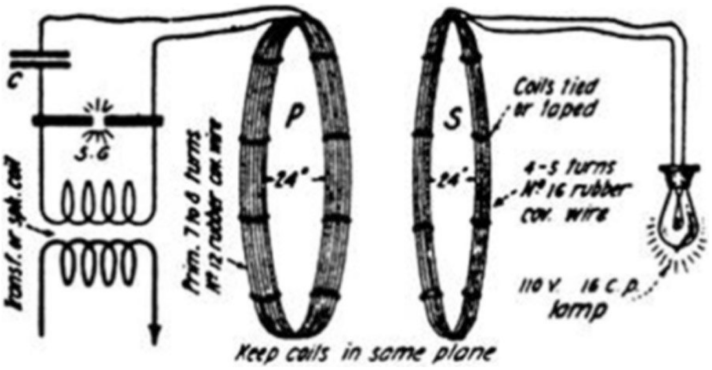

Figure 1.4: Diagram of one of Tesla's wireless power experiments [36].

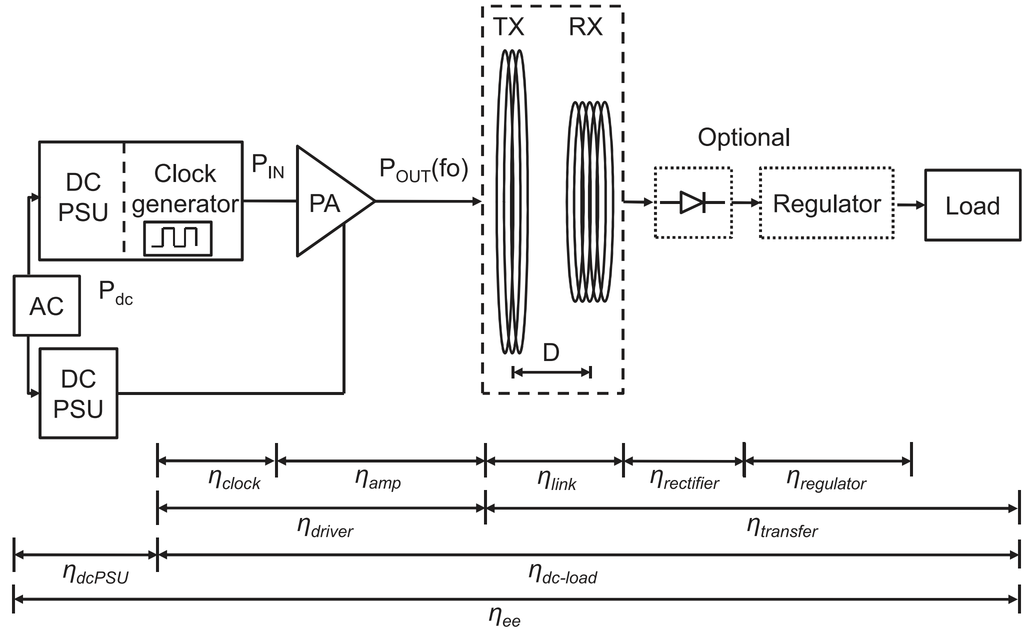

Figure 1.5: Example of a complete IPT link, from the AC main to the dc load [35]. Each partial efficiency is shown in an exploded fashion.

The equivalent of Tesla's diagram and of today's IPT systems is in fig. 1.5, which shows the basic block diagram of inductively coupled WPT systems. It consists of the mains rectifier, of a primary-side dc/ac resonant converter, which converts dc into high-frequency ac energy, of a transformer with the inductive coupling coefficient k, of a ac-dc resonant rectifier, an optional regulator and eventually the load. The secondary side is not connected electrically with the primary side and thus can be movable (linearly and/or rotating), giving flexibility, mobility, and safety to supplied loads.

Depending on the power range and air gap length, different transformer cores can be used. For high power and low air gap, transformers with magnetic cores in the primary and secondary are often applied, maximizing the shared flux between the coils and therefore the coupling coefficient. Contrary to this, for a large air gap and low/medium power, air transformers (core-less) are preferred. The air transformer offer higher mobility, less weight and cost, but also less inductance and coupling. This is the situation of this work, also named as loosely coupled coils. To overcome this issue, higher frequencies are needed, as will be clear in the following.

1.1.1.1 Coupled Coils and Coupling Coefficient

The inductive link is provided, in its simplest form, by two coils. Despite its apparent simplicity, there are lot of details to be considered for the proper design.

Since the focus of this work is on loosely coupled coils, what happens when the iron core of a transformer is removed? Indeed, two coupled coils are de-facto a transformer, and the usual equivalent circuit can be useful to grasp the effects, as in fig. 1.6. In a regular transformer, the iron core allows almost the entire flux generated by the current in one coil to flow to the other, with a very small portion which is lost.

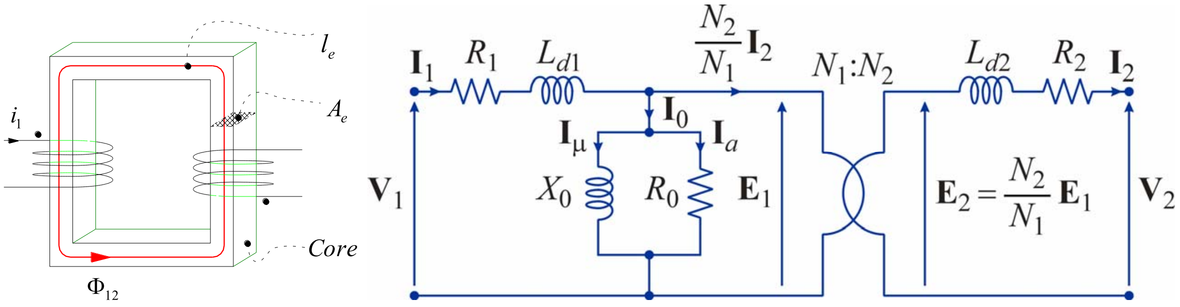

Figure 1.6: Simplified diagram of a transformer.

The coupling coefficient models the percentage of flux which is coupled:

$$k = \frac{\phi_{12}}{\phi_1} = \frac{\phi_{21}}{\phi_2} \tag{1.1}$$

where ϕ_1 and ϕ_2 are the total flux in the respective coil, while ϕ_{12} and ϕ_{21} the shared flux. Note that ϕ_{12} is usually different from ϕ_{21}, but the percentage on the respective total is not, as the coupling depends only on the geometries of the link and on the coils. For example, if the secondary is open, there is no current and hence $\phi_2 = 0$, which means $\phi_{21} = 0$, but does not mean $\phi_{12} = 0$.

By taking the constitutive relations:

$$\begin{aligned} L_1 &= \frac{N_1\phi_1}{i_1} \quad L_2 = \frac{N_2\phi_2}{i_2} \\ M &= \frac{N_2\phi_{12}}{i_1} \quad M = \frac{N_1\phi_{21}}{i_2} \end{aligned} \tag{1.2}$$

then

$$MM = \frac{N_1\phi_{21}N_2\phi_{12}}{i_1 i_2}. \tag{1.3}$$

If $k = \phi_{12}/\phi_1$ and $k = \phi_{21}/\phi_2$, then:

$$M^2 = \frac{N_1 k\phi_2 N_2 k\phi_1}{i_1 i_2} \tag{1.4}$$

or

$$M^2 = k^2 \frac{N_1\phi_1}{i_1}\frac{N_2\phi_2}{i_2} = k^2 L_1 L_2 \tag{1.5}$$

and therefore the coupling coefficient is written as:

$$k = \frac{M}{\sqrt{L_1 L_2}} = \frac{\phi_{12}}{\phi_1} = \frac{\phi_{21}}{\phi_2}. \tag{1.6}$$

For more coils, each coupling between coil L_a and L_b is then:

$$k_{ab} = \frac{M_{ab}}{\sqrt{L_a L_b}}. \tag{1.7}$$

When the iron is removed, for example due to mobility reasons, the leakage inductances ($L_{d1} = (1-k)L_1$ and $L_{d2} = (1-k)L_2$ in fig. 1.6) become large and, because ωL_{d2} is much larger than the useful load at weak couplings, it requires higher $\boldsymbol{E}_1$. The magnetizing inductance $X_0/(j\omega) = kL_1$, which is proportional to k and represents the flux which is linked to the secondary, falls dramatically, reducing the primary induced voltage $\boldsymbol{E}_1$ and affecting sensibly the efficiency of the link (η_{link} in fig. 1.5). Furthermore, ωL_{d1} is also large, which further reduces $\boldsymbol{E}_1$. Both effects are related and indeed they are caused by the same cause, but they cause a stronger than linear reduction of the primary induced voltage. The efficiency is too low, or impractical, for low couplings ([34] indicates k below 5%) without any countermeasure.

At this point, before discussing if a poor coupling means a poor efficiency, we must discuss how to define the efficiency of the link. If P_{out} is the power before the rectifier and P_{in} the power entering the primary coil:

$$\eta_{\text{link}} = \frac{P_{out}}{P_{in}} \tag{1.8}$$

Lot of authors, most of them with a RF background, define the link efficiency as:

$$\eta_{\text{link}} = |S_{21}|^2 \tag{1.9}$$

where S_{21} is defined from the transmission coefficient of the scattering parameters. Eq. (1.9) supposes:

- A reflection-less matching of the load to the secondary, which is a different condition than the load for maximum efficiency;
- The normalizing impedances (usually $50\,\Omega$) for computing the scattering parameters to be the same of the load;
- The equivalent impedance of the generator to be equal to the normalizing impedance or that the available power of the generator is lost when not delivered to the load.

While the normalization is arbitrary, the impedances are usually different:

- The load is chosen to maximize the efficiency of the link, which means that the power transferred to the receiver is the maximum share of the input one;
- Since the inverter can not be represented using the Thévenin equivalent, due to its strongly non linear behaviour, the usual conjugate matching to the internal impedance is not applicable;

- With reference to a resonant inverter, there is an optimum load where its efficiency is maximized (it is not the open load as would be for the Thévenin equivalent);
- The available power has not a particular meaning with resonant inverters and usually the optimum load provides both the maximum output power and efficiency of the inverter;
- In the other cases there would be two optimal loads, one for the maximum physical output power (loadline matching [42]) of the inverter and one for its maximum efficiency;
- Using the optimal load of the inverter and the condition for maximum efficiency of the link, it means that power is transferred from the inverter to the receiver in the optimum way, which usually coincides with both the maximum efficiency and maximum power transfer.

To avoid any misunderstanding, in this work, the definition of link efficiency uses the formal and rigorous one, as defined in eq. (1.8).

Equivalently, the total efficiency, from dc-to-dc, is defined as:

$$\eta = \frac{P_{DC_{out}}}{P_{DC_{in}}}. \tag{1.10}$$

Note that the definition of total efficiency used in this work does not consider the mains rectifier, from 50 Hz ac mains to dc in, which is intentional and not interesting here because outside the scope of this thesis.

After having defined the efficiency, does a poor coupling mean a poor efficiency? First, if the iron is removed, the iron losses are zero (or $R_0 = \infty$), which removes a source of losses. Second, the link can be analyzed using circuit theory for coupled circuits [23], [34], [41].

Figure 1.7(a) depicts the circuit model of IPT systems where the transmitting coil L_1 and the receiving coil L_2 are directly connected to the power source and the load impedance Z_L, respectively. An equivalent representation is also the T-model, as shown in fig. 1.7(b). Denote M_{12} as the mutual inductance, R_1 and R_2 as the equivalent ac resistance of coils. According

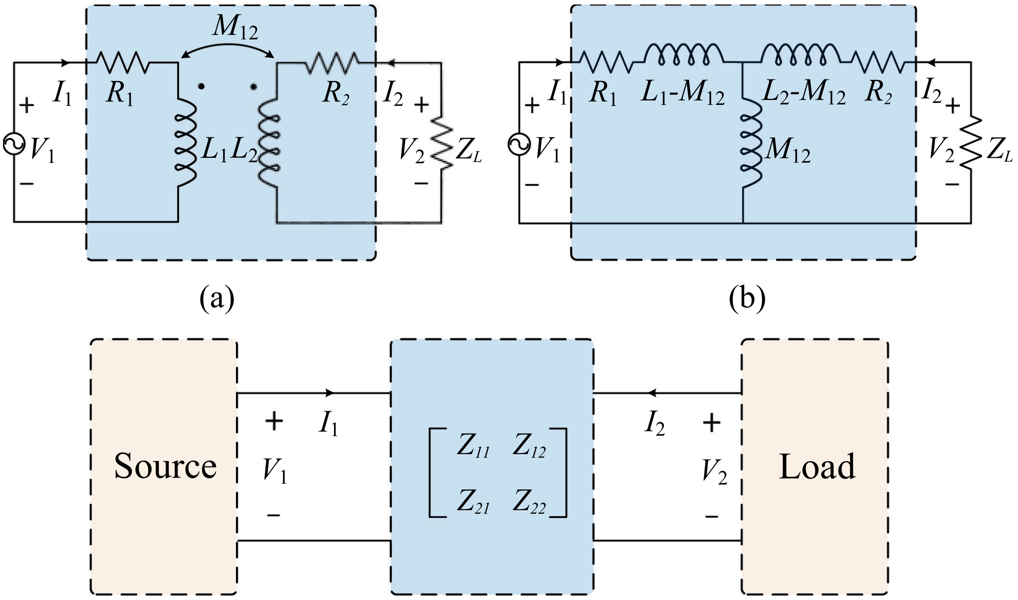

(a) (b)

(c)

Figure 1.7: IPT. (a) Circuit model. (b) Equivalent T-model. (c) Two-port network model.

to the two-port network model as shown in fig. 1.7(c), the voltage equation can be obtained as:

$$\begin{aligned}\begin{bmatrix} V_1 \\ V_2 \end{bmatrix} &= \begin{bmatrix} Z_{11} & Z_{12} \\ Z_{21} & Z_{22} \end{bmatrix} \begin{bmatrix} I_1 \\ I_2 \end{bmatrix} \\ &= \begin{bmatrix} R_1 + j\omega L_1 & j\omega M_{12} \\ j\omega M_{12} & R_2 + j\omega L_2 \end{bmatrix} \begin{bmatrix} I_1 \\ I_2 \end{bmatrix}\end{aligned} \tag{1.11}$$

and the corresponding input and output impedances, when $V_2 = Z_L I_2$ and $V_1 = Z_S I_1$ respectively, are:

$$\begin{aligned} Z_{in} &= Z_{11} - \frac{Z_{12}^2}{Z_{22} + Z_L} \\ Z_{out} &= Z_{22} - \frac{Z_{12}^2}{Z_{11} + Z_S} \end{aligned} \tag{1.12}$$

From that representation, the link efficiency in eq. (1.8) can be written as:

$$\eta_{\text{link}} = \left| \frac{Z_{12}}{Z_L + Z_{22}} \right|^2 \frac{\text{Re}\{Z_L\}}{R_1 + \frac{\omega^2 M_{12}^2 (R_2+R_L)}{(R_2+R_L)^2+(X_2+X_L)^2}} \tag{1.13}$$

where $Z_L = R_L + X_L$, R_2 is the series resistance of the receive coil and $X_2 = \omega L_2$. Eq. (1.13) represents the efficiency of the two port in fig. 1.7(c).

By computing the maximum of the efficiency in eq. (1.13), the optimal load results in [41], [43]:

$$Z_{L,\text{opt}} = R_2 \sqrt{1 + k_{12}^2 Q_1 Q_2} - j\omega L_2 \tag{1.14}$$

where $k_{12} = k$ (since this example has only two coils) is the same as in eq. (1.7) and the quality factor of the coils are defined as:

$$Q_a = \frac{\omega L_a}{R_a}. \tag{1.15}$$

The maximum efficiency is therefore:

$$\eta_{\,\text{link}_{\text{max}}} = \frac{k^2 Q_1 Q_2}{\left(1 + \sqrt{1 + k^2 Q_1 Q_2}\right)^2} \tag{1.16}$$

Equation (1.16) tells us that, with loosely coupled coils, a good efficiency is possible if the quality factors of the coils are high enough to compensate the low coupling coefficient k. Hence, to answer the initial question, a poor coupling does not mean a poor efficiency and therefore a suitable Figure of Merit (FoM) must be identified. Equation (1.16) also suggests which quantity would be a suitable FoM, which is the product $k^2 Q_1 Q_2$. Indeed, the efficiency is a monotonic increasing function of $k^2 Q_1 Q_2$.

A similar FoM is suggested by [44], where he proposes the kQ product. Basically, it is simply the square root of $k^2 Q_1 Q_2$ and therefore it can be seen as an equivalent FoM:

$$k^2 Q_1 Q_2 = k^2 \frac{\omega L_1}{R_1} \frac{\omega L_2}{R_2} = \left(\frac{\omega M_{12}}{\sqrt{R_1 R_2}} \right)^2 = (kQ)^2 \tag{1.17}$$

In other words, kQ is the equivalent quality factor of the mutual inductance M_{12}:

$$kQ = \frac{|Z_{12}|}{\mathrm{ESR}} = \frac{\omega M_{12}}{\sqrt{R_1 R_2}} \tag{1.18}$$

where $\mathrm{ESR} = \sqrt{R_1 R_2}$ is the Equivalent Scalar Resistance.

Now the following question is how to maximize the kQ product (or $k^2 Q_1 Q_2$) and the answer is more tricky. Indeed the structure of the near field is extremely complex [45], [46] and a theoretical optimal solution is too complex for a generic configurations of currents. What can be done is a qualitative procedure using some simplified reasonings [35]:

- k depends only on the geometries (distance included):
  - There is an optimum size and shape which maximizes k for a certain distance;
  - Specially shaped coils, i.e. conformal to the magnetic field, can provide the highest coupling;
- The quality factor $Q_a = \frac{\omega L_a}{R_a}$:
  - Generally, the approach is to maximize the coil area in the available space (hence $\mathrm{L_a}$ is maximized), but minimizing the conductor length (hence keeping $\mathrm{R_a}$ low);
  - Maximize the number of turns ($\mathrm{N_a}$), since the inductance has a square relation with the number of turns ($\mathrm{L_a} \propto \mathrm{N_a}^2$) and the conductor length is increasing proportionally to them ($\mathrm{R_a} \propto \mathrm{N_a}$) while the coupling is ideally not affected ($k(\mathrm{N_a}) \sim$ const);
  - Choose an optimal frequency:
    - Q is maximized when radiation begins to dominate losses for a certain size, but then the coil impedance is affected by parasitics;
    - It is usually advised to use the highest frequency with a linear reactance;
    - The number of turns affects the parasitics and therefore the maximum usable frequency;

    - ∗ This pushes the frequency higher, therefore requiring the development of MHz power electronics;

- The relation between the coupling factor k and the quality factor Q is complex and they are not mutually independent;

- For example a bigger coil at a fixed distance can have lower k but still provide an increased kQ;

- The inclusion of parasitics makes everything more complicated and less predictable;

- To obtain a good design of the coil, an full-wave optimization of the link geometry, using a goal that maximizes kQ should be performed;

- The full-wave optimization is required, because it must take into consideration also the parasitics, which are not computed by a magnetostatic simulation: the frequency domain simulation (FEA/FEM) is the best option because an IPT link usually employs a single frequency.

1.1.2 Compensation Network

Before introducing the compensation networks, let us consider again eq. (1.13). When the load is purely resistive and $X_L = 0$, which we call the uncompensated case, the maximum link efficiency can be rewritten as [34]:

$$\eta_{link_{max},\, UC} = \frac{k^2 Q_1 Q_2}{2 + k^2 Q_1 Q_2 + 2\sqrt{1 + Q_2^2 + k^2 Q_1 Q_2}} \tag{1.19}$$

If we rearrange eq. (1.16) a comparable equation comes out:

$$\eta_{link_{max}} = \frac{k^2 Q_1 Q_2}{2 + k^2 Q_1 Q_2 + 2\sqrt{1 + k^2 Q_1 Q_2}}. \tag{1.20}$$

Equation (1.20) differs from eq. (1.19) only for the additional Q_2^2 term. The only difference between the two cases, is that eq. (1.20) implements the optimal load impedance instead of only the optimal load resistance. This is

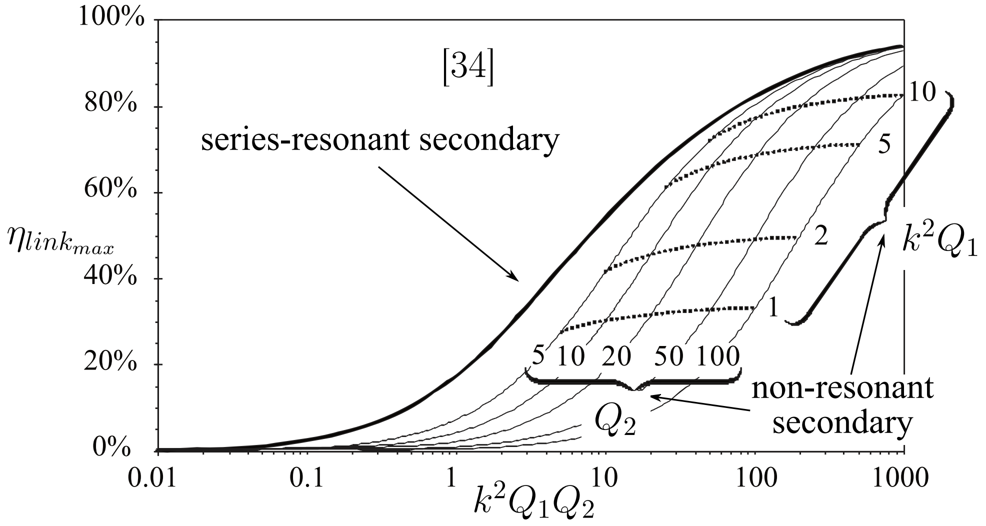

Figure 1.8: The maximum link efficiency for compensated and uncompensated secondary as a function of $k^2Q_1Q_2$ and the coil quality factors.

called the compensated, or resonant, case and is needed to harness the full capabilities of the link and reward the efforts to optimize kQ.

Figure 1.8 helps to visualize and understand the differences, showing how a resonant secondary improves the link efficiency, especially for low couplings. This diagram, if not properly read, can erroneously suggests that a lower secondary coil quality factor corresponds to a higher link efficiency in case of a non-resonant secondary. Indeed, because $k^2Q_1Q_2$ is taken as horizontal co-ordinate, a lower secondary coil quality factor for the same $k^2Q_1Q_2$ automatically implies a higher primary coil quality factor and the corresponding reduction in the primary dissipation overcompensates the increased secondary loss. In other words, for the uncompensated case, the quality factor of the primary is more important than the one of the secondary.

Efficient uncompensated links can be realized only with high couplings, which implies iron cores, while for low couplings the advantage of the compensated solution is evident. Indeed, the latter can use both coils to push its efficiency, compared to the former which needs a unrealistically high secondary quality factor. For example, if $Q_1 = 100$, $Q_2 = 100$ and $k = 0.1$, which are reasonable for industrial CET moving applications, the uncompensated case would provide about 30% of efficiency, while the compensated case is over 80%.

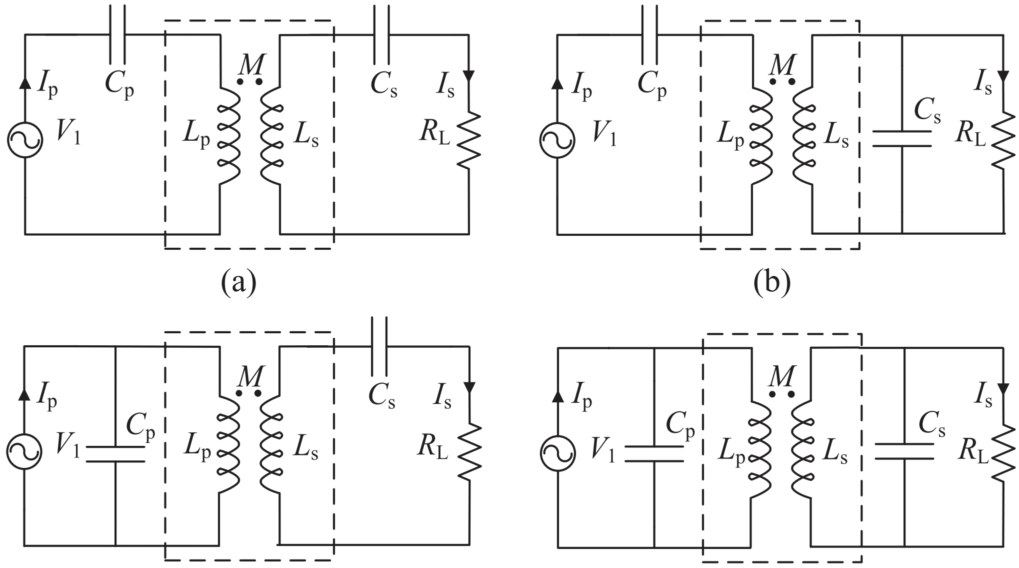

(a) (b)

(c) (d)

Figure 1.9: Compensation networks: (a), Series Series (SS), (b), Series Parallel (SP), (c), Parallel Series (PS) and (d), Parallel Parallel.

Figure 1.9 shows the 4 possible compensations: (a), Series Series (SS), (b), Series Parallel (SP), (c), Parallel Series (PS) and (d), Parallel Parallel. According to eqs. (1.13), (1.14) and (1.16), only the secondary circuit needs a capacitive compensation to eliminate the imaginary part and maximize the efficiency, since using the optimum load provides the maximum efficiency. A compensation of the primary is required to reduce the Volt Ampere Reactive (VAR) load of the inverter. In a usual link, both compensation are required, but the resonant primary could even be part and included in the inverter.

By using the reflected impedance theory, the compensated capacitances can be calculated with respect to various network topologies [31], [32], [34],

[41].

In [31], [32], the capacitances are computed in a lossless case and are listed in table 1.1. The working frequency is selected as the natural resonance of the secondary resonator, $\omega = 1/\sqrt{L_2C_2}$, while the primary ones are obtained depending on the connection. The reflected load depends also on the connection, with the series secondary behaving as an immittance inverter.

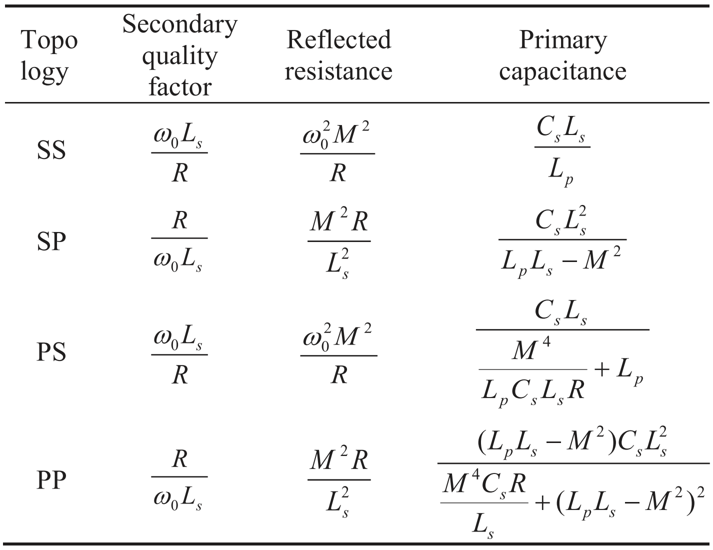

Topo logy	Secondary quality factor	Reflected resistance	Primary capacitance
SS	$\frac{\omega_0 L_s}{R}$	$\frac{\omega_0^2 M^2}{R}$	$\frac{C_s L_s}{L_p}$
SP	$\frac{R}{\omega_0 L_s}$	$\frac{M^2 R}{L_s^2}$	$\frac{C_s L_s^2}{L_p L_s - M^2}$
PS	$\frac{\omega_0 L_s}{R}$	$\frac{\omega_0^2 M^2}{R}$	$\frac{C_s L_s}{\frac{M^4}{L_p C_s L_s R} + L_p}$
PP	$\frac{R}{\omega_0 L_s}$	$\frac{M^2 R}{L_s^2}$	$\frac{(L_p L_s - M^2) C_s L_s^2}{\frac{M^4 C_s R}{L_s} + (L_p L_s - M^2)^2}$

Table 1.1: Effects of the Compensation ($M_{12} = M$ and $R_{12} = R$ to simplify the table). The working frequency is $\omega = 1/\sqrt{L_sC_s}$

In series-compensation, the impedance of the secondary inductance and its compensated capacitance cancel each other out at the resonant frequency, making the output voltage independent of the load and equal to the secondary open circuit voltage. As a result, there is theoretically no limit to the power transfer capability, in the loss-less case, because the series-compensated secondary is in effect a voltage source driving into the output load. It usually provides low output voltages and requires loads with low impedance. It provides a sinusoidal current output, with $i_2 = |i_2|cos(\omega t)$, an no dc path.

In parallel-compensation the admittance of the secondary inductance and its compensated capacitance cancel each other out at the resonant frequency. This makes the output current independent of the load and equal to the secondary short circuit current. Consequently, in theory there is also no limit to the power transfer capability, in the loss-less case, since the parallel-compensated secondary is an effective current source driving into the load. It usually provides high output voltages and requires loads with high impedance. It provides a sinusoidal voltage output, with $v_2 = |v_2| cos(\omega t)$ and the dc path.

On the primary side, a series compensation reduces the Volt Ampere (VA) requirements of the inverter, but requires an high current output and hence its optimum load should have low resistance. It is ideal for inverters with current output. A parallel compensation also reduces the Volt Ampere (VA) requirements of the inverter, but requires an high voltage output. It is ideal for inverters with a voltage output and high impedance. It can be used for applications that requires high currents, without requiring the same current to flow through the inverter, because these are just circulating in the coil and capacitor. The advantage is that creates high magnetic fields and therefore is useful with very low couplings. Anyway, high magnetic fields can also be a source of issues, due to health and safety regulations.

Series-parallel-compensation [47] is a trade-off between the reduction of voltage and current ratings. This is sometimes necessary to ensure that both the voltage and current ratings are designed to meet industrial regulation but using commercially available components that are cost effective.

It should be noted that the Series Series is the only topology which is independent of the coupling coefficient and of the load condition, since the reflected reactance equals zero on the primary side. This result is important when working with resonant inverters, where the operational regime of the inverter is strongly influenced by any minimal variation of the input reactance.

The method above uses the natural resonance frequency (ω) of the secondary resonator, but other options are also viable, which anyway are quite similar. In [34], they calculate the resonant frequency similarly to [31], therefore compensating the reflected reactance to be zero, but they include also losses in the coils. This results in an optimal load, which for the series connection is:

$$R_{L,\mathrm{optS}} = R_2\sqrt{1+k^2Q_1Q_2}, \text{ with } \omega_S = \omega = \frac{1}{\sqrt{L_2C_2}} \tag{1.21}$$

while for the parallel case is:

$$R_{L,\mathrm{optP}} = \frac{L_2}{C_2}\frac{1}{R_2\sqrt{1+k^2Q_1Q_2}}, \text{ with } \omega_P = \sqrt{\omega^2 - \frac{1}{R_L^2C_2^2}} \tag{1.22}$$

Note that the parallel case, in order to reflect a zero reactance, has the resonance frequency dependent on the load, which is also called the resonance frequency of the loaded secondary.

A different approach is followed by [41], which calculates directly the optimal resonant frequency that results in the maximum efficiency for each compensation topology, without forcing the reflected reactance to be zero. However, for high quality factors and loosely coupled coils, which is usual without iron cores, the optimal frequency is approximately the natural one (ω).

1.1.3 Class E ZVS Inverter

The Class E Zero Voltage Switching (ZVS) inverter [48]–[51] belongs to the family of soft-switching inverters, and are the most efficient inverter known so far. The current and voltage waveform of the switch are carefully designed to enable the high efficiency operation by turning on the switch at zero voltage. Since the switch current and voltage waveforms do not overlap during the switching time intervals, switching losses are virtually zero, yielding high efficiency. This condition is fundamental when working with high frequencies, because most of the losses are due to switching losses.

In this section, a simple qualitative description of its operation is discussed to provide, albeit simple, insights into the characteristics of this inverter as a basic power cell.

The ideal schematic of a Class E inverter is given in fig. 1.10. It consists of a power device (an HEMT, or MOSFET, or other suitable ones) operating as a switch, a $L_LC_LR_L$ series-resonant circuit, a shunt capacitor C_1, and a

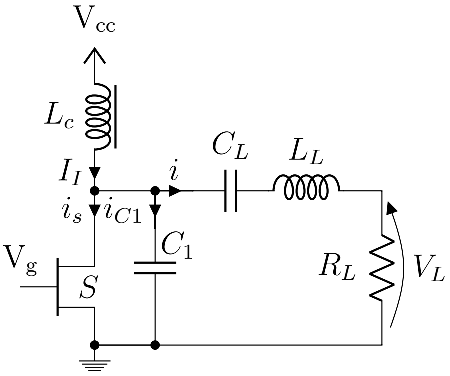

Figure 1.10: Class E ZVS inverter.

choke inductor L_C. The switch turns on and off at the operating frequency $f = \omega/(2\pi)$ determined by a driver, which has an easy job because it is referenced only to the ground node. Indeed, the bootstrap diode or the floating dc source is not needed, compared to the Class D. The transistor output capacitance, the choke parasitic capacitance, and stray capacitances are included in the shunt capacitance C_1. For high operating frequencies, all of capacitance C_1 can be supplied by the overall shunt parasitic capacitance. The resistor R_L, is an AC load. The choke inductance L_C is assumed to be high enough so that the AC ripple on the DC supply current can be neglected.

When the switch is ON, the resonant circuit consists of L_L, C_L and R_L, because the capacitance C_1 is short-circuited by the switch. However, when the switch is OFF, the resonant circuit consists of L_L, C_1, C_L and R_L connected in series. Because C_1 and C_L are connected in series, the equivalent capacitance $C_{eq} = C_L C_1/(C_L + C_1)$ is lower than C_L and C_1. The load network is therefore characterized by two resonant frequencies and two loaded quality factors. When the switch is ON,

$$f_{o1} = \frac{1}{2\pi\sqrt{L_L C_L}}, \; Q_{L1} = \frac{\omega_{o1} L_L}{R_L} = \frac{1}{\omega_{o1} C_L R_L}. \tag{1.23}$$

When the switch is OFF,

$$f_{o2} = \frac{1}{2\pi\sqrt{\frac{L_L C_L C_1}{C_L + C_1}}}, \; Q_{L2} = \frac{\omega_{o2} L_L}{R_L} = \frac{1}{\frac{\omega_{o2} L_L C_L C_1}{C_L + C_1}}. \tag{1.24}$$

fig. 1.11 shows current and voltage waveforms in the Class E ZVS inverter for three cases: $dv_s(\omega t)/d(\omega t) = 0$, $dv_s(\omega t)/d(\omega t) < 0$, $dv_s(\omega t)/d(\omega t) > 0$ at $\omega t = 2\pi$ when the switch turns on. In all three cases, the voltage vs across the switch and the shunt capacitance C_1 is zero when the switch turns on. Therefore, the energy stored in the shunt capacitance C_1 is zero when the switch turns on, yielding zero turn-on switching loss. Thus, the ZVS condition is expressed by:

$$v_s(2\pi) = 0 \tag{1.25}$$

The choke inductor L_C forces a dc current I_I. To achieve zero-voltage switching turn-on of the switch, the operating frequency $f = \omega/(2\pi)$ should be greater than the resonant frequency $f_{o1} = 1/(2\pi\sqrt{L_L C_L})$, hence $f > f_{o1}$. However, the operating frequency f is usually lower than $f_{o2} = 1/(2\pi\sqrt{L_L C_{eq}})$, hence $f < f_{o2}$. The shape of the waveform of the current i depends on the loaded quality factor Q_L, and if it is high i is approximately sinusoidal. The combination of the choke inductor and the load series-resonant circuit acts as a current source whose current is $I_I - i$. When the switch is ON, the current $I_I - i$ flows through the switch. When the switch is OFF, the current $I_I - i$ flows through capacitor C_1, producing the voltage across shunt capacitor C_1 and the switch and hence shaping its voltage.

fig. 1.11(a) shows current and voltage waveforms for optimum operation. In this case, both the switch voltage v_s and its derivative dv_s/dt are zero when the switch turns on. The second condition is given by:

$$\left.\frac{dv_s(\omega t)}{d(\omega t)}\right|_{\omega t = 2\pi} = 0 \tag{1.26}$$

The first condition is called zero-voltage switching (ZVS), and the second one is called zero-derivative switching (ZDS) or zero-slope switching. The two conditions are the "nominal conditions". The optimum conditions are

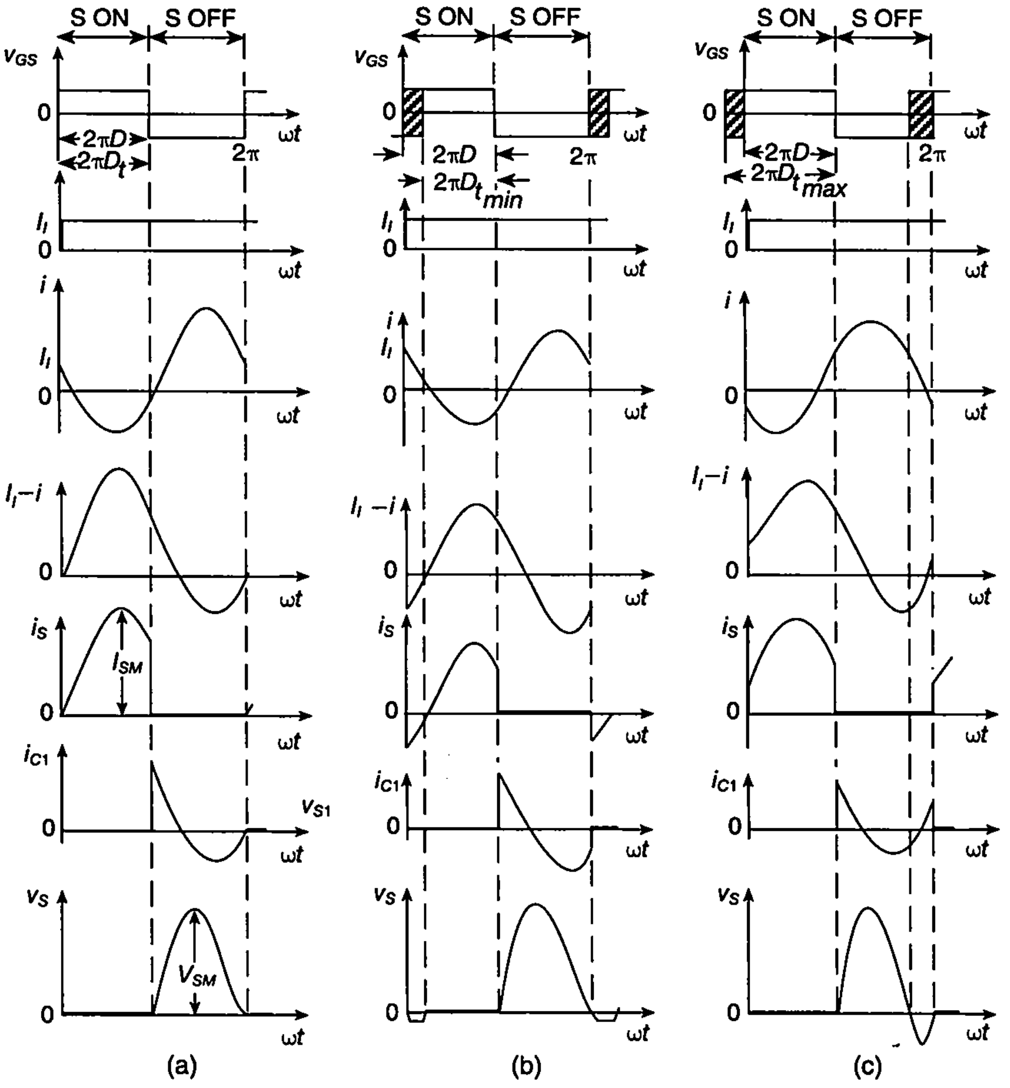

Figure 1.11: Waveforms in Class E zero-voltage-switching inverter [49]. (a) For optimum operation. (b) For suboptimum operation with $dv_s(\omega t)/d(\omega t) < 0$ at $\omega t = 2\pi$. (c) For suboptimum operation with $dv_s(\omega t)/d(\omega t) > 0$ at $\omega t = 2\pi$.

the operating conditions at which the maximum drain efficiency is achieved. For real components, the optimum conditions are off-nominal conditions. The smaller the parasitic components, the closer are the nominal and optimum operating conditions. Because the derivative of v_s is zero at the time the switch turns on, the switch current is increases gradually from zero after the switch is closed. It should be noted that both the switch voltage and the switch current are positive for optimum operation. Therefore, there is no need to add any diode to the switch. Close relationships among C_1, L_L, R_L, f and the duty-cycle D must be satisfied to achieve optimum operation [52]. Therefore, optimum operation can be achieved only at an optimum load resistance $R_L = R_{L_{opt}}$. If $R_L > R_{L_{opt}}$, the amplitude of the current i through the load series-resonant circuit is lower than that for optimum operation, the voltage drop across the shunt capacitor C_1 decreases, and the switch voltage v_s is greater than zero at turn-on. On the other hand, if $R_L < R_{L_{opt}}$, the amplitude of i is higher than that for optimum operation, the voltage drop across the shunt capacitor C_1 increases, and the switch voltage v_s is less than zero at turn-on. In both cases, the energy in the capacitor C_1 is dissipated in the transistor as heat after the switch is turned on, resulting in a turn-on switching loss. To obtain ZVS operation at a wider load range, an anti-parallel or a series diode can be added to the transistor. This improvement ensures that the switch automatically turns on at zero voltage for $R_L < R_{L_{opt}}$.

For operation with zero-derivative switching (ZDS), Miller's effect is reduced to zero, since instantaneous voltage gain is zero, and therefore the gate-to-drain capacitance reflected to the gate-to-source terminals is C_{gd} and the FET input capacitance is $C_i = C_{iss} = C_{gs} + C_{gd}$. Since Miller's effect is eliminated and the FET input capacitance is low, the gate-to-source voltage V_G increases much faster than in the inverters with hard switching, in which the slope of the transistor voltage is large when the transistor turns on.

The Class EF used in this work is an extension of the Class E, where a certain numbers of harmonics are shunted in its output, similarly to the Class F [53], [54]. In this way, the behaviour of the inverter is modified and other solutions with different characteristics are possible, as for example the load independent behaviour.

1.2 Introduction to Wide Band-Gap (WBG) Semiconductors

The power electronic market is expected to grow steadily in the very next years, driven by established applications, as rail traction or motor drives, or by novel applications, as Electric Vehicles or the Wireless Smart Powering of pervasive and IoT systems. The need of high efficiency and of weight, size, and cost reduction is driving the research for novel materials and devices which could sensibly change the electronics of the future.

Wide Band Gap (WBG) Semiconductor Market is currently governed by two materials, the Gallium Nitride (GaN) and the Silicon Carbide (SiC) [55]–[66]. The SiC technology is quite mature, especially for the Schottky diodes, and can withstand voltages from approximately 600 V to few thousands of Volts. The GaN technology is less mature, uses HEMT transistors instead of MOS ones, and withstands less voltages, from approx 100 V to 600 V. They present less capacitance and therefore are suitable for higher frequencies, as high as few MHz if soft-switching techniques are considered.

The ideal power switch should be able to block high voltages without any leakage current when in the off state, to have zero resistance in the on state, and to have an instantaneous switch on and switch off, without any charge storage.

1.2.1 Why Wide Band Gap Semiconductors?

To understand why a Wider Band Gap is favorable the *Baliga's Figure of Merit* is derived for the 1D Abrupt Junction. Starting from the Poisson's equation it is possible to express the electric field $E(x)$, or equivalently the potential $V(x)$, inside the junction (fig. 1.12) as follows:

$$E(x) = \frac{-qN_D}{\varepsilon}\left(W_D - x\right), \tag{1.27a}$$

$$V(x) = \frac{qN_D}{\varepsilon}\left(W_D x - \frac{x^2}{2}\right). \tag{1.27b}$$

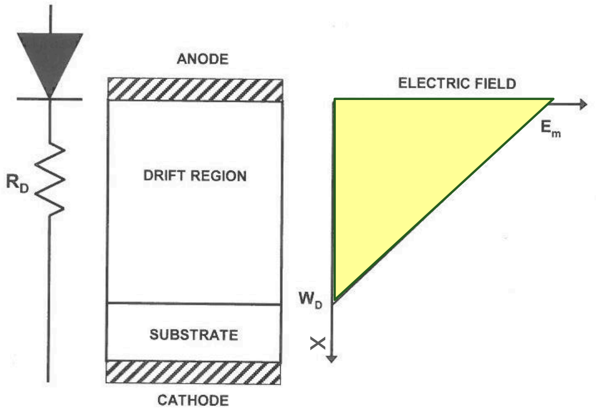

Figure 1.12: 1D Abrupt Junction.

If the device is subject to the breakdown voltage V_{bd}, eq. (1.27b) is rewritten as:

$$V_{bd} = \frac{qN_D W_D^2}{2\varepsilon}, \tag{1.28}$$

and hence

$$W_D = \sqrt{\frac{2\varepsilon V_{bd}}{qN_D}}. \tag{1.29}$$

The electric field at the interface $E(0)$ when the device is subject to the breakdown (critical field E_C) is then expressed as:

$$E(0) = -E_C = \frac{-qN_D W_D}{\varepsilon}, \tag{1.30}$$

which used in eq. (1.28) provides

$$V_{bd} = \frac{E_C W_D}{2}. \tag{1.31}$$

Now the carrier density can be expressed using eqs. (1.29) and (1.31) as

$$N_D = \frac{\varepsilon E_C^2}{2qV_{bd}}. \tag{1.32}$$

If the channel resistance is then expressed in terms of its resistivity:

$$R_{on} = \frac{W_D}{qN_D\mu_N}, \tag{1.33}$$

and therefore:

$$R_{on} = \frac{W_D^2}{\mu_n\varepsilon E_C} = \frac{4V_{bd}^2}{\mu_n\varepsilon E_C^3}. \tag{1.34}$$

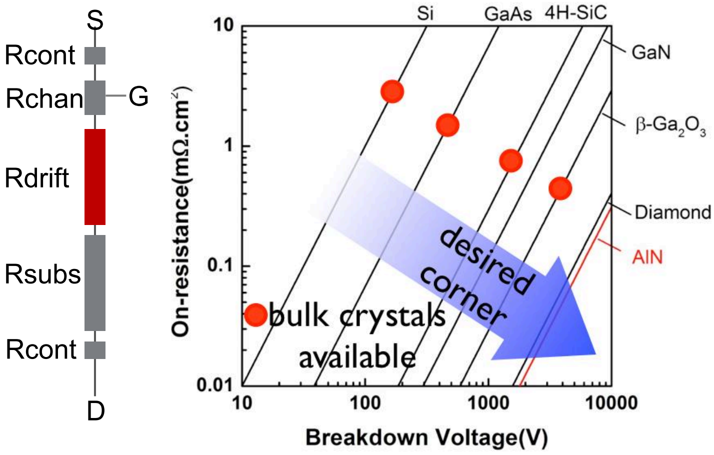

Figure 1.13: On-channel resistance for a 1-D Abrupt Junction.

The Baliga's FoM [66]–[68] is a metric to compare different materials for uni-polar power device technology. It considers the drift electron mobility μ, without taking into account the doping, and the critical electric field E_C. It represents a trade-off between the on resistance of the channel R_{on}) and the breakdown voltage V_{bd} (see fig. 1.13):

$$\text{BFOM} = \mu_n\varepsilon E_C^3 \tag{1.35}$$

and is directly related to the power-device-figure-of-merit V_{bd}^2/R_{on}:

$$\text{BFOM} \propto \frac{V_{bd}^2}{R_{on}} \tag{1.36}$$

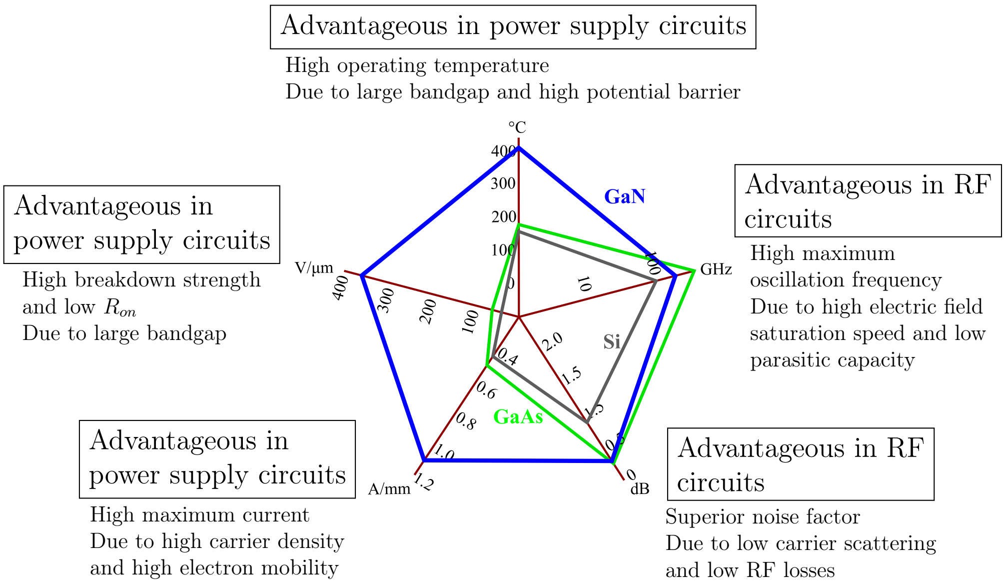

Advantageous in power supply circuits

High operating temperature
Due to large bandgap and high potential barrier

Advantageous in power supply circuits

High breakdown strength and low R_{on}
Due to large bandgap

Advantageous in RF circuits

High maximum oscillation frequency
Due to high electric field saturation speed and low parasitic capacity

Advantageous in power supply circuits

High maximum current
Due to high carrier density and high electron mobility

Advantageous in RF circuits

Superior noise factor
Due to low carrier scattering and low RF losses

Figure 1.14: Above, Baliga's FoM with additional parameters. Below, radar chart to compare the performances of WBG semiconductors to silicon, focused on the application.

A comparison for silicon, gallium nitride and gallium arsenide can be simplified to the radar chart in fig. 1.14, which is a simplification but gives the idea of the capabilities of WBG semiconductors for different applications.

1.3 Introducing the Next Chapters

In the next chapters a complete framework to design position independent links is discussed, which allows to obtain a moving link that behaves as being still.

In chapter 2, the framework is focused on industrial scenarios, where some movers need to freely move over a powered path. Different scenarios, for example with machineries for clean rooms or with machineries that require low periodic maintenance, necessitate of a wireless transfer on energy to the on-board electronics. Each position on the path should be invisible to the mover, which needs to be powered identically in each position. Sections 2.1 and 2.2 discuss the solutions to obtain a constant coupling coefficient using two transmitters and one geometrically optimized receiver. Section 2.3 provides a design solution which employs physical switches, or Solid State Relays, along with all the rules to cope with the effects of parasitics and asymmetric switches. This solution is suitable for low frequency applications, because the parasitics introduce stray resonances. Section 2.4 introduces the idea of Coupled Load Independent Class EF Inverter, which is able to drive efficiently two transmitting coils with the same current, therefore implementing a *virtual series*. The prototype transferred 100 W to the dc receiver with efficiencies over 80%, independently of the position, and with a dc voltage of 55 V, independently of the position and load. The same section also introduces an optimized Class E rectifier, able to reflect a zero reactance to the inverters and to maintain a load independent dc output voltage. An important aspect of this solution is the possibility to passively sense the position of the receiver only by a readout of currents in the transmitters. Section 2.5 complements the IPT link with a high data throughput link, with a bandwidth of over 100 Mb/s, again position independent. A network solution is also provided, which consents the elements of the system to communicate with each other.

Finally, a solution for rotation independent implants is discussed in chapter 3. This scenario requires lower powers and presents very low couplings, therefore with sensibly different requirements compared to the previous chapters.

Chapter 2

Sliding Inductive Power Transfer

"And yet it moves."

- Galileo Galilei -

This chapter describes the design, realization and measurements of a complete data and power transfer system for sliding applications. There are endless possible industrial applications but we are focusing on those requiring around a hundred of watts. A mover, as will be discussed in the following, is an industrial equipment which can move over a certain path, stop in certain positions and perform some tasks. The requirement for wireless powering can be to reduce wear and extend time between periodic maintenances or also to avoid contaminating the environment with dust produced by the sliding contacts. This second case can be for example related to machines in the drug production industry.

While moving on this path, the mover needs to be powered, which can be done using rechargeable batteries, with the issue of recharging them, their cost and life time. A more sensible solution is to continuously power the mover, without any need of battery or using the battery as a backup solution. Having metallic contacts is not a viable solution, due to safety and practical reasons, as its reliability under dirt or water. A possible solution is to power the mover via a Resonant Inductive Power Transfer link, since there are no contacts, and therefore parts subject to wear or posing safety issues, and the efficiency on the coupled link can be very high, easily over 95%. The problem is how to design such links to be position independent.

An issue in designing a Resonant IPT link is the need of high frequencies, in the MHz range, to improve the efficiency of the link. Soft switching inverters, for example employing the Zero Voltage Switching (ZVS) technique, are very efficient at high frequencies, but maintaining the ZVS, and therefore efficient conversion, while the load changes is an open issue. Furthermore, a load change also affects the output voltage, which then would require an additional regulator.

On the other side, the mover usually needs to have a data link, which is used to communicate information, servicing or receiving commands. Industrial environments are electromagnetically very noisy and the interference imposes techniques specific to these environments, resulting in expensive equipments. An alternative solution is to provide high power received signals, which can maintain high signal to noise ratios even in presence of strong interference. This solution can work using cheap consumer hardware, but would require very short distances.

The methods described in this chapter provide a framework to design a complete load and position independent IPT link, which can also sense indirectly, using only informations at the transmitting side, the position of the receiver. It also provides a position independent high throughput data link, which reuses the same previous structure and provides a rugged data link using consumer hardware.

2.1 Geometrical Optimization for Constant Coupling

A first step in achieving position independent powering is to demonstrate that a geometrical optimized receiver with two active transmitters are able to maintain a constant coupling coefficient.

Traditionally, to solve the problem of variable couplings, long primary current loops are adopted [69]. Long transmitting coils provide large primary inductances, but both the area and the conductor perimeter increases proportionally to the length, hence without increasing the quality factor (eq. (1.15)). The large leakage inductance means also low coupling and therefore the efficiency is eventually affected. Other possible additional effects are the radiation losses, which can be an issue with large structures and increase sensibly the losses, and the parasitic capacitances, which can introduce stray resonances and strongly affect the system behaviour.

As an alternative, we propose an optimized segmentation of the transmitters that allows a more energy efficient powering of the sliding path. By activating only two transmitting coils at a time and by sliding the movable one over them, we demonstrate that an optimum choice of the RX and TX reciprocal coil lengths exists, enabling a constant coupling coefficient, and thus a constant power transfer and efficiency, during the RX coil translation. Two transmitters is the minimum number to achieve the desired behavior.

A zero order approximation of the field in coils can provide an initial guess for the length of the receiver, which will be then analyzed with a full wave EM simulation. The approximation uses the following assumptions:

- The magnetic field is constant inside each coil: if multiple turns are considered, the field inside the inner coils is simply the superposition of all the fields from the outer coils (the simplified analysis is done with two turns);
- The magnetic field is zero outside;
- The two active Tx coils have the same magnetic field;
- The conductor is treated as a thin wire.

The first two assumptions are equivalent to assume the coils as solenoids, which have a null field outside and uniform inside. With these assumptions, the transmitters contribute to the shared magnetic field only when there is a geometrical overlap of the receiving coil on the transmitting ones. These are strong assumptions, but they will be demonstrated to be a good starting value for the successive full-wave optimization. The third assumption, both coils having the same magnetic field, requires the same currents in the transmitters and the implications will be discusses in the following of this section.

Then, in order to keep it simple, we opted for a graphical demonstration which is quite easy to obtain. A symbolic proof is obviously more formal and might be possible, but very clumsy for this simple case and probably an overkill.

The first step is to consider fig. 2.1, where the receiver is included with the dimensions of (see eq. (2.1)):

$$l_{RX} = l_1 + \frac{l_2 - l_1}{2} + g. \tag{2.1}$$

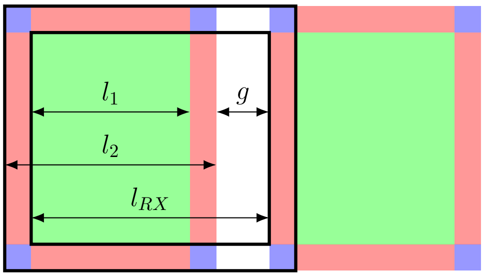

Figure 2.1: Simplified coil's structure in the initial position to demonstrate eq. (2.1)

In order to compute the total shared flux, since the magnetic field is approximated as constant, the only need is to find the shared areas and then the shared flux is simply a multiplication of the magnetic field with the shared area. The coils are made of two turn and therefore the area is composed of two contributions, which are the sum of inner and outer coil areas. Note that the inner area is shared between both turns.

By looking at fig. 2.1:

- The inner loop of the receive coil shares an area indicated with green, which is counted twice because there are two turns in the transmitter, and one vertical red area;
- The outer loop of the receive coil shares an area composed of six blue squares, three vertical and two horizontal red areas and again two green areas, which are counted twice because of the two turns in the transmitter;
- The total receive coil shared area for this snapshot is therefore composed of six blue areas, four vertical and two horizontal red areas and four green areas.

The receiver is now slid right of the same length as the distance between the two turns (the blue square), as in fig. 2.2. The second step is to evaluate the area which is removed:

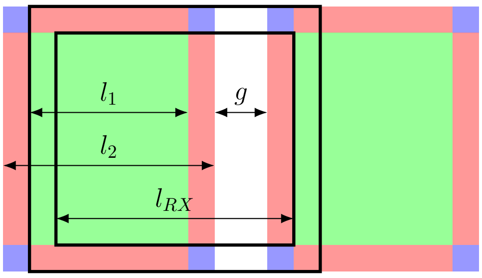

Figure 2.2: Simplified coil's structure in a successive position to demonstrate eq. (2.1)

- The shared area of the inner receive coil has lost two green slices (still counted twice) from the left side of the transmitter, which are equivalent to two vertical red areas (since the length of the movement was done on purpose to be equal to the distance between the transmitter's turns);

- The shared area of the outer receive coil has lost from the left side of the transmitter two blue squares and one vertical red areas;
- The total receive coil shared area for this position has therefore lost from the left side two blue squares and three vertical red areas.

Now what is reintroduced from the right tx is:

- The shared area of the inner receive turn has included one vertical red area from the right side;
- The outer turn of the receive coil has included two small red squares of areas equivalent to two blue squares, and two slices of green areas, which are equivalent to two vertical red areas;
- The total receive coil shared area for this position has therefore included from the right two blue areas and three vertical red areas.

The difference in shared flux between the two positions is therefore zero. From now onwards it is straightforward to see what goes out and what goes in, which is obviously the same and therefore confirms that the l_{RX} in eq. (2.1) is the optimum length of the receiver under previous assumptions.

Probably now the reader is guessing how good the assumptions would be and if they provide an adequate solution. The best way to answer this question, which takes also into account all the parasitics, is to do a full-wave simulation of the entire structure, as shown in fig. 2.3, with the receiver in different positions for a set of different lengths of the receiving coil. The output of the simulator is the impedance matrix of the three port network, which allows to evaluate the performances in each position with a defined Figure of Merit (FoM).

This kind of simulations, if the model is accurate enough, provides realistic results. Indeed, in the MHz range, it is quite straightforward to create a realistic 3D model. Anyway, setting the simulator in the proper way for these frequencies is not obvious, in particular if a full-wave solver is used to include the possible radiative losses. The meshing should be accurate enough that, if increased, the variation of the impedance matrix should be limited, for example under 1%. The default values, which are intended for RF simulations, are not fine enough for simulating IPT coils, which are not intended to radiate and therefore their size is much smaller than the wavelength (they are approximately quasi-stationary). It should be noted that, while in propagative structures the mesh should be adequate to properly approximate the wavelength, in quasi-static coils it should be adequate to approximate the structure. This has the consequence of a faint dependence of the mesh size on the wavelength and therefore it is be more sensible to use a fixed mesh density, independent of the wavelength. An alternative approach is to set the same mesh size related to the lowest frequency in the structure and allow the simulator to increase the number of cells for higher frequencies. When the characterization is at a single frequency, the two approaches are equivalent, while with a spectrum it would add complexity and simulation time due to the excessively denser mesh for the higher frequencies.

CST Microwave Studio has a large and continuously increasing number of solvers, but the main two general full-wave EM solvers are the Transient and the Frequency solvers. The Transient solver, which is the main CST solver, is well suited to broad-band problems. It requires the energy to decay and therefore it works best if there are not strong resonances in the electromagnetic structure to be simulated, which would increase the simulation time or return wrong results. The Frequency solver is better suited for narrow-band problems and works very well with strong resonances. Since an IPT link is single frequency by its nature, the frequency solver is the best choice. Moreover, when the parasitic capacitances of the coil start to resonate with its inductance, which is not a radiative process and the resulting resonator can have a very high quality factor, the frequency solver will tackle this easily. On the other hand, the transient solver would need a very long time.

The magneto-static solvers provides faster results, but neglecting the capacitive parasitics can make huge difference in MHz air coils and can return unreliable results.

The structure is shown in fig. 2.3. Each position for each receiver length l_{RX} is a different simulation: there are 11 lengths and 20 positions, for a total of 220 EM simulations. The receiving coil slides from the position in a), where its center is aligned with the center of the first transmitter, to the

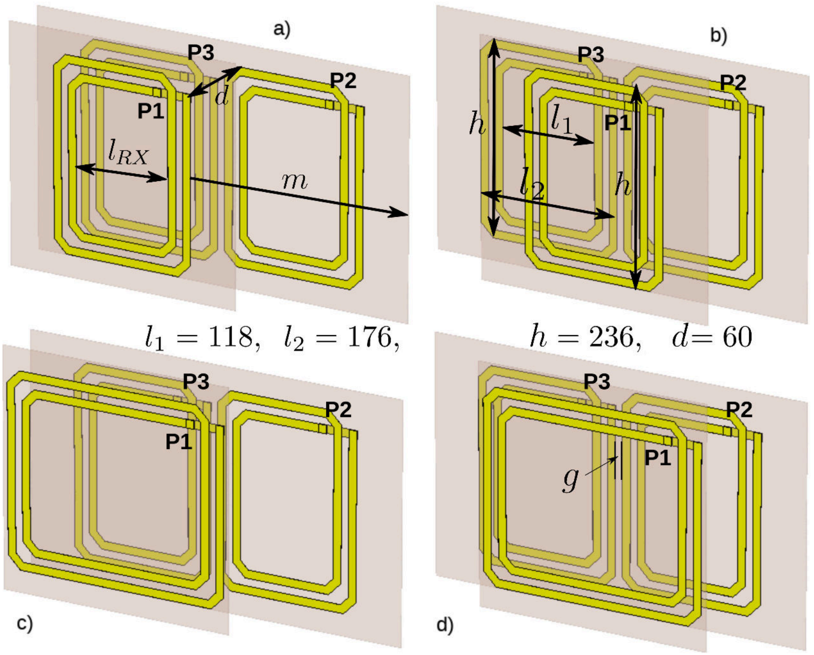

Figure 2.3: Structure simulated in CST. For each different length of the receiver, the receiving coils slides from the position in a), where its center is aligned with the center of the first transmitter, to the position in b), where its center is midway between the two transmitters. The material is FR4 and the coils are made of 35 µm thick copper.

position in b), where its center is midway between the two transmitters.

The standard FoM for resonant IPT is the $k_{i,j}^2 Q_i Q_j$ product: in this case, to simplify the analysis we will neglect the losses, by using only the imaginary parts in the impedance matrix, and consider only the coupling coefficient (eq. (1.7)) as a FoM to measure how the link variates. This is also a sensible solution if the goal is a constant output voltage, which is mainly related to the mutual inductance and therefore there is a strong relation with the coupling coefficient.

Ideally, the three coils link, which has the moving receiver, should behave as a static two coils link for the transmitter and receiver. There are different ways to provide a black box equivalent and the easiest is to reduce the size of system by connecting the transmitters in series or in parallel.

Before talking about the connection, it is interesting to see how the coupling between a single transmitter and the receiver changes varying the position and size of the receiver [3]. Fig 2.4 shows why, if a single transmitter is desired, the solution must be a very long transmitter. This is affected by the issues discussed before and motivates the move to two transmitters.

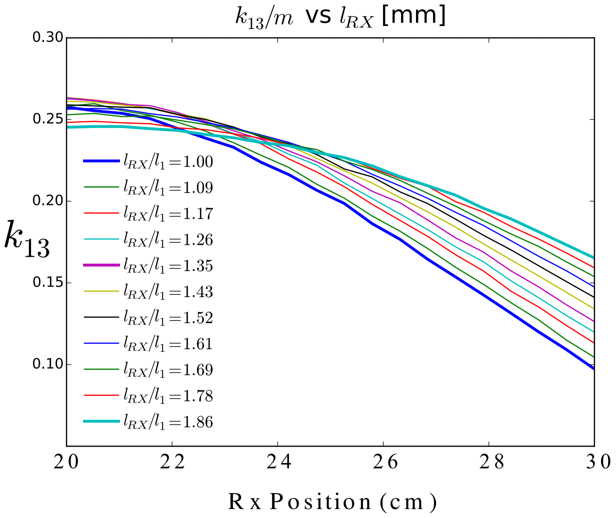

Figure 2.4: Simulated coupling coefficient between a transmitter and a receiver. Without any connection, in order to get a flat coupling, the receiver should be very long.

2.1.1 Series Connection of the Transmitters

The first possibility is the series connection of the two transmitters, as in fig. 2.5.

Consider the impedance matrix $\boldsymbol{Z}$ of a three port network, where Z_{ij}

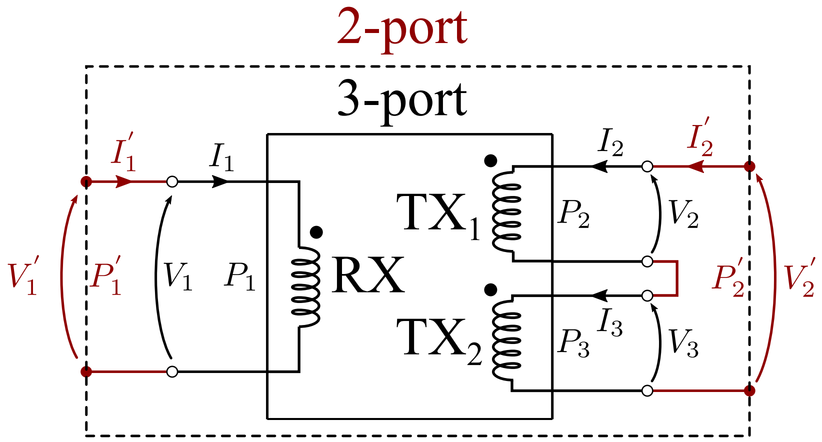

Figure 2.5: Schematic representation of the series connection between the two transmitting coils.

are its elements. The three port network can be expressed as:

$$\begin{aligned} V_1 =& Z_{11}I_1 + Z_{12}I_2 + Z_{13}I_3 \\ V_2 =& Z_{21}I_1 + Z_{22}I_2 + Z_{23}I_3 \\ V_3 =& Z_{31}I_1 + Z_{32}I_2 + Z_{33}I_3 \end{aligned} \tag{2.2}$$

The coupling coefficients between the three coils, if the port 1 is the receiver and 2,3 the transmitters, are:

$$\begin{aligned} k_{RX_1} &= \frac{\operatorname{Im}(Z_{12})}{\sqrt{\operatorname{Im}(Z_{11})\operatorname{Im}(Z_{22})}} \\ k_{RX_2} &= \frac{\operatorname{Im}(Z_{13})}{\sqrt{\operatorname{Im}(Z_{11})\operatorname{Im}(Z_{33})}} \\ k_{TX} &= \frac{\operatorname{Im}(Z_{23})}{\sqrt{\operatorname{Im}(Z_{22})\operatorname{Im}(Z_{33})}} \end{aligned} \tag{2.3}$$

Since the transmitters are connected in series, it is possible to say:

$$\begin{aligned} I_2 = I_3 &= I_2' \\ V_2 + V_3 &= V_2' \\ I_1 &= I_1' \end{aligned} \tag{2.4}$$

and the two port network with the transmitters connected in series is given by:

$$\begin{aligned} V_1^{'} =& Z_{11} I_1^{'} + \left(Z_{12} + Z_{13}\right) I_2^{'} \\ V_2^{'} =& \left(Z_{21} + Z_{31}\right) I_1^{'} + \left(Z_{22} + Z_{23} + Z_{32} + Z_{33}\right) I_2^{'} \end{aligned} \tag{2.5}$$

The resulting two ports is represented by the impedance matrix $\boldsymbol{Z'}$:

$$\begin{aligned} Z_{11}^{'} &= Z_{11} \\ Z_{12}^{'} &= Z_{12} + Z_{13} \\ Z_{21}^{'} &= Z_{21} + Z_{31} \\ Z_{22}^{'} &= Z_{22} + Z_{23} + Z_{32} + Z_{33} \end{aligned} \tag{2.6}$$

One important result from eq. (2.6) is that $Z_{11}^{'}$ and $Z_{22}^{'}$ do not change with the position, since all the terms there are constant. Note that Z_{23} and Z_{32} are fixed and $Z_{23} = Z_{32}$ because the linear passive network is reciprocal.

Therefore the reciprocal two port network with the transmitters connected in series is represented by the impedance matrix $\boldsymbol{Z'}$:

$$\begin{aligned} Z_{11}^{'} &= Z_{11} \\ Z_{12}^{'} &= Z_{12} + Z_{13} \\ Z_{22}^{'} &= Z_{22} + 2Z_{23} + Z_{33} \end{aligned} \tag{2.7}$$

The inductance of the resulting transmitting coil is simply $Z_{22}^{'}/j\omega$ and $Z_{11}^{'}/j\omega$ for the receiving one. The natural resonance of the resulting transmitting and receiving coils does not change with the position, which is a nice result for the design of the system.

Now, the coupling coefficient of this equivalent two coupled coils is given by:

$$k_{RX_S} = \frac{\mathrm{Im}\left(Z_{12} + Z_{13}\right)}{\sqrt{\mathrm{Im}\left(Z_{22} + 2Z_{23} + Z_{33}\right) \mathrm{Im}(Z_{11})}} \tag{2.8}$$

where the system has been considered reciprocal. Then, since the transmitters are assumed to be identical, $\mathrm{Im}(Z_{22}) = \mathrm{Im}(Z_{33})$. Hence

$$k_{RX_S} = \frac{1}{\sqrt{2}} \frac{\mathrm{Im}(Z_{12}) + \mathrm{Im}(Z_{13})}{\sqrt{\left(\mathrm{Im}(Z_{22}) + \mathrm{Im}(Z_{23})\right) \mathrm{Im}(Z_{11})}} \tag{2.9}$$

Using the relations of the coupling coefficient for the three port network

$$k_{RX_S} = \frac{1}{\sqrt{2}} \frac{k_{RX_1}\sqrt{\operatorname{Im}(Z_{11})\operatorname{Im}(Z_{22})} + k_{RX_2}\sqrt{\operatorname{Im}(Z_{11})\operatorname{Im}(Z_{33})}}{\sqrt{\left(\operatorname{Im}(Z_{22}) + k_{TX}\sqrt{\operatorname{Im}(Z_{22})\operatorname{Im}(Z_{33})}\right)\operatorname{Im}(Z_{11})}} \tag{2.10}$$

which using again $\operatorname{Im}(Z_{22}) = \operatorname{Im}(Z_{33})$ and simplifying:

$$k_{RX_S} = \frac{1}{\sqrt{2}} \frac{k_{RX_1} + k_{RX_2}}{\sqrt{1 + k_{TX}}} \tag{2.11}$$

Eq. (2.11) tells us that for the series connection it is sufficient to maintain $k_{RX_1} + k_{RX_2}$ constant to have a constant series coupling coefficient. The series connection provides the same effect of the previous approximated approach, since the same currents would provide the same magnetic fields in the two coils.

The approach can validated by using the results from the previous full wave simulation and by applying the expressions above.

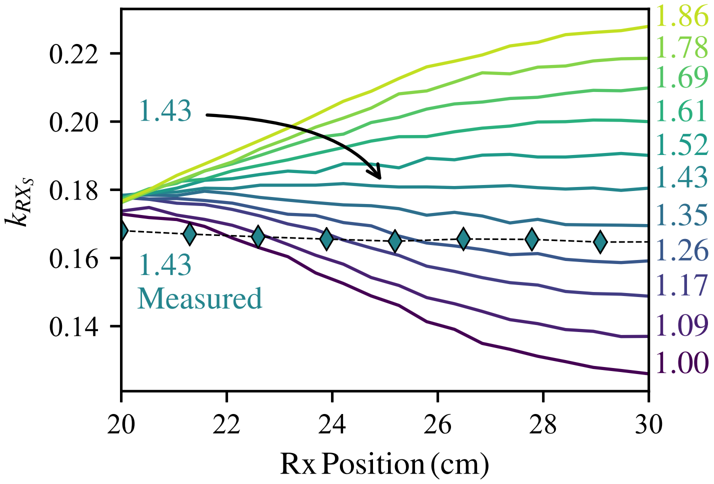

Figure 2.6: Coupling coefficient for different l_{RX}/l_1 with the transmitters connected in series. The measured data for $l_{RX}/l_1 = 1.43$ is plotted with diamond markers.

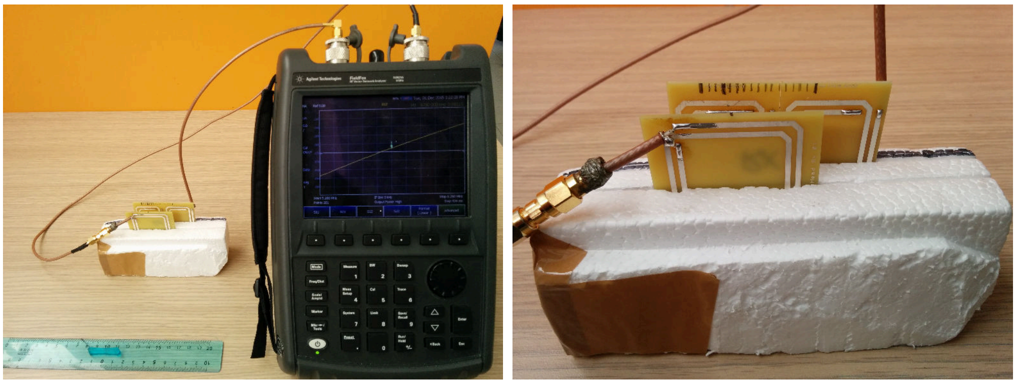

(a) (b)

Figure 2.7: Setup for the measurements. (a), connection to the VNA, (b), Device Under Test.

The simulated and measured results are plotted in fig. 2.6 for different lengths of the receiving coil. When $l_{RX}/l_1 = 1.43$, the resulting simulated series coupling coefficient (k_{RX_S}) is flat. Note that the approximated formula in eq. (2.1) provides $l_{RX}/l_1 = 1.42$, which is practically the same value. In order to validate the simulations, a simplified setup is built, as shown in fig. 2.7, which is a six times scaled down replica of the simulated structure. Being a scaled version, this would maintain the same coupling coefficient, since it depends only on the geometry, but would provide different parasitics and, de facto, an higher self resonance. The simulations for the full size version anticipated a self resonance above 70 MHz, with a constant inductance below 20 MHz after which the parasitics start to gain influence and the inductance became frequency dependent. The frequency dependence above 20 MHz means that the self resonance is starting to show its effects and the coil is not behaving anymore as a pure inductor. Since it is in the frequency range where it behaves as a pure inductor, it is fine to use a scaled replica to measure the coupling coefficients.

The measurements confirm the position independent coupling obtained from the simulations but have a small shift on its mean value, which is probably due to a slight different distance in the prototype. One of the drawbacks of a scaled down structure is that it is much more sensitive to a possible mechanical tolerance in the setup. A 1 mm variation in the distance is a mere 1.5% in the full size structure but a 10% in the scaled replica. The near-field is very sensitive to mechanical variations of the structure, meaning that the error in the coupling coefficient would be magnified. The measurements show a coupling coefficient of about 90% of the simulated equivalent, which is in a reasonable error range. Moreover, the variation of the coupling coefficient is below the possible error due to the setup, with an average value of 0.175, a standard deviation of 0.0012 and a maximum variation of 1.3%.

Now, it is also interesting to check the variations with the distance to see if the flatness is retained.

The approximated theory, with the assumption of constant field inside and zero outside, will still provide the same l_{RX}. Unfortunately, that model will also predict the same coupling, which is unrealistic. Anyway, if the magnetic field is symmetric to the center of each coil, $k_{RX_1} + k_{RX_2}$ in eq. (2.11) remains position independent and therefore also the series coupling. The previous prediction of same coupling is not necessary with this model and therefore a lower coupling is a possible solution, which is fine from a physical point of view.

In fig. 2.8, the coupling for different normalized orthogonal separation between the transmitters and receiver (d/l_1), with the transmitters connected in series and $l_{RX}/l_1 = 1.43$, is plotted for simulated and measured results. A higher distance provides a lower coupling, as expected, and maintains a constant coupling. The lowest distance has a worse flatness because of secondary effects: the conductor trace width is comparable with the distance. Anyway, the variation is still limited.

It should be noted that the demonstrated constant coupling coefficient is obtained by the concurrency of the layout optimization, that ensures the spatial periodicity, and the series connection of two transmitters, that are satisfied by a moving system along a linear path. On the contrary, a rotation or a lateral displacement that deviate the system from such periodicity can cause a degradation of the coupling coefficient. This effect can be easily seen from the qualitative proof in section 2.1.

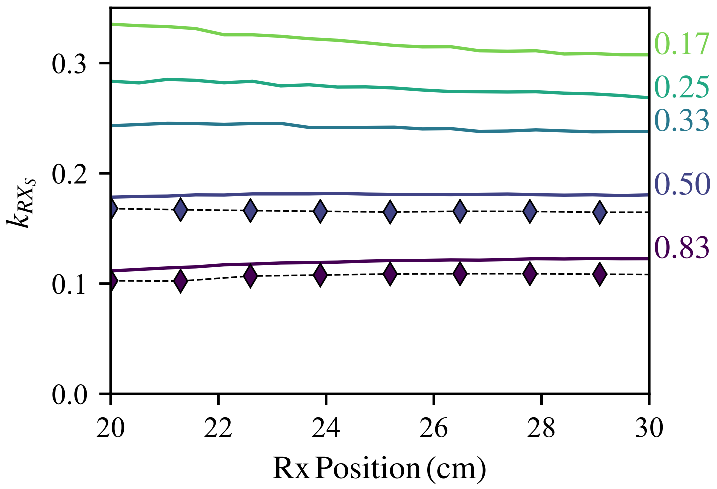

Figure 2.8: Coupling coefficient for different d/l_1 with the transmitters connected in series and $l_{RX}/l_1 = 1.43$. Measured data is plotted with diamond markers.

2.1.2 Parallel Connection of the Transmitters

The other possibility is the parallel connection of the two transmitters, as in fig. 2.9.

Consider the same impedance matrix $\boldsymbol{Z}$ an in eq. (2.2). Since the transmitters are connected in parallel, it is possible to say:

$$\begin{aligned} I_1^{'} &= I_1 & V_1^{'} &= V_1 \\ V_2^{'} &= V_2 = V_3 & I_2^{'} &= I_2 + I_3 \end{aligned} \tag{2.12}$$

which results in:

$$\begin{aligned} V_1^{'} &= \left(Z_{11} - \frac{Z_{12}\left(Z_{21}-Z_{31}\right) - Z_{13}\left(Z_{21}-Z_{31}\right)}{Z_{22}-Z_{23}-Z_{32}+Z_{33}}\right) I_1^{'} + \frac{Z_{12}\left(Z_{33}-Z_{23}\right) + Z_{13}\left(Z_{22}-Z_{32}\right)}{Z_{22}-Z_{23}-Z_{32}+Z_{33}} I_2^{'} \\ V_2^{'} &= \frac{Z_{21}\left(Z_{33}-Z_{32}\right) + Z_{31}\left(Z_{22}-Z_{23}\right)}{Z_{22}-Z_{23}-Z_{32}+Z_{33}} I_1^{'} + \frac{Z_{22}Z_{33}-Z_{23}Z_{32}}{Z_{22}-Z_{23}-Z_{32}+Z_{33}} I_2^{'} \end{aligned} \tag{2.13}$$

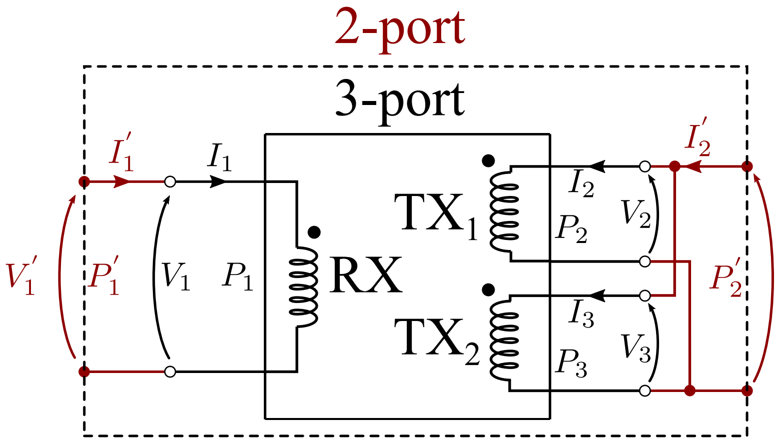

Figure 2.9: Schematic representation of the parallel connection between the two transmitting coils.

The resulting two ports is represented by the impedance matrix $\boldsymbol{Z}'$:

$$\begin{aligned}
Z_{11}' &= Z_{11} - \frac{Z_{12}\left(Z_{21}-Z_{31}\right) - Z_{13}\left(Z_{21}-Z_{31}\right)}{Z_{22}-Z_{23}-Z_{32}+Z_{33}} \\
Z_{12}' &= \frac{Z_{12}\left(Z_{33}-Z_{23}\right) + Z_{13}\left(Z_{22}-Z_{32}\right)}{Z_{22}-Z_{23}-Z_{32}+Z_{33}} \\
Z_{21}' &= \frac{Z_{21}\left(Z_{33}-Z_{32}\right) + Z_{31}\left(Z_{22}-Z_{23}\right)}{Z_{22}-Z_{23}-Z_{32}+Z_{33}} \\
Z_{22}' &= \frac{Z_{22}Z_{33}-Z_{23}Z_{32}}{Z_{22}-Z_{23}-Z_{32}+Z_{33}}
\end{aligned} \tag{2.14}$$

One important result from eq. (2.14) is that Z_{22}' does not change with the position, since all the terms there are constant, but Z_{11}' is position dependent.

This is an important difference from the series connection, where both the equivalent inductances of the two ports were position independent. Imagine an inverter connected to the transmitter, which is the port 2. When the receiver slides, the inductance seen from the inverter changes, affecting its behaviour (for example the ZVS).

Note that Z_{23} and Z_{32} are fixed and that the linear passive network is reciprocal and therefore the impedance matrix $\boldsymbol{Z}'$ is:

$$\begin{aligned} Z'_{11} &= Z_{11} - \frac{\left(Z_{12} - Z_{13}\right)^2}{Z_{22} - 2Z_{23} + Z_{33}} \\ Z'_{12} &= \frac{Z_{12}\left(Z_{33} - Z_{23}\right) + Z_{13}\left(Z_{22} - Z_{23}\right)}{Z_{22} - 2Z_{23} + Z_{33}} \\ Z'_{22} &= \frac{Z_{22}Z_{33} - Z_{23}^2}{Z_{22} - 2Z_{23} + Z_{33}} \end{aligned} \tag{2.15}$$

and the coupling coefficient results to be:

$$k_{RX_P} = \sqrt{\frac{\left(k_{12} + k_{13}\right)^2\left(1 - k_{23}\right)}{\left(1 + k_{23}\right)\left[2\left(1 - k_{23}\right) - \left(k_{12} - k_{13}\right)^2\right]}} \tag{2.16}$$

Eq. (2.16) tells that there is not any k_{12} and k_{13} which provides a constant k_{RX_P}.

When k_{12} and k_{13} are small, which could be below 0.2, $\left(k_{12} - k_{13}\right)^2$ is negligible and $k_{RX_P} = k_{RX_S}$. Hence, for low couplings, the parallel connection can have a flat coupling and the l_{RX} is the same as the series connection. Furthermore, the variation of Z'_{11} in eq. (2.15) is also small. Anyway, even a small variation could detune the inverter [1] and therefore the effect is more serious and unpredictable.

Previous approximated analysis is not valid for this case, because the parallel connection does not provide the same magnetic field in the two coils. The simulated results are plotted in fig. 2.10 for different lengths of the receiving coil. Measured results are not provided because the series connection was selected for its superior and safer characteristics and therefore a prototype was not built. As previous measurements were in good agreement with the simulations, we expect them to be reliable. Indeed, both uses the same simulated impedance matrix of the three port, which is then post processed using Python to include the connection.

Again, it is interesting to see the variations with different distances which are shown in fig. 2.11. As expected, at low couplings the difference with the series connection is negligible, but it is well visible at higher couplings.

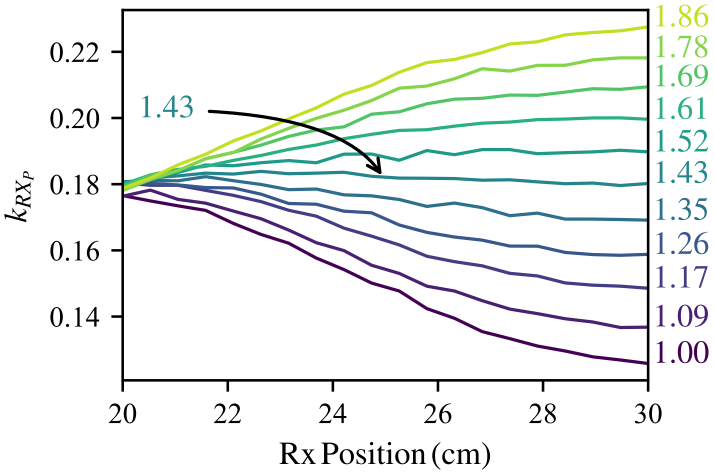

Figure 2.10: Coupling coefficient for different l_{RX}/l_1 with the transmitters connected in parallel.

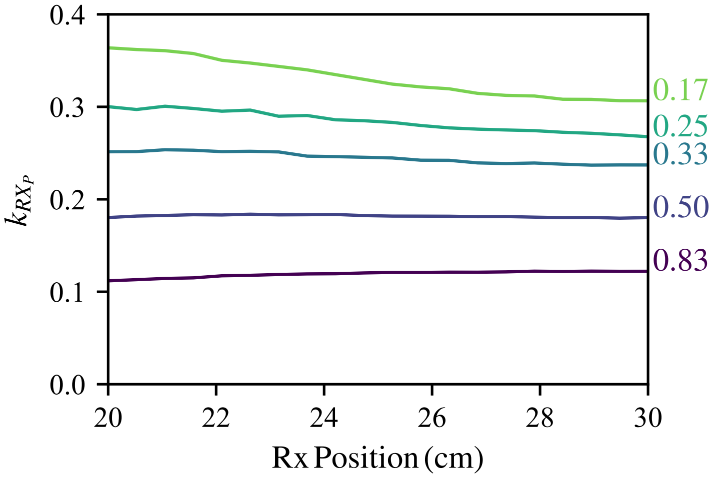

Figure 2.11: Coupling coefficient for different d/l_1 with the transmitters connected in parallel and $l_{RX}/l_1 = 1.43$.

2.1.3 Remarks

- Series Connection:
  - The series connection is able to provide a constant coupling coefficient with a simple geometrical optimization;
  - The equivalent inductances to be compensated are independent of the position;
  - The approximated eq. (2.1) provides the optimum l_{RX}, as confirmed by simulations and measurements.
- Parallel Connection:
  - The parallel connection cannot provide a constant coupling coefficient with a simple geometrical optimization at all couplings;
  - At low couplings it is approximately flat and the same eq. (2.1) provides the optimal l_{RX};
  - The equivalent inductance to be compensated at the transmitter is position dependent, which is a major drawback for the design of the inverter.
- The results are for structures that can be adapted for different needs, as distances, powers and frequencies, by simply scaling the entire structure;
- The parasitics do not scale and require a careful evaluation for the operating frequency, ideally with a full-wave EM simulation.

This page was intentionally left blank.

2.2 Unlimited Path using N-Transmitters

Two coils are not sufficient to provide a position independent power transfer: the distance is limited to the space between the centers of the two transmitting coils.

A simple method is able to replicate the behavior by shifting the active coils. The space-periodic path is schematically represented in fig. 2.12, where the active coils are outlined depending on the Rx positions. In case (I) only TX_2 and TX_3 are powered, an this condition is fine for movements from 20 cm to 40 cm, in the full size structure.

When the receiver axis aligns with the TX_3 axis, case (II), TX_2 must be turned off and TX_4 must be activated, allowing to periodically reproduce the same behavior from 20 cm to 40 cm. Therefore, the spatial periodicity of the system enables a theoretically unlimited path.

The idea is extremely simple as a concept, but the implementation can be very complicated. In the next sections, two methods are discussed for its implementation: in section 2.3 the implementation uses a switch network to connect the coils in physical series, while in section 2.4 the series is performed virtually by forcing the same current with efficient switch-mode current sources.

It is noteworthy that the proposed layout is suitable for powering multiple receivers by selectively enabling the proper coils pairs.

2.2.1 Remarks

- The two coils system can be used for extended paths;
- When the receiver aligns with the following coil the preceding is deactivated and the following activated;
- The path is theoretically unlimited in length.

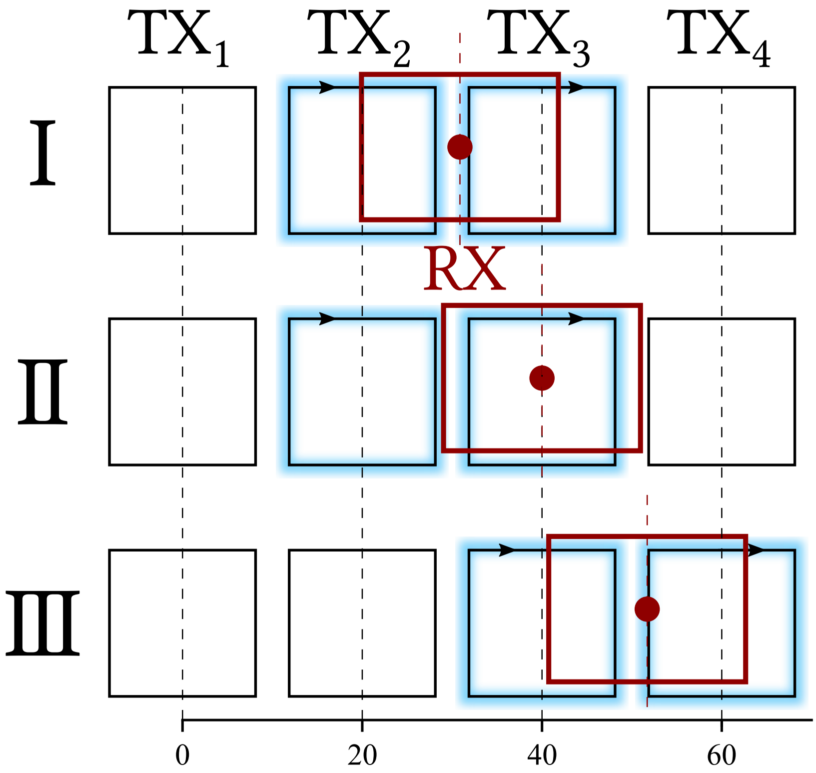

Figure 2.12: A pair of series-connected Tx coils, in blue, with respect to the Rx positions (cm), in red. I and III correspond to all the Rx coil positions located between two subsequent Tx coils. II shows the Rx position where Tx coils switching is needed: TX_2 is deactivated and TX_4 activated. The sequence is repeated all over the transmitting path.

2.3 Real Series Connection

In this section, the issues of implementing this kind of moving system, powered by a unique ac source, are studied. As discussed in section 2.1, the series connection is preferable over the parallel one for its superior characteristics. We name this method the “Real Series” from the physical series connection, which is performed using switches.

In the following, the design of a suitable network, whose role is to ensure the series connection between two subsequent coils, is presented [4]. The procedure is divided into states: the stable states are intended to transfer power and the intermediate states, which are temporary states, are not intended to transfer power and are only required for the switching mechanism to operate safely. For each intermediate state which occurs while the active coils are changed, the main issue is to keep under control voltage spikes and over-currents, which is accomplished by a proper choice of the compensating circuit elements of the Tx chain. Specifically, the real dynamic behavior of the switches, including the unavoidable asynchronous switching times, must be considered in the design to avoid current discontinuities through the coils. The design and experimental verifications are carried out at 6.78 MHz, chosen to verify the proposed design approach under severe parasitic effects, which are introduced by the switch network and are discussed in this section. Anyway, the natural application of such a system is for scenarios where the use of multiple inverters along the path [1], [5] is not convenient and better powered by a single ac source, but with a frequency which avoids the effect of parasitics. It will be shown that it translates to low frequency and high power links.

The coils are the same as used in section 2.1, therefore the scaled replica, as shown in fig. 2.13.

The proposed implementation has a voltage-fed source and a T-immittance inverter (see fig. 2.14) at the receiver side [70], which uses the inductance of the Tx coils to reduce the number of components and an uncoupled Rx coil to obtain L'_{RX}. In combination with the inverting behavior of a resonant inductive link, the whole system acts as a voltage transformer (double T-immittance inverter (LCL - LCL)): if the input voltage amplitude is constant, the output voltage amplitude is also constant. It also provides

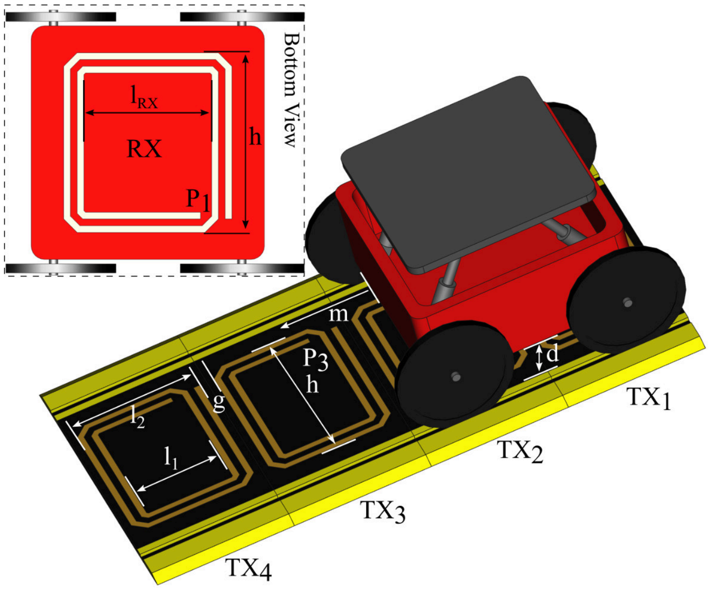

Figure 2.13: Sketch of a wireless powered mover, with a sequence of transmitters and one receiver; only two transmitters are active at a time. P_1, P_2 (on TX$_2$, covered by the RX), P_3 are the WPT-link ports; d is the Tx-to-Rx distance; h, l_1 and l_2 are the Tx-coil geometrical parameters; g is the distance between the Tx-coils; l_{RX} is the Rx coil length; m is the lateral Rx-to-Tx displacement. Dimensions of the designed and measured prototype (mm): $l_1 = 20$, $l_2 = 30$, $h = 40$, $d = 10$, $l_{RX} = 28.5$, $g = 3.5$.

an input impedance which is proportional to the load impedance as:

$$Z_{\text{in}} = \frac{{M'_{12}}^2}{{L'_{RX}}^2} Z_{\text{load}} \tag{2.17}$$

where $M'_{12} = \text{Im}(Z'_{12})$. Eq. (2.17) can be straightforwardly obtained cascading two T-immittance inverters at resonance.

2.3.1 Ideal Dynamical Conditions

Fig. 2.15 shows the active section of a slice of the WPT system composed by the moving Rx and two Tx coils, two capacitors and 6 switches. The

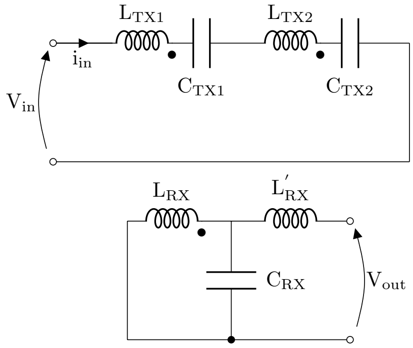

Figure 2.14: Equivalent link as shown in section 2.1. The immittance inverter at the receiver side, in combination with the inverting behavior of a resonant inductive link, provides a transformer-like behavior.

entire Tx side is composed of a periodic connection of identical modules of this kind.

Let the moving receiver be located between the first and the second Tx coils. In such conditions these two coils are powered and the switches SW_{U1}, SW_{S1}, SW_{S2}, SW_{D3} are closed (fig. 2.15). This configuration is the normal situation and is maintained, while the receiver is moving continuously, until it is in front of the second Tx and their axes are aligned.

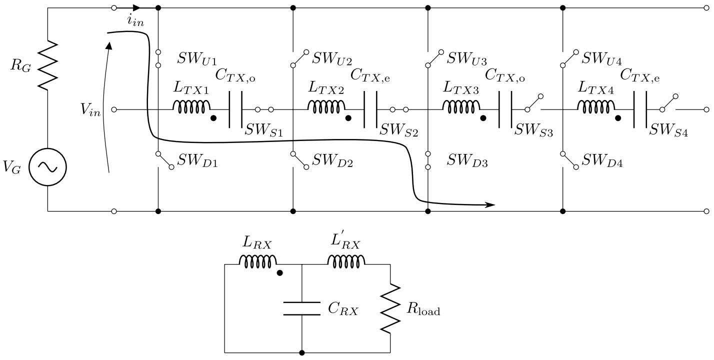

Figure 2.15: Equivalent circuit of the modular WPT link: two subsequent couples of the Tx coil are shown with the Rx located between the first two Tx coils, see fig. 2.12 (I). The current path is outlined.

When the receiver moves beyond the center of the second Tx coil, the first one must be disconnected and the third one is powered, as shown in fig. 2.16.

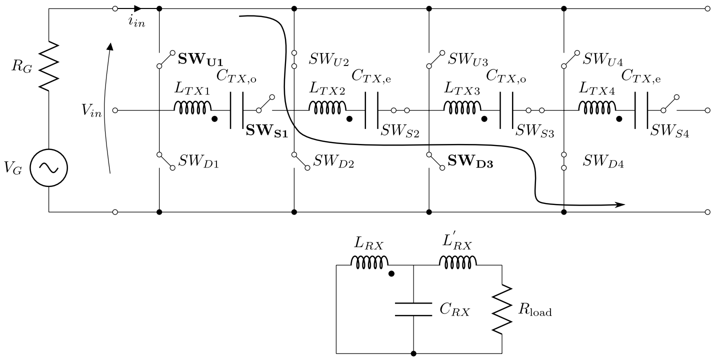

Figure 2.16: Circuit representation of the modular WPT link when the Rx coil is located between the second and the third Tx coils: the associated current path is outlined.

Since a direct transition from the state of fig. 2.15 to that of fig. 2.16 would cause current discontinuities, the switches SW_{U2}, SW_{S3}, SW_{D4} must be closed before SW_{U1}, SW_{S1}, SW_{D3} are opened. In this way, the intermediate and temporary state, represented in fig. 2.17 is introduced. This state will be referred to as "State A". The system is not meant to transfer power in these temporary states, but they are necessary to allow a seamless change between the active coils. It can be observed that, in this configuration, the first resonator is short-circuited by the switches SW_{U1}, SW_{U2} and, similarly, the third resonator is short circuited by the switches SW_{D3}, SW_{D4}. In such conditions, a current is induced in the loop formed by the shorted resonators (see fig. 2.17), which can reach excessively high values and compromise the switches. To avoid this critical condition, two different values, $C_{Tx,o}$ and $C_{Tx,e}$, are adopted for the capacitances connected in series to the odd and to the even coils, respectively. The capacitances are chosen in such a way that the resonance condition is achieved when a couple of Tx coils are connected in series, but the impedance of the short-circuited LC branches in fig. 2.17 (TX1 and TX3), at the operating frequency, is large enough to inhibit over-current. It can be observed that in state A the system is no longer resonant, and this causes a reduction of the transmitted power. However, since the system remains in this state only for the brief time required for the transition from the configuration of fig. 2.15 to that of fig. 2.16, the effect on the overall performance is negligible.

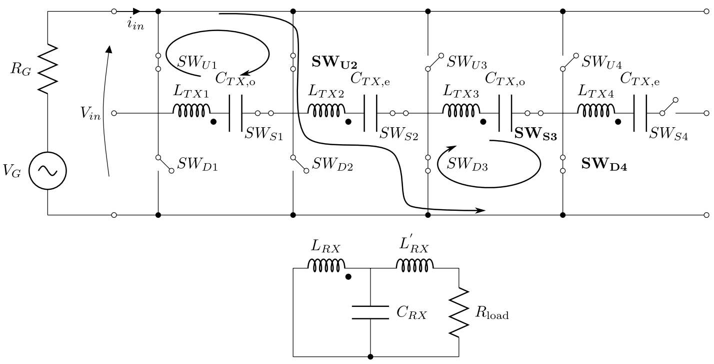

Figure 2.17: Intermediate state required to maintain current continuity ("State A"). The switches SW_{U2}, SW_{S3}, SW_{D4} are closed, before SW_{U1}, SW_{S1}, SW_{D3} are opened. Two potentially critical closed loops are created.

2.3.2 Real Dynamical System

In real scenarios, the switch commutations cannot be assumed perfectly synchronous. To effectively analyze the system behavior during switches commutations, additional intermediate states can be experienced, besides the one depicted in fig. 2.17. They are represented in figs. 2.18 and 2.19 and can be referred as "State B" and "State C". Two other states, obtained interchanging the first and the third resonators, are possible, but are not considered explicitly, since the results derived for states B and C also apply in those cases.

As in state A, in states B and C, the over-current in the shorted loop can be avoided by a suitable choice of the capacitance values, as it will be shown in the following.

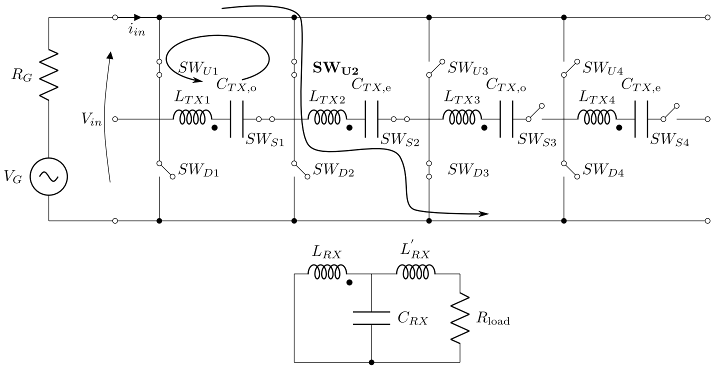

Figure 2.18: Temporary states due to the not synchronous commutation of the switches, the switch SW_{U2} gets closed before SW_{S3} or SW_{D4} ("State B").

2.3.3 Analysis of the Intermediate States

The proposed solution in order to avoid the over-currents is to resort to different values for the even and odd capacitances ($C_{Tx,o}$, $C_{Tx,e}$). The decision about their values is made by means of analyses carried out in states A, B, and C, aimed at establishing the dependence of the currents in the coils on the capacitance ratio α:

$$\alpha = \frac{C_{Tx,o}}{C_{Tx,e}}. \tag{2.18}$$

Since the series connection of two consecutive LC branches must resonate at the operating angular frequency, ω, the capacitances must also satisfy the condition

$$\frac{C_{Tx,o}C_{Tx,e}}{C_{Tx,e}+C_{Tx,e}} = \frac{1}{\omega^2 L_{Tx}} \ . \tag{2.19}$$

In the last equation L_{Tx} is the inductance of the transmitter, i.e.: $L_{Tx} = L_{Tx1} + L_{Tx2} + 2M_{Tx}$, where M_{Tx} is the mutual inductance between two Tx coils. To reduce complexity and theoretically analyze the system in the intermediate states, the receiving coil is removed, thus representing a worst-case scenario. Indeed, without a receiver (and hence a load), the active Tx resonators exhibit the minimum impedance and, as a consequence,

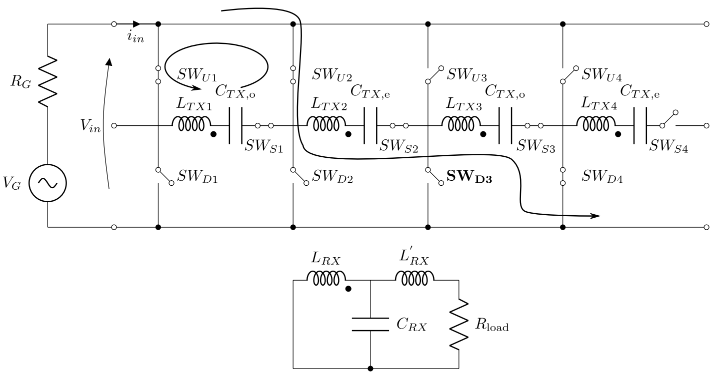

Figure 2.19: Temporary states due to the not synchronous commutation of the switches, the switch SW_{D3} gets open before SW_{U1} and SW_{S1} ("State C").

the current amplitudes are the highest, whereas a load would introduce an additional resistance. It should be obvious that, without a receiver, there is no coupling to be kept constant. This analysis is meant to remove the criticality at the Tx side, also avoided when the Rx is reintroduced.

R is intrinsic resistance of each Tx coil, which is supposed to equal for simplicity, and the current I_n is the current in the transmitting coil L_{TX_n}.

2.3.4 Loop Currents in Intermediate State A

For State A, the currents in the loops for the first ($\mathbf{I}_1$) and the third ($\mathbf{I}_3$) Tx coil can be derived by circuit analysis as follows:

$$\begin{aligned}
&\left(R + j\omega L_{Tx} - \frac{j}{\omega C_{Tx,o}}\right)\mathbf{I}_1 + j\omega M_{Tx}\mathbf{I}_2 = 0 \qquad (2.20)\\
&j\omega M_{Tx}\left(\mathbf{I}_1 + \mathbf{I}_3\right) + \left(R + j\omega L_{Tx} - \frac{j}{\omega C_{Tx,e}}\right)\mathbf{I}_2 = \mathbf{V}_{in}\\
&j\omega M_{Tx}\mathbf{I}_2 + \left(R + j\omega L_{Tx} - \frac{j}{\omega C_{Tx,o}}\right)\mathbf{I}_3 = 0.
\end{aligned}$$

where boldface letters represent the current and voltage phasors. It is convenient to define the normalized current amplitudes through the Tx coils as:

$$i_i = \frac{\omega L_{Tx}}{|\mathbf{V}_{in}|}|\mathbf{I}_i|, \tag{2.21}$$

with $i = 1, 2$, and hence to introduce the coil quality factor Q_{Tx} and the coupling coefficient k_{Tx} between the two adjacent Tx coils,

$$Q_{Tx} = \frac{\omega L_{Tx}}{R}, \quad k_{Tx} = \frac{M_{Tx}}{L_{Tx}}. \tag{2.22}$$

From (2.20), it is then possible to obtain the following expressions of the normalized current amplitudes as a functions of the capacitance ratio α:

$$\begin{aligned} i_1 = i_3 &= \frac{|k_{Tx}|\left(\alpha+1\right)^2 Q_{Tx}^2}{\sqrt{\gamma^2 + 4k_{Tx}^2\left(\alpha+1\right)^4 Q_{Tx}^2}} \\ i_2 &= \frac{\left(\alpha+1\right) Q_{Tx}\sqrt{\left(\alpha - 2k_{Tx} - 1\right)^2 Q_{Tx}^2 + \left(\alpha+1\right)^2}}{\sqrt{\gamma^2 + 4k_{Tx}^2\left(\alpha+1\right)^4 Q_{Tx}^2}}, \end{aligned} \tag{2.23}$$

where

$$\begin{aligned} \gamma = {} & \left(\alpha+1\right)^2 + \\ & \left[\left(2k_{Tx}+1\right)\left(\alpha-1\right)^2 + 2k_{Tx}^2\left(\alpha^2+1\right)\right] Q_{Tx}^2 \end{aligned}$$

2.3.5 Loop Currents in Intermediate State B

For state B, the currents in the loops can be determined by solving the equations

$$\begin{aligned} \left[R + j\left(\omega L_{Tx} - \frac{1}{\omega C_{Tx,o}}\right)\right]\mathbf{I}_1 + j\omega M_{Tx}\mathbf{I}_2 &= 0 \\ j\omega M_{Tx}\mathbf{I}_1 + \left[R + j\left(\omega L_{Tx} - \frac{1}{\omega C_{Tx,e}}\right)\right]\mathbf{I}_2 &= \mathbf{V}_{in}, \end{aligned} \tag{2.24}$$

In this case, using the definitions introduced in the previous sections, the normalized current magnitudes are expressed as

$$\begin{aligned} i_1 &= \frac{|k_{Tx}|\,(\alpha+1)^2}{\sqrt{\left[(k_{Tx}+1)^2(\alpha-1)^2+\frac{(\alpha+1)^2}{Q_{Tx}^2}\right]^2+\frac{4k_{Tx}^2(\alpha+1)^4}{Q_{Tx}^2}}} \\ i_2 &= \frac{Q_{Tx}^{-1}(\alpha+1)\sqrt{(\alpha-2k_{Tx}-1)^2Q_{Tx}^2+(\alpha+1)^2}}{\sqrt{\left[(k_{Tx}+1)^2(\alpha-1)^2+\frac{(\alpha+1)^2}{Q_{Tx}^2}\right]^2+\frac{4k_{Tx}^2(\alpha+1)^4}{Q_{Tx}^2}}} \end{aligned} \tag{2.25}$$

2.3.6 Loop Currents in Intermediate State C

In state C the loop currents are obtained by solving the equations

$$\begin{aligned} &\left[R+j\left(\omega L_{Tx}-\frac{1}{\omega C_{Tx,o}}\right)\right]\mathbf{I}_1+j\omega M_{Tx}\mathbf{I}_2=0 \\ &j\omega M_{Tx}\mathbf{I}_1+ \\ &\left(2R+2j\omega L_{Tx}-\frac{j}{\omega C_{Tx,e}}-\frac{j}{\omega C_{Tx,o}}\right)\mathbf{I}_2=\mathbf{V}_{in} \end{aligned} \tag{2.26}$$

which provide

$$\begin{aligned} i_1 &= \frac{|k_{Tx}|\,(\alpha+1)}{\sqrt{(\alpha+1)^2\left(2+k_{Tx}^2Q_{Tx}^2\right)^2+4(\alpha-2k_{Tx}-1)^2}} \\ i_2 &= \frac{Q_{Tx}\sqrt{(\alpha-2k_{Tx}-1)^2Q_{Tx}^2+(\alpha+1)^2}}{\sqrt{(\alpha+1)^2\left(2+k_{Tx}^2Q_{Tx}^2\right)^2+4(\alpha-2k_{Tx}-1)^2}}. \end{aligned} \tag{2.27}$$

2.3.7 Optimum Odd and Even Capacitances

The current magnitudes with respect to the capacitance ratio, α, are shown in fig. 2.20. They are computed from the equations derived in the previous sections, assuming $Q_{Tx} = 20$ and $k_{Tx} = -0.0595$, which are the values derived for the realized prototype described in the next section. The same currents are also computed by circuital simulations, which are practically identical to the theoretical ones and are perfectly superimposed in fig. 2.20.

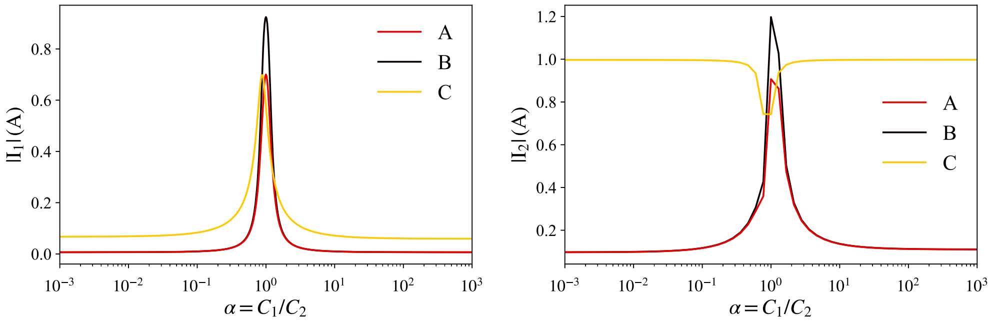

Figure 2.20: Magnitude of I_1 and I_2 when the system is in states A, B, and C. In state A the magnitude of I_3 is equal to the magnitude of I_1.

The maximum current amplitude of the shorted LC branches in states A and B, I_1, occurs for $\alpha = 1$, which corresponds to equal compensating capacitances, while it rapidly decreases and becomes practically negligible as α tends to zero or to infinity.

In state A the amplitude of I_3 has exactly the same behavior as the amplitude of I_1.

Similarly, the amplitude of I_2 has a peak for $\alpha = 1$, when the active LC branch resonates, and tends to a lower constant value for lower or higher values of α, when the branch impedance is dominated by a capacitive or by an inductive contribute.

State C exhibits a different behavior. In this case, two LC branches are simultaneously activated, and their series connection resonates for all values of α. When α is far from 1, this results in a higher amplitude of I_2. However, in these conditions, the shorted LC loop exhibits a high impedance, and consequently the amplitude of the induced current I_1 is low. Furthermore, when the receiver is loaded, the current I_2 is limited by the load itself and therefore it is a safe condition. When α approaches 1, the shorted LC branch tends to resonate, and the amplitude of I_1 increases. This also causes an increase of the reflected impedance seen by the active resonators, and, consequently, a reduction of the amplitude of I_2, which, in turn, tends to limit the increase of I_1. Due to this interaction between the coupled Tx coils, the maximum of I_1 and the minimum of I_2 do not occur for $\alpha = 1$, but for $\alpha = 1 + 2k_{Tx}$, which, in the present case, corresponds to about 0.88.

It can be noted that, in all cases, the current amplitude of the shorted loops is small, and practically independent from the capacitance ratio, for $\alpha \ll 0.1$ or $\alpha \gg 10$. As a consequence, a convenient choice can be to set $\alpha = 0$, which simply corresponds to replace the even capacitors ($C_{Tx,e}$) with shorts and to keep the odd ones, whose value must be $C_{Tx,o} = 1/(\omega^2 L_{Tx})$ to preserve the nominal resonance frequency. Equivalently, it is possible to set $\alpha = \infty$, which corresponds to keep only the even capacitors.

2.3.8 Experimental Validation

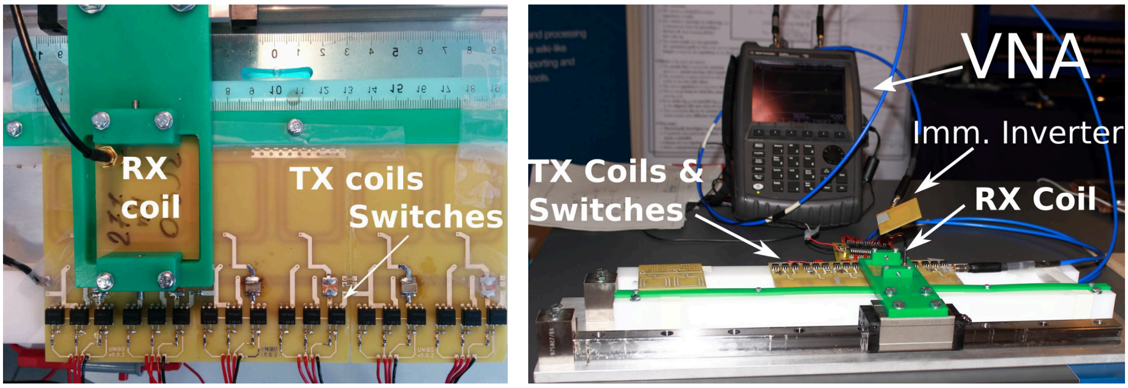

(a) (b)

Figure 2.21: System to be measured: (a), a top view of the system and (b), the complete set-up to be measured.

To validate the theoretical results, the prototype shown in fig. 2.21(a) is realized. The system consists of 6 Tx resonators and a movable receiver coil, placed on a sliding guide. The geometrical dimensions of the coils are reported in fig. 2.13 and correspond to inductances of 240 nH for the Tx coils and 277 nH for the Rx coil. The switches between the Tx coils are realized with the Vishay type VO14642AT Solid State Relays [71], which have an on-resistance of 0.1 Ω and an off-capacitance of 200 pF. These are low-cost components, chosen for the realization of the first prototype in order to demonstrate the validity of the theoretical approach. They are not intended as a final solution, where the choice must be carefully done based on the required power and selected frequency. Indeed, the quality factors of the resonators with the switches included are quite low ($Q_{TOT} < Q_{Tx} = 20$), explaining the low efficiency which will be obtained in the results. Bigger coils increase the quality factor and therefore the efficiency, but the efficiency is not the goal of this experiment.

The link has been measured from the ac Tx input port to the ac Rx output port (fig. 2.21(b)) using a Agilent FieldFox N9923A Vector Network Analyzer. 130 different positions of the receiver have been considered with 1 mm step, starting from the configuration where the Rx coil is aligned to the first Tx coil and ending with the Rx coil aligned with the fifth Tx coil. The last Tx coil is not powered during the measurements, but it is used because its switches are needed to complete the experiment.

2.3.9 Real Coupling Coefficient

A first set of measurements investigates the effects of parasitic capacitances in the switches on the coupled inductances. For this purpose, only the coupled coils with the switches are measured; therefore all compensating capacitors are short circuited and the Rx impedance inverter is removed. The impedance matrix ($\boldsymbol{Z_S}$) of the two-port network formed by two series connected Tx coils, by the Rx coil, and by the switches is measured. Fig. 2.22 reports the imaginary parts of its elements Z_{S11}, $Z_{S12}(= Z_{S21})$, and Z_{S22}, where ports 1 and 2 correspond to the Tx and Rx port, respectively. Each line corresponds to a different Rx position (130 position in total are considered, corresponding to a 13 cm displacement). These plots show an impedance with a linear frequency dependence (or that can be approximated by a straight line), thus a purely inductive behaviour, only up to about 6-6.5 MHz. At higher frequencies, the effect of the parasitic capacitances becomes evident and the resulting behaviour is different from an ideal

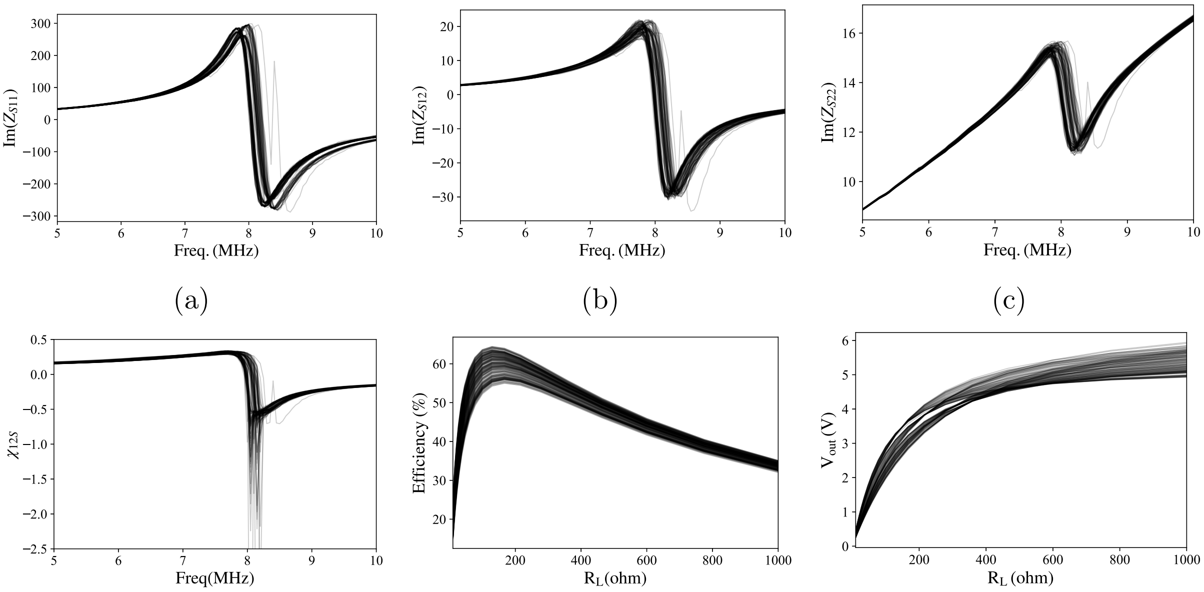

(a) (b) (c)

(d) (e) (f)

Figure 2.22: (a), (b), (c), elements of the measured impedance matrix of the coupled inductors, indexes 1 and 2 correspond to the Tx and Rx port, respectively, (d) generalized coupling coefficient (2.28), (e) efficiency (1.8) and (f) output voltage (with $V_{\text{in}} = 1\text{V}$). Each line, partly transparent to express a density, corresponds to a different Rx position: 130 positions with 1 mm step are considered, from the Rx aligned with the first Tx, to the Rx aligned with the fifth Tx. In (a)–(d) the compensating capacitors have been shorted.

inductor. In particular, a resonance at about 8 MHz can be observed.

Starting from these results, the quantity

$$\chi_{12S} = \frac{\operatorname{Im}(Z_{12})}{\sqrt{|\operatorname{Im}(Z_{11})\operatorname{Im}(Z_{22})|}}. \tag{2.28}$$

which will be referred as the generalized coupling coefficient is calculated. It can be noted that at the lower frequencies, when the system behaves as two coupled inductances, χ_{12S} corresponds to the ordinary coupling coefficient.

On the other hand, the non idealities in the actual setup, such as the C_{SW} and L_L, cause negative values of equivalent inductance near the resonance and in these conditions the usual coupling coefficient can no longer be defined.

The dependence of χ_{12S} on frequency is shown in fig. 2.22(d). These results show that the impact of the switches parasitics is not negligible at the frequency of 6.78 MHz. Nevertheless, the parasitics capacitances do not practically affect its dependence on the Rx position. The curves corresponding to different Rx positions remain well superimposed (each curve is a different position), even for frequencies close to the resonance, proving how effective and the rugged is the proposed approach under severe parasitic effects.

2.3.10 Output Voltage and ac-ac Efficiency

A second set of measurements characterizes the whole ac-ac link, for a wide range of loading resistances, in terms of output voltage (V_{out}) and efficiency (η) eq. (1.8). For this set-up the compensating capacitors ($C_{Tx,o}$) and the Rx impedance inverter are included. Fig. 2.22 shows these measurements, in the same 130 Rx positions considered before. According to the previous discussion, only the capacitors $C_{Tx,o}$ ($\alpha = 0$) are connected in series with the Tx resonators, whereas the capacitors $C_{Tx,e}$ are replaced with short circuits. The measured efficiency at 6.78 MHz is reported in fig. 2.22(e) as a function of the load resistance, which varies from 100 Ω to 1 kΩ and where each curve corresponds to a different Rx position.

Since the goal is not a state-of-the-art efficiency, but a proof of work of the proposed framework which avoids the over-currents, a peak efficiency of 65% is an acceptable result. As outlined before, the switch losses reduce significantly the quality factor of such small coils, leading to low efficiencies. Bigger coils and proper switches would easily increase the efficiency and reduce the variations, but without any added value to the goal of this work.

Furthermore, the switch off capacitances C_{SW} and line inductances L_L increase the output voltage variations compared to a result without the switches, as shown in fig. 2.23 [2]. The figure shows the same measurements as in fig. 2.22(e) and fig. 2.22(f), but using measured data from the system in fig. 2.7, which is the two coil link without the switches and therefore without the parasitics, as in fig. 2.14. It it possible to see that the variation is much smaller at 6.78 MHz and represents what to expect at lower frequencies.

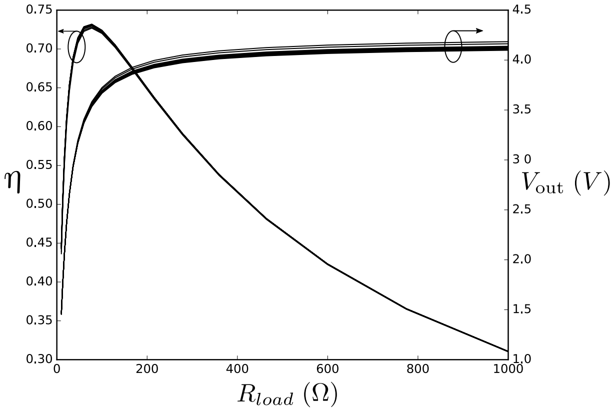

Figure 2.23: The same measurements of fig. 2.22(e) and fig. 2.22(f) but using measured data from fig. 2.7. The two coils are measured using the same method but without the switches. It it possible to see that the variation is much smaller at 6.78 MHz.

2.3.11 Characterization of the Intermediate States

A last set of measurements verify the currents in the critical loops, formed in the states A, B and C when α is varied. For this purpose, let the receiver be aligned to the subsequent Tx coil (case II in fig. 2.12), hence where the active coils need to change. The efficiency shows the over-currents in the critical closed loops: an efficiency reduction at the operating frequency indicates indirectly the presence of an over-current in the shorted resonators. Indeed, measuring the currents in the coils would affect the system, making the measure unreliable.

For each state, the measurement is repeated with 3 different configurations of the Tx capacitors, and consequently of α. For $\alpha = 1$ the capacitors $C_{Tx,o}$ and $C_{Tx,e}$ are equal, for $\alpha = 0$ only the capacitors $C_{Tx,o}$ are used, while the capacitors $C_{Tx,e}$ are replaced by short circuits, for $\alpha = \infty$ only

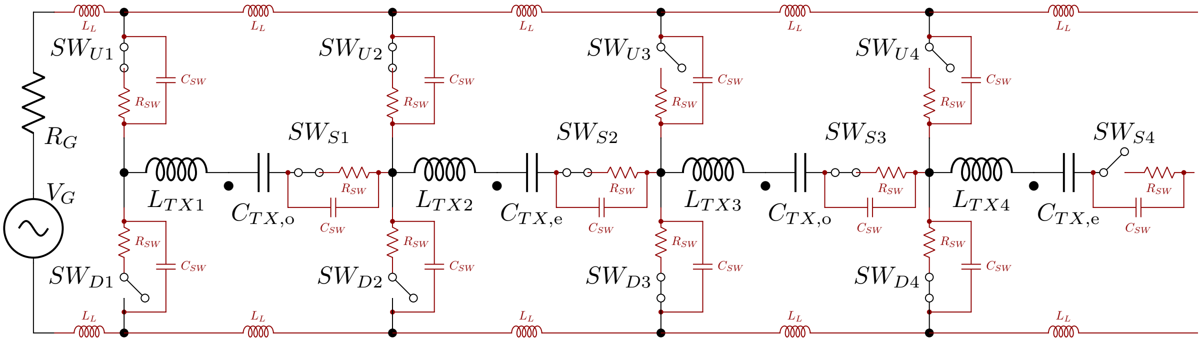

Figure 2.24: Simulated layout of State A (equivalent to fig. 2.16) with line stray inductances ($L_L = 20\,\mathrm{nH}$), switch stray capacitances ($C_{SW} = 200\,\mathrm{pF}$) and loss resistances ($R_{SW} = 100\,\mathrm{m\Omega}$). The Rx is not shown but included in the simulation as ideal. The other intermediate states are obtained by the proper selection of the switches.

the capacitors $C_{Tx,e}$ are used. The layout in fig. 2.24, which accounts for the stray capacitances of the open switches, the loss resistance of the closed switches and the inductances of the feeding lines, is numerically simulated (ac analysis [72]) and compared to measurements in fig. 2.25. As expected, for $\alpha = 1$, all the curves have a notch in correspondence of the operating frequency and therefore over-currents in the closed loops. This problem is avoided when $\alpha = 0$ or $\alpha = \infty$.

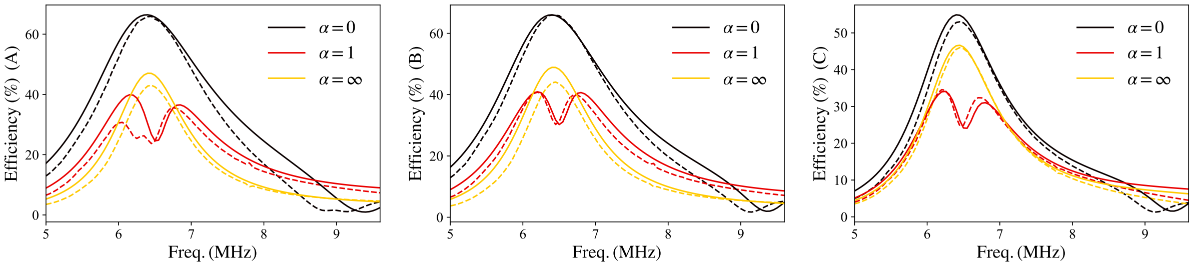

Figure 2.25: Measured (solid lines) and simulated (ac analysis, dashed lines) efficiency with the system in state A, B and C.

2.3.12 Remarks

- The “Real Series” connects two coils in series using a network of switches an a single AC source;
- It is able to maintain position independent coupling coefficient and implement the sections 2.1 and 2.2;
- The parasitic affects the performance of the system:
    - The parasitic inductance of the line affects the modularity of system by introducing a reactance, which depends on the distance from the source;
    - The parasitic capacitance of the switch introduces stray resonances;
    - The parasitic resistances of the switch reduces the quality factor of the resonators and therefore the efficiency;
    - The switches must be bidirectional;
    - The system is suitable only for low frequency links (i.e. $<$ 100 kHz).
- A method to limit over-currents when the coils are replaced is implemented and tested.

This page was intentionally left blank.

2.4 Virtual Series Connection

In this section an entire dc-to-dc system is studied and experimentally valuated [1], [5]. Again, as discussed in section 2.1, the series connection is preferable for its superior characteristics. We name this method the "Virtual Series", since the series connection behavior is obtained by forcing the same current in the coils with individual transmitters, but there is not any physical series connection. Each individual transmitter and its coil make a building block. This way, a fully modular and periodic WPT system, whose length can be arbitrarily extended depending on the specific need, is demonstrated to be possible. A further added value of the proposed architecture is that only a dc feeding line and the control logic signals are needed along the powering path, which avoids any undesired reactive parasitic effects and RF losses and high WPT operating frequencies are possible.

The block diagram is shown in fig. 2.26(a), while fig. 2.26(b) shows an illustration of the system with the dimensions. The structure is the same as used in section 2.1.

Given the high operating frequency of 6.78 MHz, the moving WPT system is tested in a quasi-static regime approximation, that is by means of snapshots of the receiver positions. Indeed, the switching period is orders of magnitude shorter than the Rx time-of-flight between two Txs. The inverters are easily synchronized by driving them with the same clock (or gate) signal.

For the demonstrative part of the system design the activation/deactivation of the switches is performed manually, but these operations can be straightforwardly implemented by a suitable control logic unit driven by the sensing of the Rx position.

2.4.1 Coupled Class-EF Inverters for Constant RF Current

To ensure the series connection of the active couple of Tx coils, while keeping the full modularity of the transmitting system, a coupled load-independent Class EF inverter, similar to the one proposed in [73], [74] is adopted as

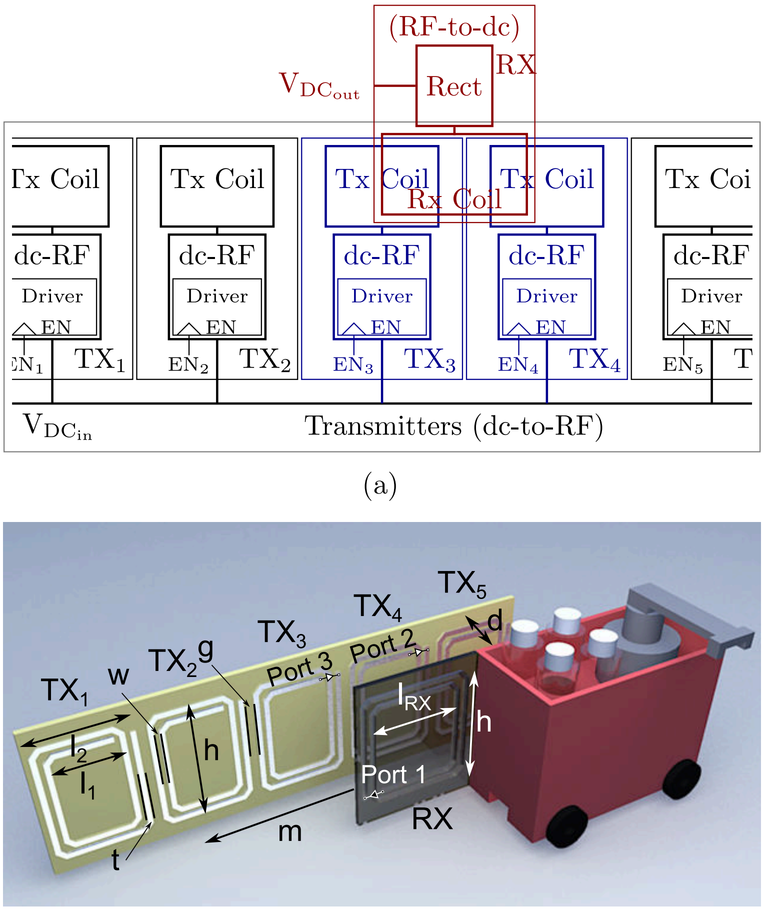

(a)

(b)

Figure 2.26: Moving WPT link powered by a linear array of planar Tx modules: a segment of five is shown, but the system can be extended to cover any linear path. Only two Tx are active at each time (blue), depending on the Rx (red) position. (a), block diagram, (b), rendered illustration of an industrial slider. For the present design at 6.78 MHz, the dimensions in cm are: $l_{RX} = 17.2$, $l_1 = 12$, $l_2 = 18$, $g = 2$, $h = 24$, $w = 1$, $t = 1$ and $d = 6$.

the power source of each Tx coil. This topology is reported in fig. 2.27, where two identical inverters driving two coupled inductors are shown: each inverter consists of a single GaN HEMT (Q_1), with a parallel reactive network designed to ensure ZVS operation. In a first step, the Rx is not yet considered, or, equivalently, $k_{RX_S} = 0$.

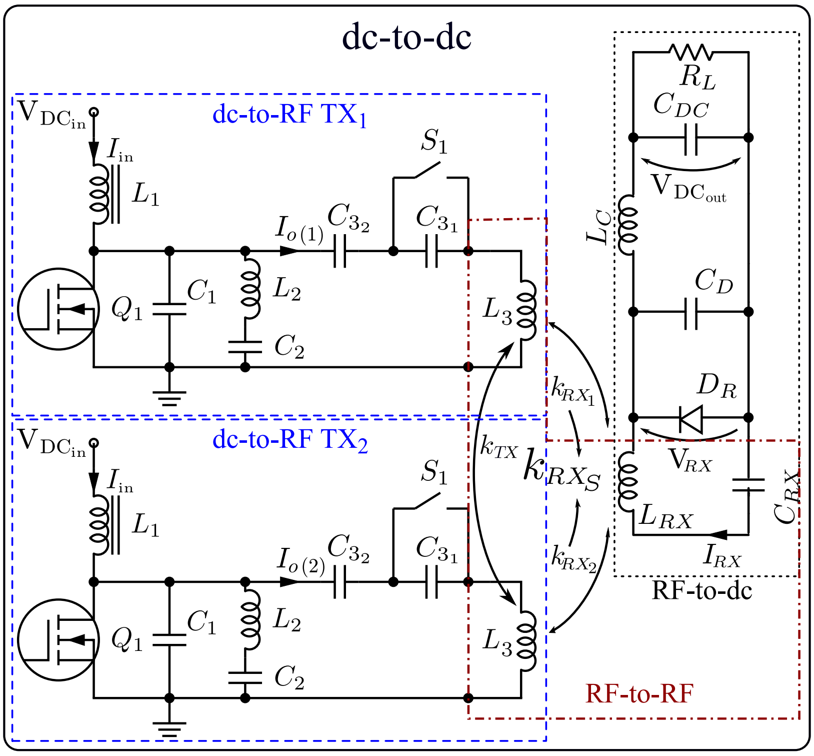

Figure 2.27: *Instantaneous* dc-to-dc moving WPT system. On the Tx side, the dc-to-RF sub-system consists of two identical current sources exciting two coupled Tx coils, L_3. To form the RF-to-RF sub-system, they are coupled to the Rx coil, L_{RX}. On the Rx side, the RF-to-dc sub-system is a class E rectifier terminated on a resistive load (variable).

The ZVS is accomplished by the parallel connection of the output capacitance C_1 with the series branch $C_2 - L_2$, which is optimized to resonate at a frequency between the inverter switching frequency, 6.78 MHz, and its second harmonic. When S_1 is open, C_{3_1} and C_{3_2} are connected in series with the Tx coil L_3, to provide the proper residual inductance. This topology maintains the ZVS operation, while achieving a constant output current, for a wide range of loads without any need of re-tuning or components replacement. The useful feature of this inverter, to be exploited in the present distributed WPT system, is to provide a constant load-independent RF output current, enabling the *virtual* series connection of the two Tx coils.

First, following the numerical procedure presented in [73], [74], the circuit parameters for the stand alone inverter are obtained: $L_1 = 88\mu H$ (RF Choke), $L_2 = 270nH$, $L_3 = 1.42\mu H$, $C_1 = 830pF$ (which includes the capacitance of Q_1), $C_2 = 718pF$, $C_3 = 480pF$, duty-cycle $D = 0.32$. In such conditions, the proper inverter resistive load can vary between 0 and $6\,\Omega$.

When two nearby Tx coils are powered, the coupling between them, k_{TX} in fig. 2.27, significantly modifies the load impedance of each inverter and the standalone topology can be used only as a starting point for the design of the two coupled inverters. Assuming the same L_3 for the two inverters, the coupled inverter design can start from the voltages and currents relationships at Tx coil ports:

$$\begin{aligned} V_{L3(1)} =& (R_{L_3} + j\omega L_3) I_{o(1)} + j\omega M_{TX} I_{o(2)} \\ V_{L3(2)} =& j\omega M_{TX} I_{o(1)} + (R_{L_3} + j\omega L_3) I_{o(2)}, \end{aligned} \tag{2.29}$$

where L_3 and R_{L_3} are the coils inductance and loss resistance, respectively, and $M_{TX} = k_{TX} L_3$. The currents $I_{o(2)}$ and $I_{o(1)}$, that ideally should be the same, if the assumption of *virtual* series connection holds, can be expressed as:

$$I_{o(1)} = Ae^{-\frac{j\phi}{2}} I_o, \quad I_{o(2)} = Be^{\frac{j\phi}{2}} I_o, \tag{2.30}$$

where $A, B \in \mathbb{R}^+$, $\phi \in \mathbb{R}$ and $I_o \in \mathbb{C}$. Using (2.29), each Tx coil impedance, $Z_{L3(n)}$ with $n \in \{1, 2\}$, in the absence of a receiver can be computed as:

$$Z_{L3(n)} = \frac{V_{L3(n)}}{I_{o(n)}} = R_{L_3} + j\omega L_3 + j\omega M_{TX} \alpha_n, \tag{2.31}$$

where $(\alpha_n) = (\alpha_1, \alpha_2) = \big(B/Ae^{j\phi}, A/Be^{-j\phi}\big)$.

The actual inductances at each inverter output, $L_{TX(n)}$, taking into account the coupling are:

$$L_{TX(n)} = \frac{\operatorname{Im}\left\{Z_{L3(n)}\right\}}{\omega} = L_3 + |\alpha_n|\, M_{TX}\cos(\phi). \tag{2.32}$$

Thus, accounting for the Tx coils coupling is mandatory, because the effective inductances, loading each coupled inverter, are different from those at the output of a standalone inverter.

Furthermore, differences in the current phases (ϕ) of each coupled Tx coil result in power transferred between the inverters ($P_{t(n)}$) that can be evaluated using the real part of (2.31):

$$\operatorname{Re}\left\{Z_{L3(n)}\right\} = R_{L_3} + \omega M_{TX}\,|\alpha_n|\sin(\phi_n), \tag{2.33}$$

$$P_{t(n)} = \omega M_{TX}\,|\alpha_n|\sin(\phi_n)\left|I_{o(n)}\right|^2, \tag{2.34}$$

where $(\phi_n) = (\arg\{\alpha_1\}, \arg\{\alpha_2\}) = (\phi, -\phi)$.

Since $P_{t(1)} = -P_{t(2)}$, the linear network alone does not introduce losses, but if the inverter is included, a phase difference can compromise its ZVS operation due to an additional voltage component induced from the current through the coupled coil that is not synchronized with the inverter operation. Indeed, the switching clocks of both inverters are synchronized (or supplied from a common source) by design and an unwanted induced voltage is inevitably affecting the ZVS. The closed switch shorts this induced voltage, causing high currents and losses. Moreover, a variation of the residual inductance, as in (2.32), even if negligible for small phase impairments, affects the ZVS due to detuning since the inverter is not tolerant to variations of its reactance termination. On the contrary, a current magnitude variation, $|\alpha_n|$, produces similar effects on the ZVS but only due to the residual inductance, because, without any phase impairment, the power transferred between the Tx coils is always zero ($\sin(\phi_n) = 0$). Besides an efficiency degradation, this also means that Q_1 can experience overheating.

The quality factor of the virtual inductor $L_{TX(n)}$ is:

$$Q_{L_{TX(n)}} = \frac{\omega\left(L_3 + |\alpha_n|\, M_{TX}\cos(\phi)\right)}{R_{L_3} + \omega M_{TX}\,|\alpha_n|\sin(\phi_n)}, \tag{2.35}$$

or equivalently, using the relation $M_{TX} = k_{TX} L_3$:

$$Q_{L_{TX(n)}} = \frac{1 + |\alpha_n|\, k_{TX} \cos(\phi)}{Q_{L_3}^{-1} + |\alpha_n|\, k_{TX} \sin(\phi_n)}, \tag{2.36}$$

where $Q_{L_3} = (\omega L_3)/R_{L_3}$ is the quality factor of L_3.

Since a key feature is to achieve currents with equal amplitudes, it is possible to approximate $|\alpha_n| \simeq 1$. Therefore:

$$L_{TX(n)} \simeq L_3 + M_{TX} \cos(\phi) \simeq L_3 + M_{TX}, \tag{2.37}$$

where $\cos(\phi) \simeq 1$ for small angles ϕ. Equivalently:

$$L_{TX(n)} \simeq L_3 \left(1 + k_{TX}\right). \tag{2.38}$$

The resistive part becomes:

$$\mathrm{Re}\left\{Z_{L_{3(n)}}\right\} \simeq R_{L_3} + \omega M_{TX} \phi_n, \tag{2.39}$$

with $\sin(\phi_n) \simeq \phi_n$ for small angles ϕ_n.

For this setup, the Tx coils are modeled as: $k_{TX} = -0.0595$, $L_3 = 1.42\,\mu$H, $R_{L_3} = 0.15\,\Omega$, $\omega = 2\pi 6.78 \times 10^6$rad/s. Since the coupling k_{TX} is negative, $L_{TX(n)} = 1.34\,\mu$H, smaller than L_3.

The next step is to guarantee the proper residual inductance [49] to each coupled inverter. Let $L_{3,r}$ be the desired one for the standalone inverter, which is the result of the $C_3 - L_3$ series. When the *virtual* $L_{TX(n)}$ loads the inverter in place of L_3, the proper compensating capacitor $C'_{3(n)}$ which provides $L_{3,r}$ is computed as:

$$L_{3,r} = L_3 - \frac{1}{C_3 \omega^2},\ L_{TX,r(n)} = L_{TX} - \frac{1}{C'_{3(n)} \omega^2}. \tag{2.40}$$

Forcing $L_{3,r} = L_{TX,r(n)}$ and using (2.38):

$$C'_{3(n)} = \frac{C_3}{1 + \left(\frac{\omega}{\omega_r}\right)^2 k_{TX}}, \text{ where } \omega_r = \frac{1}{\sqrt{C_3 L_3}}, \tag{2.41}$$

where C_3 is the optimal value for the standalone inverter [73] and $C^{'}_{3(n)}$ is the corresponding one for the coupled case.

The last issue to be discussed is to limit the currents induced in the non-active Tx coils due to the currents flowing in the activated coils. From circuit simulation it is shown that without any countermeasure, these currents are of the same order of magnitude of the desired ones, resulting in additional losses and detuning of the active inverters. To minimize this contribution, the capacitor $C^{'}_{3(n)}$ is split into two C_{3_2}, C_{3_1}, with $C_{3_2} > C_{3_1}$, and a switch (S_1 in Fig. 2.27) is connected in parallel to the smaller capacitor: if the inverter is off, the switch is closed, if the inverter is on, the switch is open. In this way, if the inverter is off, its load is strongly detuned and the resulting output current is minimized. Furthermore, this solution avoids to short the $V_{DC_{in}}$ supply, which would happen by shorting a single $C^{'}_{3(n)}$. To determine C_{3_1} and C_{3_2} values, their series connection is chosen to be equal to $C^{'}_{3(n)}$. Let $C_{3_2} = \beta C_{3_1}$, it follows that:

$$C_{3_1} = C^{'}_{3(n)} \left(\frac{\beta + 1}{\beta} \right), \quad C_{3_2} = C^{'}_{3(n)} \left(\beta + 1 \right). \tag{2.42}$$

A snubber, formed by R_S and L_S, is also connected in series to S_1 to mitigate the current peaks through the charged C_{3_1} when the switch is closed.

The designed values of these components are: C_{3_1} =530 pF, C_{3_2} =4.70 nF (hence $C^{'}_{3(n)} = 480$ pF and $\beta \sim 9$), $R_S = 10\,\text{k}\Omega$, $L_S = 250$ nH. An inactive Tx module is reported in Fig. 2.28.

Fig. 2.27 shows the circuit schematic of the end-to-end (dc-to-dc) link with two active Tx modules and the Rx coil loaded by a Class E rectifier similar to the one designed and experimentally verified in [75], [76]. The modified design Class E rectifier is detailed in the next subsection.

In the next step, to evaluate the dc-to-RF sub-system in different positions, the receiver is introduced as a series resonant RLC load (with $k_{RX_S} \neq 0$), which allows to check if the coupled inverters sustain the same current through the Tx coils. It also allows to verify that the output voltage on the resistive load is independent from both the Rx position and the load. The values of the components at the Rx side are: L_{RX} =1.7 μH,

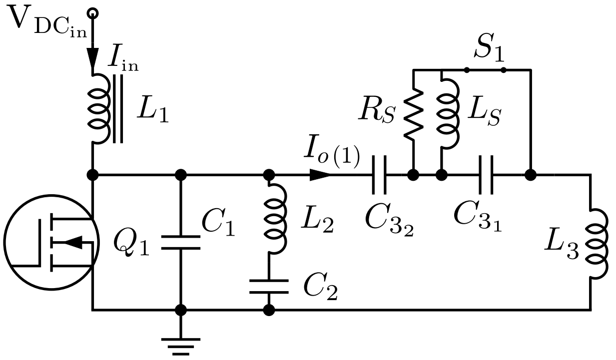

Figure 2.28: Modified Class EF inverter in the off state: S_1 is closed, the inverter is detuned and the current $I_{o(1)}$ is negligible.

C_{RX} =324 pF. k_{RX_1} and k_{RX_2} are derived by full-wave EM simulation of the coupled-coil 3-port RF link. From the measurements, the coupling coefficients resulted to be 10% lower than predicted, see fig. 2.8, which in turn results in an effective k_{RX_S} of about 0.16.

First, the circuit of fig. 2.27 is simulated in time-domain, with the rectifier replaced by a variable resistive load, for several receiver positions and loads: for each of the twenty Rx positions previously considered. The performance with respect to thirty different loads are evaluated, from 10 Ω to 1 kΩ. fig. 2.29(a) shows the currents through each Tx coil, while fig. 2.29(b) reports the voltage across the resistive Rx load. The input dc voltage ($V_{DC_{in}}$) is 70 V. All these plots are practically superimposed, proving that the coupled inverters are able to work as load-independent current sources, with the *virtual* series connection between the two Tx active coils confirmed.

2.4.2 The Rectifier and the Complete dc-to-dc Link

To ensure the same performances discussed above, the rectifier is required to present a constant output voltage and a purely resistive input impedance, over the range of RF input power of interest, for any possible Rx position and loading conditions. This is a challenging task and, to our knowledge, it is still

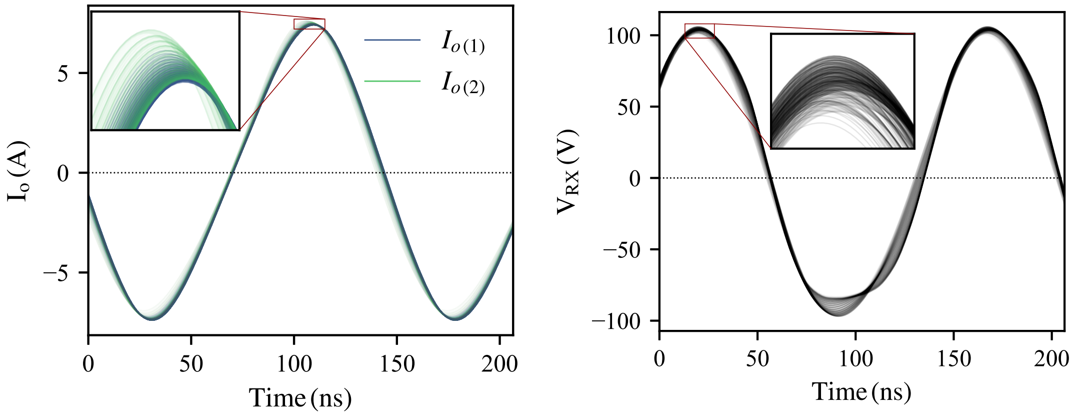

(a) (b)

Figure 2.29: Load and position independent waveforms of the currents exciting the two coupled Tx coils, Fig. (a), and voltages on the load (purely resistive and which replaces the rectifier in section 2.4.1), Fig. (b), for a $V_{DC_{in}}$ of 70 V. Results are from a set of 600 nonlinear/EM co-simulations spanning a 10 cm Rx displacement (20 different Rx positions) and 30 loads from 10 to 1 kΩ. The curves are almost indistinguishable, insets highlight the differences.

unresolved. Indeed, the design of a standard Class E rectifier [49], [75] cannot be adopted for the present case, because its input reactance is dependent on the duty-cycle, which is a function of the dc load. Furthermore, in a moving system, such reactance varies with the Rx position and, once reflected to the Tx side, would degrade its performances, which are based on the (resistive-)load-independent coupled inverters. For a given excitation, the nonlinear reflected impedance $Z'_{RX(n)}$, which effectively loads the inverter, can be written as:

$$Z'_{RX(n)} = \frac{\omega^2 M^2_{RX(n)}}{Z_{RX}} \tag{2.43}$$

where $M_{RX(n)} = k_{RX(n)}\sqrt{L_3 L_{RX}}$ is the mutual inductance between an active Tx coil and the Rx one and Z_{RX} is the rectifier input impedance (V_{RX}/I_{RX})

at the fundamental harmonic. Since $M_{RX(n)}$ strongly depends on the Rx position, a constant imaginary part of Z_{RX} still produces a significant variation of $Z'_{RX(n)}$ while the Rx is moving. Thus, the rectifier has to provide a quasi zero imaginary part of $Z'_{RX(n)}$ for any dc-load of interest.

The Class-E Resonant Rectifier [77] with a quasi-resistive-input is used as a starting point. Although this solution is able to reduce the reactive part of Z_{RX}, by a proper choice of C_D and by allowing for a ripple of the output current by reducing L_C, it results in a output voltage strongly dependent on the dc load, which is not an acceptable solution for the system under consideration. For this reason an harmonic balance (HB)-based optimization of the whole dc-to-dc system is carried out, spanning all the possible Rx loads and positions. The RF choke, L_C, is reintroduced. The capacitors C_{RX} and C_D (Fig. 2.27) are included among the design variables. Two main goals are pursued: the maximization of the dc-to-dc efficiency and the minimization of the dc output voltage variations, which imply minimizing the imaginary part of $Z'_{RX(n)}$. A total number of system configurations equal to 600 is considered, covering 20 Rx positions and 30 loads. The nonlinear regime is described using 16 harmonics. $V_{DC_{in}}$ is 70 V, which is the best trade-off between maximum output dc power, efficiency, and safety for the experimental verification. The losses are accounted for by resistances in series with the respective inductances and are computed as: R_{L_1} =2 Ω, R_{L_2} =0.06 Ω, R_{L_3} =0.15 Ω, $R_{L_{RX}}$ =0.2 Ω, R_{L_C} =2 Ω. Q_1 is modeled as a switch with a series resistance of 50 mΩ, while the remaining components are ideal. The other circuit elements are: L_{RX} =1.7 μH, L_C =88 μH, C_{DC} =20 μF. The diode is the Schottky SiC Wolfspeed/CREE C3D1P7060Q, chosen to sustain high current/voltage capability and has a low capacitance. To comply with high current peaks, two diodes are connected in parallel thanks to the positive temperature coefficient of SiC diodes, which results in equal sharing of currents, and are included in the simulation using their SPICE model. The optimized capacitors are: C_{RX} =498 pF and C_D =33 pF.

The predicted dc output power is 100 W on a 38 Ω load with a dc-dc efficiency of 80%, calculated as eq. (1.10).

The voltage variation is under 5%, for any load value over 30 Ω. After the nonlinear optimization, the imaginary part of the impedance $Z'_{RX(n)}$, monitored for all the system configurations discussed above (Rx positions and loads) is always lower than $0.2j$, corresponding to a L_3 variation under 5 nH, or 0.3%. This ensures the proper switching operation (ZVS) of the inverters.

2.4.3 Experimental Set-Up and Measurements

The measurement set-up, see fig. 2.30, is composed of four identical Tx modules (one is shown in fig. 2.31). Details of the inverter and the rectifier are shown in Fig. 2.32 and in Fig. 2.33, respectively. Q_1 is a GaN System GS66504B Enhancement HEMT GaN FET. The powering path, as extended as necessary, is obtained by placing side-by-side other transmitter modules, like "Lego" tiles. Therefore the system only requires a single dc-feed line along the whole path while the RF signal is generated on board at the active modules locations only, which is a strong advantage in terms of power consumption.

On top of the transmitter path, the receiver unit is able to continuously slide through the Tx path. It is also possible to transfer power to multiple receivers using different pairs of inverters, by ensuring a pair of inactive coils in between two pairs of the active ones, to avoid unwanted multiple couplings.

In the prototyped Class E rectifier, the Wolfspeed/CREE C3D02060F diode is adopted in place of the two C3D1P7060Q, due to the inaccuracy of the SPICE model of the latter in describing the diode capacitance, which causes unwanted non-zero reactance at the rectifier input. This allows a lower capacitance, of the order of 20 pF, at the expense of a 1% reduction of the peak efficiency. However, this is found to be necessary to achieve a proper working system. Both devices are based on Wide Band Gap Semiconductors, which allow higher efficiencies, power densities, breakdown voltages, and low stray capacitances.

Table 2.1 reports all the component values of the inverters and of the receiver. Both the predicted and the actual ones used in the prototype are reported. For the Tx side, both the standalone and the coupled inverter configurations are reported. For the Rx side, two configurations are con-

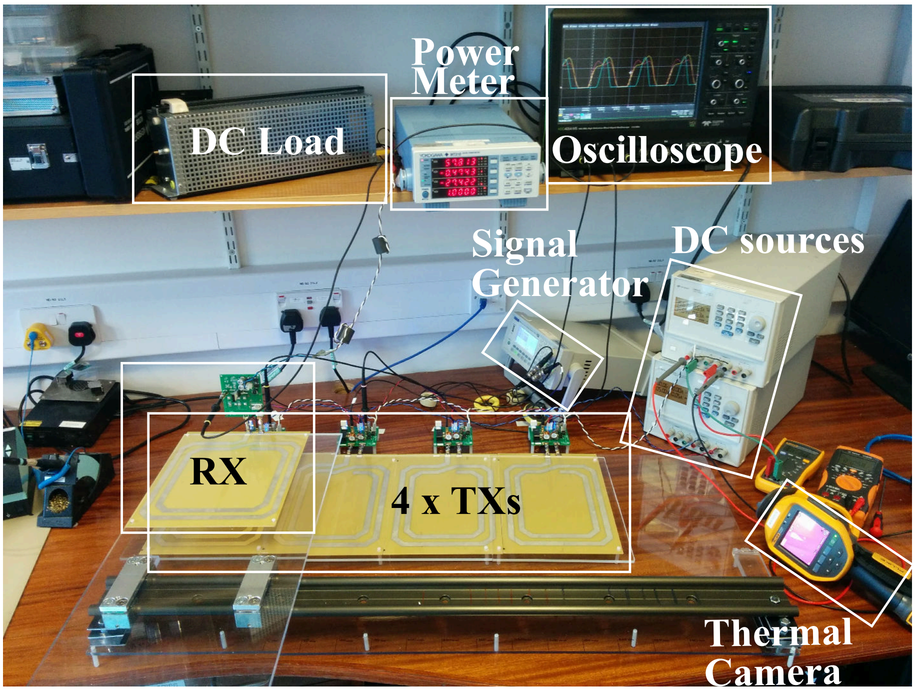

Figure 2.30: dc-to-dc link set-up: four Tx coils, each one driven by its own inverter, with a Rx subsystem sliding over them at a vertical separation of 6 cm. The GaN FET is driven by an ISL5511IRZ high speed mosfet IC driver with a gate voltage of 5 V. The variable load is connected to the dc output and spans from 30 Ω to 120 Ω (higher resistances are obtained by a series connection of 100 Ω power resistors). The output dc power is measured by the Yokogawa WT310 power meter and the RF voltage waveforms are monitored using the LeCroy HDO4054 oscilloscope. The thermal camera is used for temperature monitoring.

sidered: i) the purely resistive variable load, in series with the $C_{RX} - L_{RX}$ resonator; ii) the rectifier. Some component values of the prototype are different from the predicted ones due to the fine tuning needed for the experimental setup. The optimum operating frequency of the prototype was found to be 6.81 MHz to achieve ZVS.

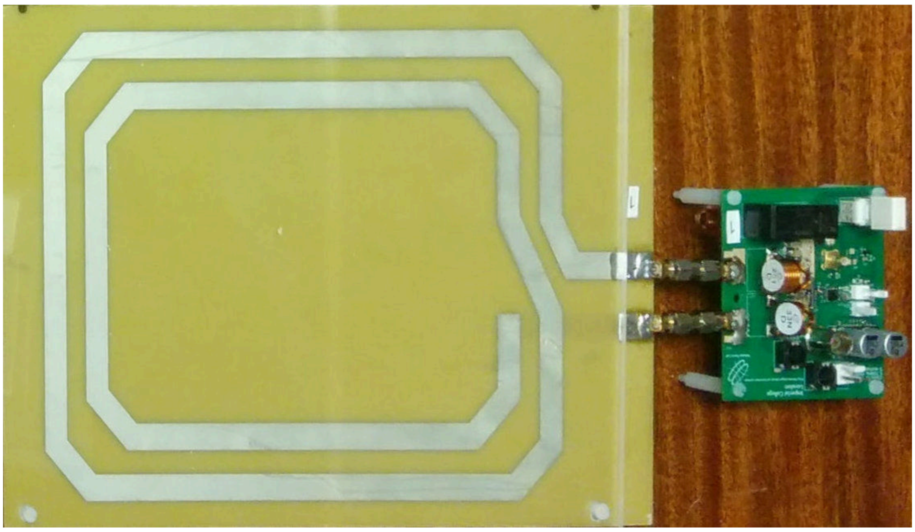

Figure 2.31: Photo of a single TX module.

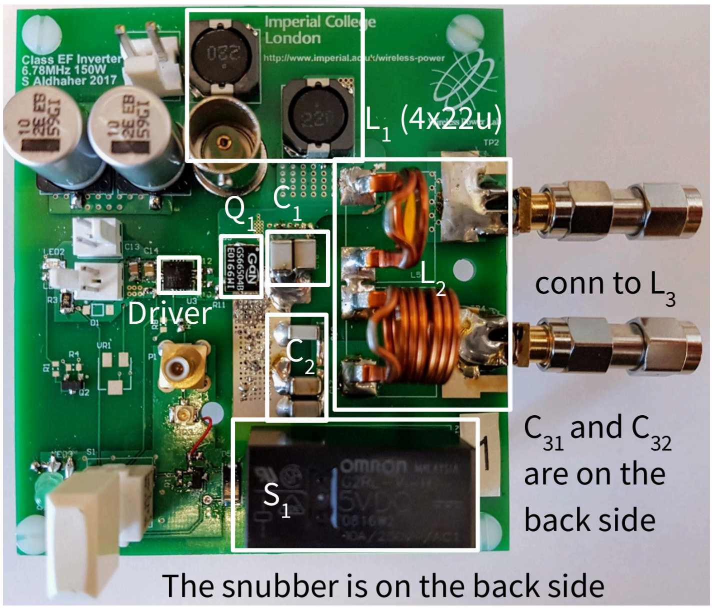

Figure 2.32: Photo of the Class-EF inverter.

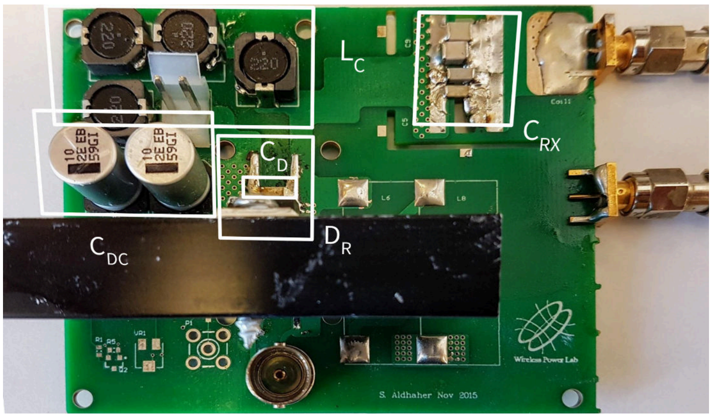

Figure 2.33: Photo of the Class-E rectifier.

2.4.4 Entire WPT System Characterization with the Moving Rx

The receiver is moved over the entire Tx path and the dc output voltage is measured. Figure 2.34(a) shows the simulated and measured dc output voltage and fig. 2.34(b) the overall dc-to-dc efficiency. Simulation results belong to two different models of the RF-to-RF link: the first one uses the link Z-matrix computed by full-wave EM simulation; the second one uses a coupled coils model with the coupling coefficient reduced by 10% ($k^{'}_{RX(n)} = 0.9k_{RX(n)}$), which better matched the VNA measurements of the RF link, corresponding to a slightly longer Tx-Rx effective distance. The model with $k^{'}_{RX(n)}$ is in very good agreement with the measurements. The key aspects of these experimental plots is the excellent flatness of $V_{DC_{out}}$ that the present design is able to ensure, regardless of the receiver position and load. Figure 2.34(b) shows the efficiency compared again with the two simulation models. The maximum efficiency is 80% with an output power of 100 W. As previously stated, the goal of a 100 W is chosen for validating the design of the entire dc-to-dc system, while ensuring safe measurement conditions. A 70 V dc bias is needed to reach this output dc power. Choosing a higher dc bias increases the maximum efficiency and allows a higher output dc power and voltage, but with no added value to the

Table 2.1: Tx and Rx component values.

Inverter:	**Standalone [73]**	**Coupled**	
	Simulated	Simulated	Prototype
L_1	88 µH	88 µH	88 µH
L_2	270 nH	270 nH	283 nH
L_3	1.42 µH	1.42 µH	1.42 µH
C_1	830 pF	830 pF	660 pF
C_2	718 pF	718 pF	696 pF
C_3	480 pF	—	—
C_{3_1}	—	530 pF	526 pF
C_{3_2}	—	4.7 nF	4.7 nF
Q_1	50 mΩ (R_{on})	50 mΩ (R_{on})	GS66504B
R_S	—	10 kΩ	10 kΩ
L_S	—	250 nH	250 nH
k_{TX}	—	-0.0595	-0.0595
D	0.32	0.32	0.32
f	6.78 MHz	6.78 MHz	6.81 MHz
Rx load:	**Resistive**	**Rectifier**	
	Simulated	Simulated	Prototype
L_C	88 µH	88 µH	88 µH
L_{RX}	1.7 µH	1.7 µH	1.7 µH
C_D	—	33 pF	30 pF
C_{DC}	—	20 µF	20 µF
C_{RX}	324 pF	498 pF	498 pF
D_R	—	2 x C3D1P7060Q	C3D02060F

design proposed in this work. The chosen GaN device allows the inverter to operate with voltages as high as 100 V, predicted by simulation to enable an output dc power of 160 W into a 35 Ω load, with a dc-to-dc efficiency of about 84%. The maximum dc voltage is actually not limited by the GaN and SiC devices, but by the overheating of L_2, which reaches 80 °C with a 70 V input.

Figure 2.35 shows the measured dc output voltage versus an Rx path, which exceeds the design path and highlights that the flatness property is ensured only if the *virtual* series connection is guaranteed, while it is lost as

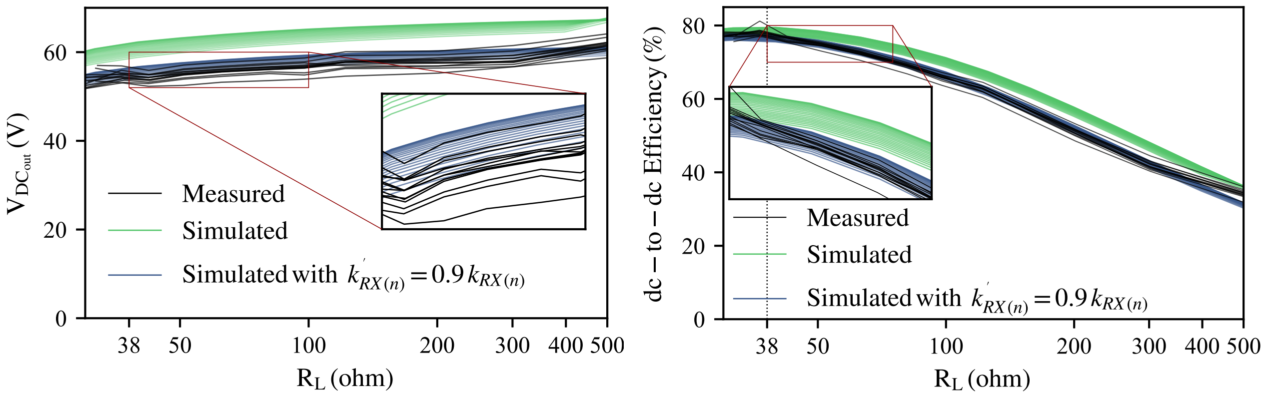

(a) (b)

Figure 2.34: (a) measured and simulated output dc voltage and (b) system efficiency versus dc load, for twenty positions over a 60 cm Rx displacement. For 0 cm, the Rx and TX_1 axes are aligned; for 60 cm, the Rx and TX_4 axes are aligned. The curves are almost indistinguishable (for a given load no significant variations of the system performance are experimentally verified). Insets are used to highlight the differences. The two families of simulated plots are obtained using $k_{RX(n)}$, as computed in (2.11), and with $k'_{RX(n)} = 0.9k_{RX(n)}$, which better matches the measured coupling.

soon as the the receiver moves out of the design path. Figure 2.36 reports the measured voltage across D_R: the peak value of 300 V is well below the 600 V breakdown voltage and the duty-cycle is only slightly modified (less than 6%) by load changes, ensuring an almost constant dc component of the voltage across the diode, without any output current ripple.

A loss budget can finally be estimated by considering constant (for the system in idle mode) and variable (with the output power) losses. With regard to the first contribution, the measured idle power loss for both coupled inverters is 15 W. The simulated current flow in L_2, which is the components experiencing the highest temperature, is in the order of 10 A, resulting in a 3 W power loss. The power loss due to a simulated current of 7 A through L_3 is 3.5 W.

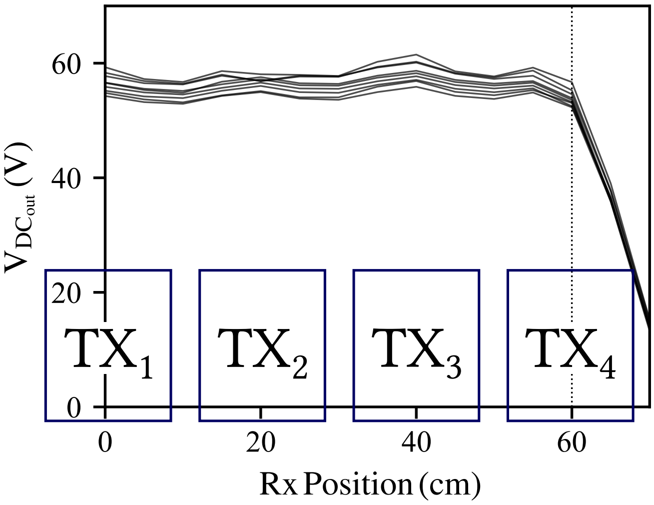

Figure 2.35: $V_{DC_{out}}$ versus an extended Rx position, with the load as a parameter. Each line is a different dc load. For 0 cm, the Rx and TX_1 axes are aligned, and the couple TX_1 TX_2 is active; for 60 cm, the Rx and TX_4 axes are aligned and a further fifth coils should be activated (not available in the present prototype). Starting from this position the output voltage immediately drops.

The losses variable with the output power are mainly affected by the RF chokes and are also position-dependent: when the Rx is aligned with one Tx and the output dc power is 100 W, the loss is 10 W with a 7 W contribution being from RF chokes. Hence for an output dc power of 100 W, 20 W is the total power lost in the inductors and 5 W in the other components, which confirms the advantages of using ZVS resonant converter based on Wide Band Gap semiconductors.

2.4.5 Coupled Inverters Characterization

Figure 2.37 shows the measured dc-to-dc efficiency for a wide range of dc output powers. The lines are all well superimposed, validating experimen-

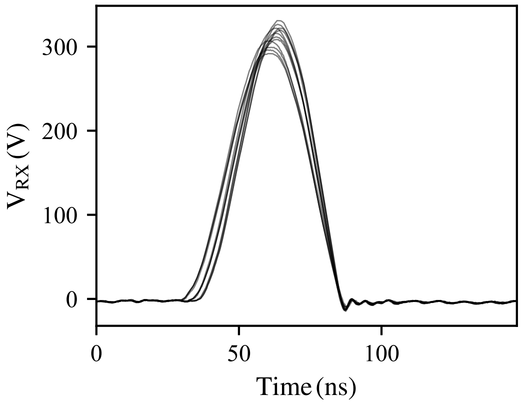

Figure 2.36: Voltage on D_R (V_{RX}) measured for all the combination of four Rx positions (0, 5, 10, 15 cm) and three loads (60, 80, 120 Ω).

tally the coupled inverter operation of providing the same dc output power and the same system efficiency regardless of the Rx position. From these plots it can be observed that the dc-to-dc system efficiency exceeds 60% as the output dc power is over 25 W.

A direct measurement of the Tx output currents $I_{o(n)}$ is not feasible since it strongly affects its operation, but it is possible to deduce that the currents through the active Tx coils are equal from fig. 2.37 and from thermal measurements: if there was a change in the phases of the Tx coil currents due to a different Rx position, this would cause a significant increase of the inverter losses due to the degradation of the ZVS operation and would overheat Q_1. Indeed, a phase shift of the current $I_{o(n)}$ directly affects the inverter ability to operate in soft-switching conditions, while the ZVS is guaranteed by the plots reported in fig. 2.38, where the measured drain-source voltage waveforms of the two active inverters are reported, for various combinations of dc loads and Rx positions. The soft-switching operation is ensured for both inverters and therefore the desired phase coherence of the currents $I_{o(n)}$ is expected. Furthermore, tests carried out with the thermal camera confirm that no overheating is experienced by the GaN devices. A further confirmation comes from the measured constant

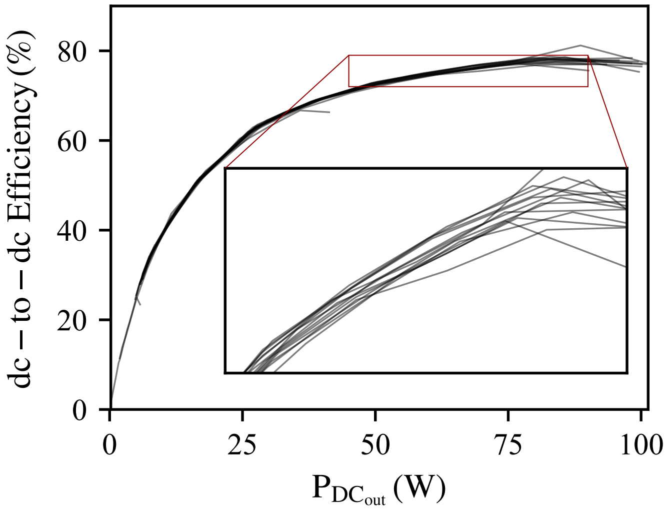

Figure 2.37: Dc-dc efficiency as function of $P_{DC_{out}}$. For each position (a different line) the load is swept ($30 < R_L < 500$) to obtain the resulting output power range with a 70 V $V_{DC_{in}}$: this confirms that the position is not detuning the inverter.

$V_{DC_{out}}$ of fig. 2.35, which proves the *virtual* series connection between the coupled inverters. Since the output voltage is related to the absolute value of V_{RX}:

$$V_{RX} = M_{TX_1} I_{o(1)} + M_{TX_2} I_{o(2)}, \tag{2.44}$$

a phase difference would add two out-of-phase contributions and therefore a lower V_{RX}, also dependent on the Rx position.

2.4.6 Passive Position Sensing via Inverter Currents

There are many possible ways to find the position of the receiver, from an optical sensor to a passive indirect extrapolation from the inverter currents.

The easiest is the optical sensor on the receiver, which can then communicate the position to a control system at the transmitter side via a data link, but it requires the power system to *trust* completely the data link.

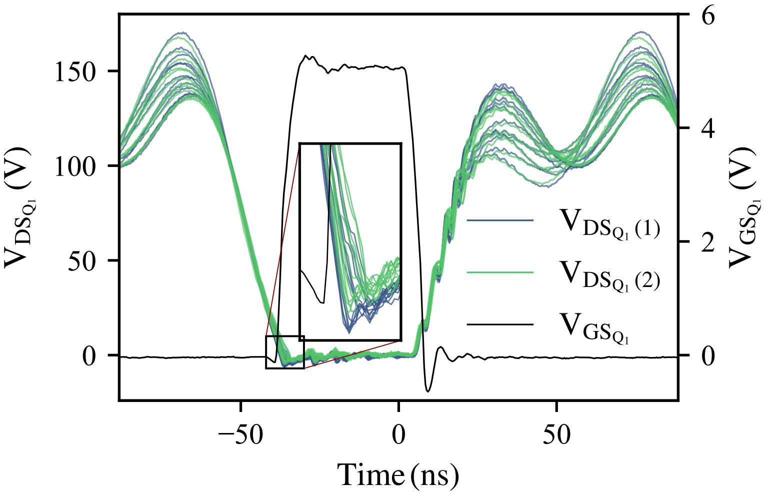

Figure 2.38: GaN E-HEMT drain-source voltage of the inverters ($V_{DS_{Q1(n)}}$, with $n = 1, 2$) measured for four Rx positions (0, 5, 10, 15 cm) and three different loads (60, 80, 120 Ω). The measured gate-source driving voltage waveform ($V_{GS_{Q1}}$ is superimposed in the same plot: the load- and position-independent soft switching operation of the inverter is experimentally verified.

Indeed, any loss of data could mean a wrong inverter is turned on or off, with the risk of damaging the power part. The possible delay of the data link can be an another source of issues, because it would mean that the inverter are activated with wrong timings. Furthermore, an optical sensor is an additional system to service, which can be degraded by dust or dirt.

An integrated sensing is more rugged and more scientifically interesting, as to retrieve the position indirectly by a current readout on the transmitters. How the currents are shared between the two inverters depends on the position. In a system with ideal components and without losses, the sum of the input powers is equal to the output power, which is *constant.* The transmitters are powered with the same input voltage and therefore the same applies to currents: *the sum of the input currents is constant.* When the receiver is aligned with the first transmitter, the entire share of current is given to the first, vice versa when it is aligned with the second one. Anyway, a change of the receiver load would also provide a different current and therefore it cannot distinguish between a position variation or a load variations. But, when the input currents (or equivalently powers) of each inverter are normalized to their sum, this dimensionless number represents the share of the total current to each inverter and is uniquely related to the position and independent of the load.

Unfortunately, when losses are included and the load changes, the normalized input currents are again unable to uniquely find the position, discriminating a load or a position variation. Indeed, the losses introduce an offset to each inverter with a weak dependence on the load and position of the receiver. For example, these are not zero when the receiver is aligned with the other transmitter and therefore the share of input currents, which would show a load dependent offset.

The need is to estimate the losses in the inverters and, because of equal input voltage, can be represented with currents: we call them *loss currents*. When the loss currents are removed from the input ones, the remaining part is entirely flowing to the receiver, similarly to the case without losses. The efficiency of the receiver is not taken into account as it does not depend on the position and therefore is simply a slightly higher load (to compensate the losses) for the transmitters.

With other words, the input current is made of two parts: a current responsible of the power transferred to the load, which is zero when unloaded, and a current responsible of the losses, which is the idle current when unloaded. Note that not all the inverters can operate without a load but they necessitate a specific load. Hence, in these cases, the losses must be measured indirectly and the idle current is only for an hypothetical idle condition. It will be clearer in the following.

It makes sense now to hypothesize that the loss current in the transmitter, is related to the current in the coil:

- The resistive losses in the coil and the switch depend, with a quadratic relation, on the value of their currents;
- The switching losses are related to the voltage on the switch parallel capacitor when it is turned on. This voltage depends on the output

current discharging this capacitor.

- The body diode of the switch avoids negative voltages on the switch and, in this condition, the losses are therefore related to currents conducting in the diode and not to the capacitor. Anyway, it is better to use a SiC Schottky diode in parallel to the body diode, as it decreases the losses.

Therefore, the losses are mainly due to the currents circulating in the resonant circuits and how well the ZVS is performed. Notice that the Thevenin equivalent is not able to represent the nonlinear inverter. Indeed, the losses in resonant inverters are usually minimized through ZVS only for a specific load and a load change can likely increase them, even with an open circuit load, with the risk of damaging the inverter. The Load Independent Inverter maintains *ideally* the same current in the resonators and ZVS independently of the load. The idle losses are *approximately* the same throughout the entire eligible load range, which result is an efficiency increase until the peak at the optimum load. For this inverter which act as a current source, idle means that the load resonator of the inverter is shorted, which is the case when the receiver is removed. This is a safe condition, for this inverter, and therefore the idle current can be directly measured. With non ideal components, the currents in the coils slightly changes with the load, with the open circuit having the maximum current. Therefore we expect the losses to *slightly change* and to be reduced with higher powers. It is counter intuitive, but is confirmed by simulations and measurements.

2.4.6.1 Mathematical Representation of the Input Current

To represent the input current, it must be noted that the losses in the inverter, due to parasitics in a non linear circuit, are probably non representable in a closed form analytical expression. A possible alternative is to find a polynomial regression of the input current $I_{dc_{(k)}}$ to the peak coil current $i_{ac_{(k)}}$ (if the current is sinusoidal, which is the case with high resonator quality factors, this is the magnitude):

$$I_{dc_{(k)}} = I_{dc_{(J,k)}l} + \sum_{j=1}^{J} \alpha_{j(k)} i^{j}_{ac_{(k)}}, \tag{2.45}$$

where k indicates the number of the active inverter and $I_{dc_{(J,k)}l}$ is the ideal current (when $J \to \infty$) which represents the power transferred to the receiver: when there are no losses in the inverter, the input current is $I_{dc_{(J,k)}l}$ and can be seen as the zeroth term of the sum. The sum represents the loss current $I_{dc_{(J,k)}\text{loss}}$: it can not be independent of the current in the coil.

Now, the normalized load current can therefore be expressed in terms of $I_{dc_{(J,k)}l}$, similarly to the case without losses:

$$I_{Ndc_{(J,k)}l} = \frac{I_{dc_{(k)}} - \sum_{j=1}^{J} \alpha_{j_{(k)}} i^{j}_{ac_{(k)}}}{I_{dc_{(1)}} - \sum_{j=1}^{J} \alpha_{j_{(k)}} i^{j}_{ac_{(1)}} + I_{dc_{(2)}} - \sum_{j=1}^{J} \alpha_{j_{(k)}} i^{j}_{ac_{(2)}}} \tag{2.46}$$

with $k = 1, 2$.

The coefficients in eq. (2.46) are complex to derive and a tentative can be to reduce the order of the regression for the current and perform a linear regression ($J = 1$):

$$I_{Ndc_{(1,k)}l} = \frac{I_{dc_{(k)}} - \alpha_{(1,k)} i_{ac_{(k)}}}{I_{dc_{(1)}} + I_{dc_{(2)}} - \alpha_{(1,1)} i_{ac_{(1)}} - \alpha_{(1,2)} i_{ac_{(2)}}} \tag{2.47}$$

A value of 1 means that all the “loss-less” current is in that inverter.

2.4.6.2 Position Sensing Measurement Setup

Since the availability of the real system, the following methods are validated using both measured and simulated data. Originally, the concept was developed firstly with simulated data and then confirmed by measurements, but here they are instead presented side by side to ease the reader.

The simulation of the entire system is performed in ADS with the Harmonic Balance solver with order 16 (15 harmonics plus dc) [72] and shown in fig. 2.39. Each inverter is simulated with equal components and therefore the same coefficients are expected for each inverter. The link is modeled using the position dependent couplings obtained by full-wave simulations of the structure in section 2.1 and extended by mirroring them to the other coil, since ideally the structure is perfectly symmetric.

The real inverters are obviously more complicated than the simulated model. First, there are tolerances and therefore the coefficients can be different for each inverter in each couple of active coils. Indeed, each inverter can show different losses if it is working with the preceding or the following one, because a slight detuning of one inverter due to tolerances can affect tuning of the other, hence the losses. Second, the real parasitics are more complex and non linear than fig. 2.39, which only considers the linearized drain source capacitor that has been incorporated in C_1 and the resistive channel.

Tx1, Tx3 and Tx4 suffered a damage in a previous measurement due to a faulty connector to the driver, which shorted the GaNs that overheated. Tx1 and Tx4 were not anymore usable, while the GaN switch in Tx3 was slightly defective: it was suffering a breakdown when the input voltage was over 45 V and was more lossy (suffering higher temperatures). Only Tx2 and Tx3 were powered and the defective switch made the inverter Tx3 less load independent, with a more variable ac current. Of course replacing the GaN would have solved the issue, but it was unavailable at the moment and this was an opportunity to test the method with high asymmetries in the inverters. The input voltage was limited to 40 V, instead of 70 V as previously, to avoid the issues with Tx3. A lower voltage is expected to provide different coefficients, which can be dependent of the input voltage.

The details of the setup (fig. 2.40) and the measurement procedure are in the following of this section.

To measure the current, a broadband current transformer `PEARSON™ CURRENT MONITOR MODEL 6585` is introduced on one coil terminal. The connection was modified and a short piece of cable was included that connected the coil and passed through the current monitor. This additional wire slightly altered the inductance of the transmitting coil and therefore the compensating capacitance had to be reduced to recover the same frequency. The additional inductance to L_3 is about 70 nH more ($L_3 = 1.49\,\mu\text{H}$). Replacing C_3 with 527 nF, the operating frequency is 6.80 MHz and the

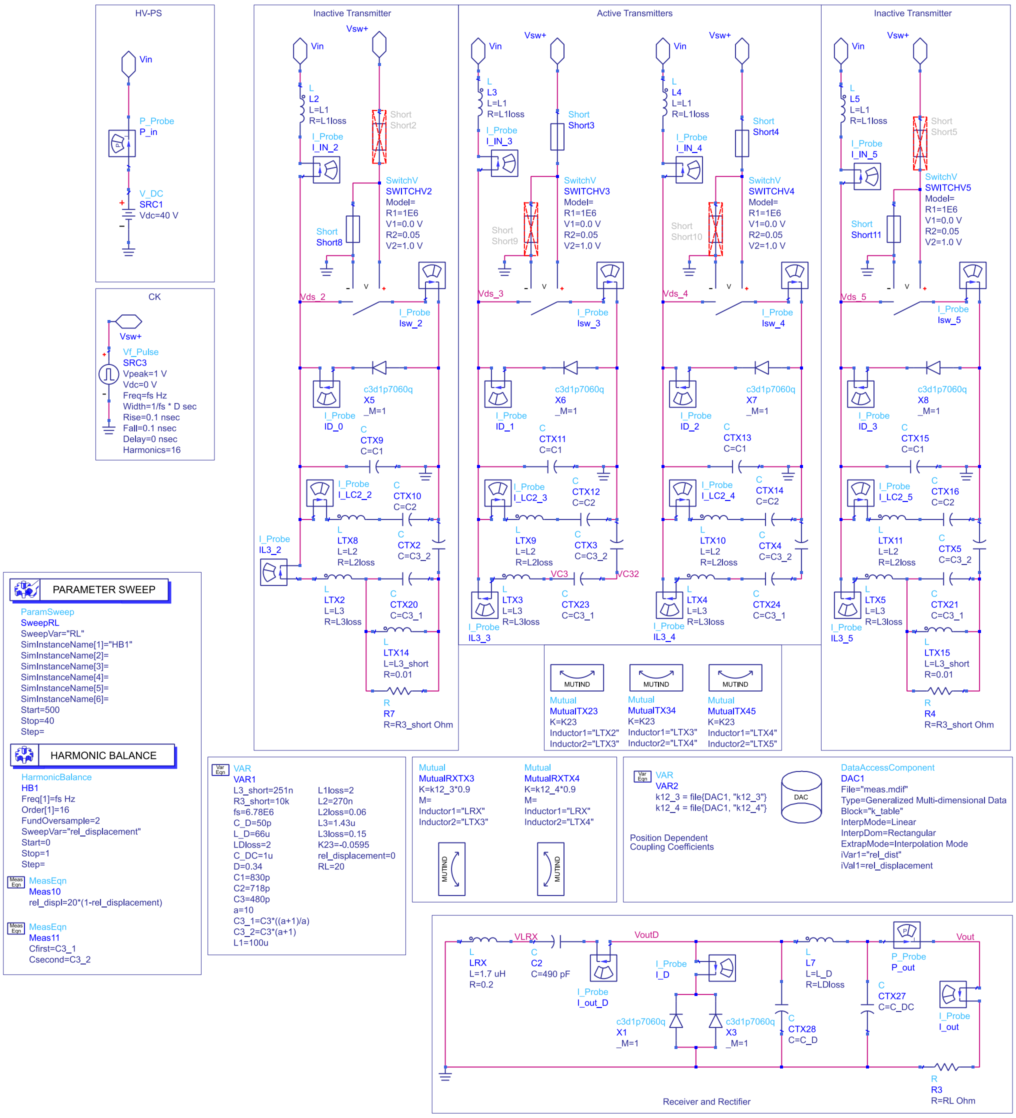

Figure 2.39: ADS [72] simulation of the system. Each inverter is simulated with equal components. Zoom in to see the details of the simulation.

duty-cycle $D = 0.73$. The signal to the gate driver (signal generator) has a $V_{pp} = 4\,\mathrm{V}$ and an offset of $V_{off} = 2\,\mathrm{V}$. The voltage to the GaN is set to

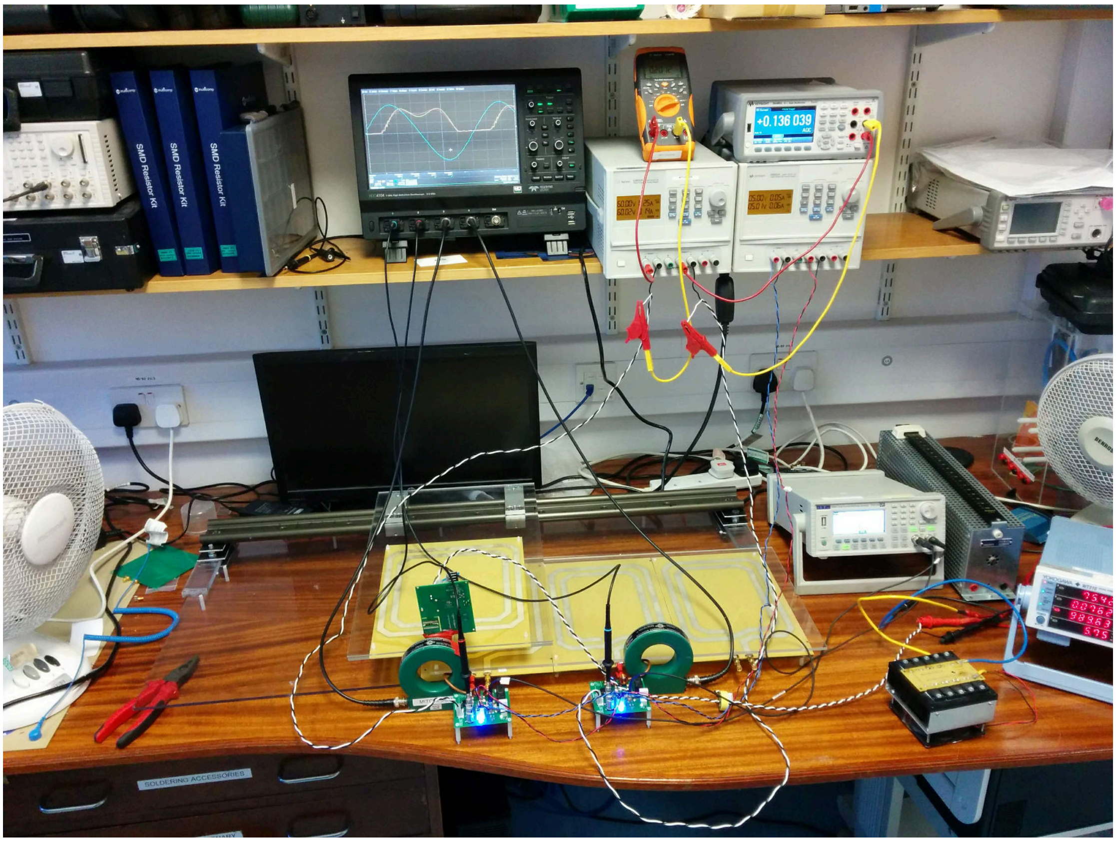

Figure 2.40: Measurement setup, with the current transformers.

5 V, the same of the logic.

2.4.6.3 Numerical Solution with Minimum Variance

The most convenient solution is obtained by minimizing the unbiased variance when the receiver is aligned with each transmitter for a set of loads. This is an estimator for α_1 which provides the best fit of the measured data to the mean, because the Mean Square Error (MSE) of each measured $I_{Ndc_{(1,k)}l}$ from the mean is minimized.

For convenience, it is implemented in Python and the key code is in listing 1, which results in $\alpha_1 = \left(\alpha_{(1,1)}, \alpha_{(1,2)}\right) = (0.0094, 0.0094)$ for the simulation and $\alpha_1 = (0.0126, 0.0272)$ for the measured setup. As expected, the coefficients from simulations are equal, while the measured ones differ for each transmitter. The plots with these α_1 are shown in fig. 2.41. The lines are well superimposed and therefore provides a position sensing method with a reduced error: each position is uniquely related to $I_{Ndc_{(1,k)}l}$. The defective Tx3 increases the error near 20 cm and hence the lines are more spread out. The simulated $I_{Ndc_{(1,k)}l}$ is not smooth near the midpoint because there is a high slope variation and therefore that region has a higher error when approximated with linear segments. A simulation with more points would provide a smoother plot near the midpoint, but is not necessary in this specific case.

```python
def res(alpha_1):
    alpha_11, alpha_12 = alpha_1
    INdc11l_meas = ((Idc1_meas - alpha_11 *
    ↪   iac1_meas)/(Idc1_meas + Idc2_meas - alpha_11 *
    ↪   iac1_meas - alpha_12 * iac2_meas))

    INdc12l_meas = ((Idc2_meas - alpha_12 *
    ↪   iac2_meas)/(Idc1_meas + Idc2_meas - alpha_11 *
    ↪   iac1_meas - alpha_12 * iac2_meas))

    var_INdc11l = scipy.var(INdc11l_meas, axis=0, ddof=1)
    var_INdc12l = scipy.var(INdc12l_meas, axis=0, ddof=1)

    return var_INdc11l[1] + var_INdc12l[-1]
    # return scipy.sum(var_INdc11l + var_INdc12l)

alpha_opt = scipy.optimize.minimize(res, [0,0])['x']
```

Listing 1: Minimum-variance estimation of the coefficient α_1 and implemented in Python. The optimization of the variance is done only when the coils are aligned to focus the locating precision in this low sensitivity region.

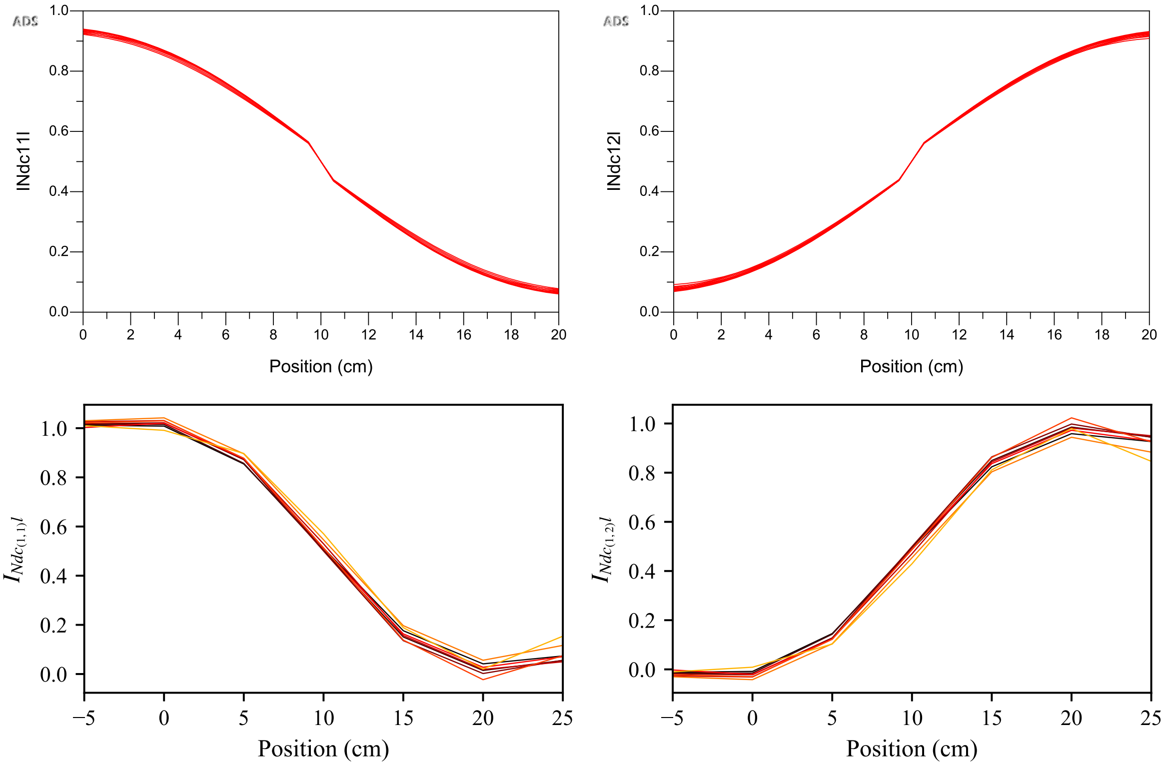

Figure 2.41: $I_{Ndc_{(1,k)}}l$ with α_1 obtained by minimizing the variance. $\alpha_1 = \left(\alpha_{(1,1)}, \alpha_{(1,2)}\right) = (0.0094, 0.0094)$ for the simulation (top plots, with ADS logo) and $\alpha_1 = (0.0126, 0.0272)$ for the measured setup (bottom plots). Each line is a different load. Note that the range of positions for measured data is increased on the two sides, going further than the centers aligned. It confirms the expectations, since it remains near one.

2.4.6.4 Solution from Idle Currents

A simplified method is to solve eq. (2.47) with an idle load, which is when the receiver is removed and the load impedance of the inverter is only the residual inductance. To do this we must suppose that the underlying behaviour of the losses against load changes is perfectly linear, either increasing or decreasing, and therefore that the inverter maintains exactly the same α_1 for all the loads, from idle to the maximum load (lowest load resistance or maximum power).

In these conditions $\alpha_{(1,k)}$ is:

$$\alpha_{(1,k)} = \frac{I_{dc_{(k)\text{idle}}}}{i_{ac_{(k)\text{idle}}}} \tag{2.48}$$

Note that $I_{dc_{(1,k)}l}$ is zero when the receiver is removed and therefore the idle currents are not affected by the receiver position. A single measurement of the idle currents in each couples of inverters is sufficient to retrieve the coefficients.

From simulations, both Tx2 and Tx3 have a dc idle current of 0.071 A and an ac current of 4.812 A, and therefore $\alpha_1 = (0.015, 0.015)$. From measurements, Tx2 has a dc idle current of 0.055 A and an ac current of 4.151 A, while Tx3 has a dc idle current of 0.117 A and an ac current of 4.246 A, resulting in $\alpha_1 = (0.0132, 0.0275)$ The plots with these α_1 are shown in fig. 2.42 Surprisingly, this method does not work with the simulation data but works well with the measured one, with only a slightly higher variance than the more rigorous method. This is a nice finding, since it allows a straightforward initial calibration and needs only a measurement of the idle currents for each transmitter in each couple. The simulations, as plotted in fig. 2.34(b), predicts a lower efficiency with higher load resistances and therefore the resulting coefficient computed using idle currents is inevitably higher. A possible reason is the simulation model of the switch, which is simplified to a on resistance and a parallel linear capacitance, that could overestimate the switching losses due to higher peak currents.

2.4.6.5 Estimation of the Inverter Losses

Since $I_{dc_{(1,k)}\text{loss}}$ was demonstrated to be a good approximation for the losses, it could be interesting to visualize which are the expected losses in the inverters. Figures 2.43 and 2.44 show the losses through the currents $I_{dc_{(1,k)}\text{loss}}$, but they can be simply translated to powers by multiplying them to the input voltage (in this case 40 V).

The interesting, while counter-intuitive, result is that higher loads (lower dc load resistances and higher dc powers) have lower losses. Another

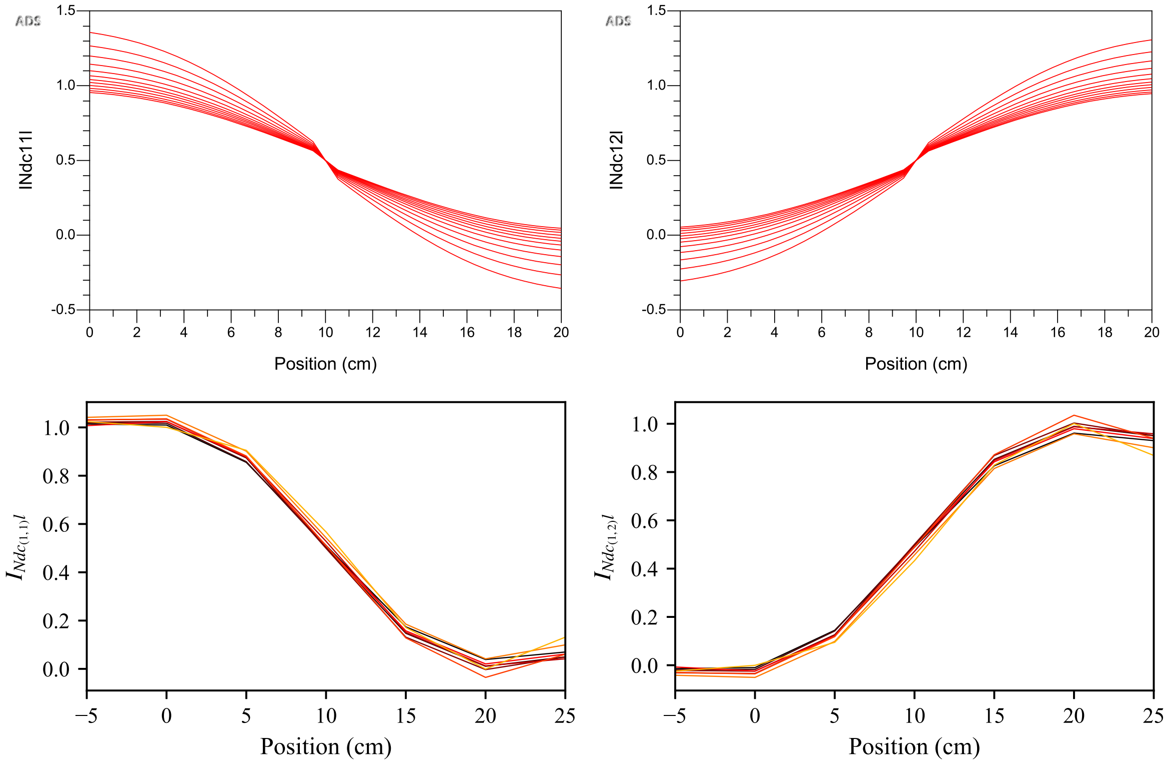

Figure 2.42: $I_{Ndc_{(1,k)}l}$ with α_1 obtained by eq. (2.48). $\alpha_1 = (0.015, 0.015)$ for the simulation (top plots, with ADS logo) and $\alpha_1 = (0.0132, 0.0275)$ for the measured setup (bottom plots). Each line is a different load. Surprisingly, this method works only with measured data.

interesting result is that measured losses are only slightly influenced by the position of the receiver, which means that the losses depends on the mutual coupling between the transmitters and not simply on how each inverter is singularly loaded.

2.4.6.6 Implementation of the Position Sensing in a Real System

The previous analysis provided a set of relations between the position and the measured $I_{Ndc_{(1,k)}l}$.

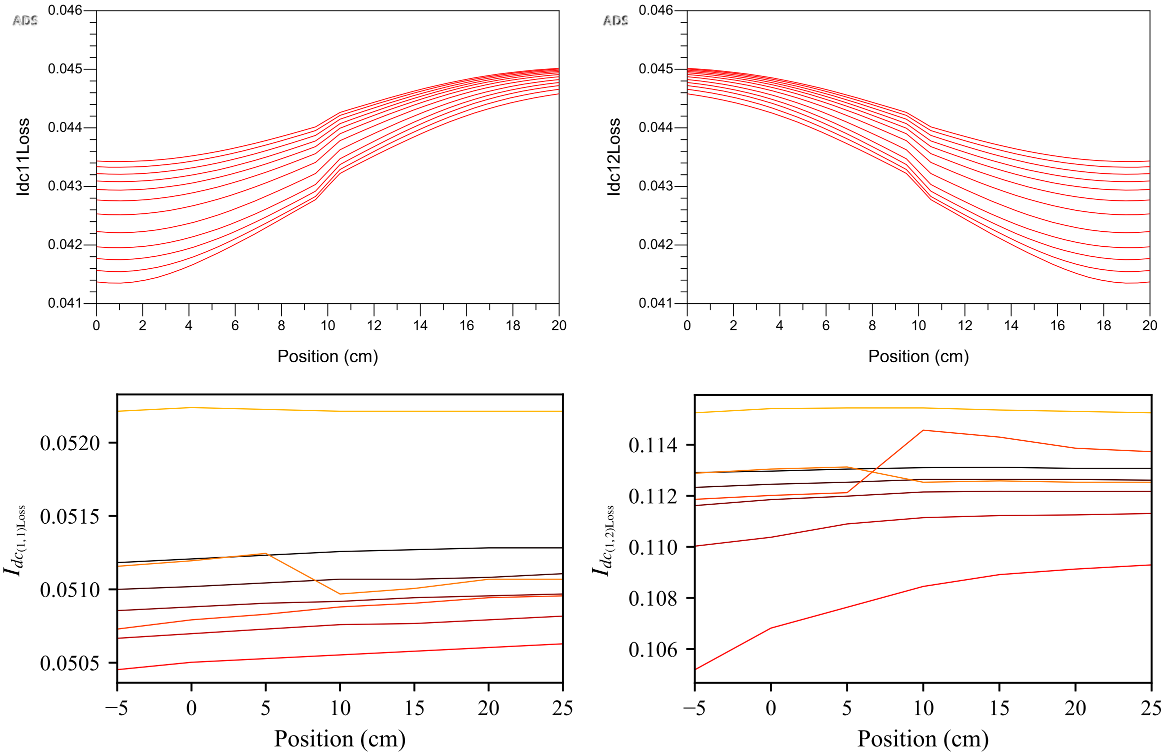

Figure 2.43: Estimated loss currents in each transmitter, using α_1 obtained from the minimization of the variance. The plots above use simulated results, below the measured ones. Higher output powers have lower losses. Measured results are only slightly influenced by the position of the receiver and are sensibly different in the two inverters. They can be simply translated to watts by multiplication with the input voltage (in this case 40 V).

The method that minimizes the variance estimates the α_1 that provides the best fit of the set of $I_{Ndc_{(1,k)}l}$ to their estimated expected value $\mathbb{E}_{R_L}[I_{Ndc_{(1,k)}l}]$. The expected value can be interpolated and the resulting function is called $f_{(1,k)}$. Then $f^{-1}_{(1,k)} \circ I_{Ndc_{(1,k)}l}$ will directly return the position of the first receiver. Note that, to avoid misunderstandings, here $I_{Ndc_{(1,k)}l}$ refers to the function in eq. (2.47) while for the expected value it is a random variable. Previously, the set of measured $I_{Ndc_{(1,k)}l}$ were numerical values.

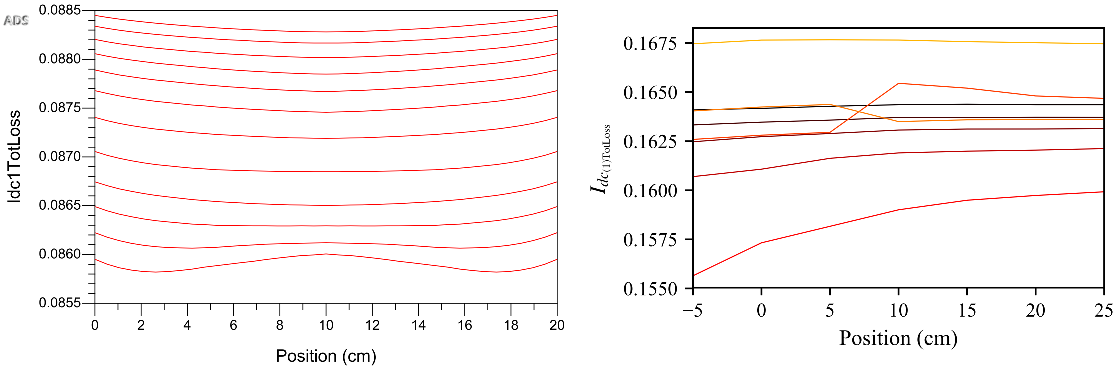

Figure 2.44: Estimated total loss current ($I_{dc_{(1)\mathrm{TotLoss}}} = I_{dc_{(1,1)\mathrm{Loss}}} + I_{dc_{(1,2)\mathrm{Loss}}}$) in a couple of transmitters, α_1 are obtained from the minimization of the variance. The plot on the left is from simulated data, the one on the right from measured ones. They can be simply translated to watts by multiplication with the input voltage (in this case 40 V).

An python example is shown in listing 2 with the graphical representation in fig. 2.45.

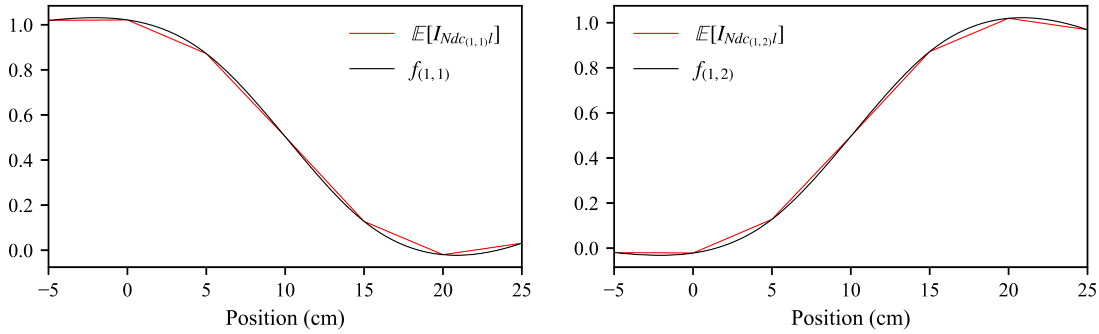

Figure 2.45: Expected value and interpolating function for position sensing. Inside the 0 cm to 20 cm range, the distance can be uniquely retrieved.

With those functions, it is sufficient to provide the instantaneous readout of the input dc currents and the peak of the current in the transmitter to retrieve the position. α_1 and $f^{-1}_{(1,k)}$ are computed and stored from the initial

```
E11 = sc.mean(INdc11l_meas, axis=0)
E12 = sc.mean(INdc12l_meas, axis=0)
f11 = sc.interpolate.interp1d(position_meas.T[:,0], E11.T,
 ↪  'cubic')
f12 = sc.interpolate.interp1d(position_meas.T[:,0], E12.T,
 ↪  'cubic')
f_inv11 = lambda I: sc.optimize.root(lambda p,I: f11(p) - I,
 ↪  [10], (I))['x']
f_inv12 = lambda I: sc.optimize.root(lambda p,I: f12(p) - I,
 ↪  [10], (I))['x']

def find_pos1k(Idc1_meas, Idc2_meas, iac1_meas, iac2_meas,
 ↪  alpha_1, f_inv1k):
    return f_inv1k(((Idc1_meas - alpha_11 *
     ↪  iac1_meas)/(Idc1_meas + Idc2_meas - alpha_1[0]*
     ↪  iac1_meas - alpha_1[1] * iac2_meas)))
```

Listing 2: Python script to implement $f^{-1}_{(1,k)} \circ I_{Ndc_{(1,1)}l}$. $f_{(1,1)}$ is obtained by interpolating the mean of all the measured $I_{Ndc_{(1,1)}l}$, which is then inverted to get $f^{-1}_{(1,1)}$. The input of $f^{-1}_{(1,1)}$ is simply output of $I_{Ndc_{(1,1)}l}$. The same approach works also for $f^{-1}_{(1,2)} \circ I_{Ndc_{(1,2)}l}$.

calibration, and they are dependent of the specific inverter and configuration. They requires to measure the currents with a set of loads and positions, the same needed for solution with minimum variance.

If the approach needs to be embedded in a system without python, $f^{-1}_{(1,2)}$ can be precomputed from the initial calibration, which is only needed once, using listing 2 and the values included in a lookup table, while $I_{Ndc_{(1,2)}l}$ uses directly the expression. Otherwise $f^{-1}_{(1,2)}$ can be stored as the interpolating function and listing 3 shows an example.

Just a note, obviously it can not locate an open dc load, which is transparent to the transmitters, but it can locate a small load, which could be seen as the receiving system is inactive and drawing the minimum current.

```
point = (3,4)
InstIMeas = (Idc1_meas[point], Idc2_meas[point],
 ↪  iac1_meas[point], iac2_meas[point])
print('Currents: ' + str(InstIMeas)[1:-1] + ' A')
print('Load: ' + str(Rload_meas[point])+' Ohm\n')

position = find_pos1k(*InstIMeas, alpha_opt, f_inv11)
print('find_pos11(' + str(InstIMeas)[1:-1] +
      ', alpha_opt, f_inv11): ' +
      str(position)[1:-1] + ' cm')
print('Real Position: ' + str(position_meas[point]) + ' cm' +
      ' / ' + 'Error: ' +
      str(position - position_meas[point])[1:-1] + ' cm')
```

```
Currents: 0.1123, 0.4428, 4.036, 4.092 A
Load: 100.192 Ohm

find_pos1k(0.1123, 0.4428, 4.036, 4.092, alpha_opt, f_inv11):
 ↪  14.89696918 cm
Real Position: 15.0 cm / Error: -0.10303082 cm
```

Listing 3: Test of the algorithm using the calibration data in a sample point. In the real system the currents are instantaneous readout in the circuit, while here are taken from measured data to give an example. The precision is impressive: the error is only 1 mm. The maximum error on the measured data is 3.5 cm, which is obtained at 20 cm. With a properly functioning Tx3, the error is expected to remain below 2 cm.

In our case, the only need is to provide a position to tell where to change the active inverter: probably the previous approach is an overkill. A simple threshold on the instantaneous value $I_{Ndc_{(1,k)}l}$ is sufficient to know when the receiver is aligned to a certain transmitter. The advantage of setting a threshold is to avoid the complete set of measurements needed to get the calibration and therefore to take full advantage of the simplified approach using only the idle currents.

The advantage of this system is to provide a completely passive measurement of the position, without any feedback from the receiver, but only some additional sensing circuits. To sense the dc currents is extremely simple and can be done with a shunt resistor and an integrated precision current sensing ADC. The ac current is a bit more complex but it can be reduced to an additional coil inside the transmitter, which is connected to a peak detector and then to a precision voltage sensing ADC. The mutual impedance between the transmitting coil and its sensing coil needs to be characterized only once in the lab, for example measuring a sample coil with a VNA. Then, since the current in the sensing coil is approximately zero, the peak current in the transmitter is simply the peak voltage in the detector divided by the mutual impedance. The voltages can be high and a simple resistive divider with few hundreds of kΩ would suffice. The above method works because the current in the transmitter is sinusoidal, otherwise each harmonic would have a different impedance and a different ratio. Notice that this is not a broadband transformer, which needs high secondary reactance and maintains a constant voltage to current ratio.

An on-board control system, for example a small micro-controller, reads the data from the ADC and sends them to a central controller which provides the control of the active switches and the calibration part. The hardware is the same for both the minimum variance and the idle current approach, with the difference being only in the calibration process. It was not built for time reasons, since it requires quite a lot of time for the implementation of the control system, but it is technically straightforward.

2.4.6.7 Inverter Selection through a Threshold

The way to decide when to change the active coil is straightforward: when the normalized current is above a certain threshold, p.e. 0.95, it is safe to switch down the preceding and switch on the following. To know which is the preceding and which is the following, a rule of thumb is to subtract the index of the active inverter with the highest current to the one with the lowest, then to add number to the inverter with the highest current. If we denote the inverter with the highest current using $\mathrm{Tx}_{\mathrm{n_H}}$ and $\mathrm{Tx}_{\mathrm{n_L}}$ for the one with the lowest current, the one to turn on is $2\mathrm{n_H} - \mathrm{n_L}$. For example, if we are located in 20 cm, $6 - 2 = 4$, therefore the transmitter to be powered is the number 4. If we are located in 0 cm, $4 - 3 = 1$, therefore the transmitter to be powered is the number 1. In both cases the one to be turned off is $\mathrm{Tx}_{\mathrm{n_L}}$, obviously.

The precision depends on how well the lines are superimposed, which in turn depends on the losses in the active device and, for example, Tx3, with its defective GaN, provided less precision than Tx2. The other source of error is the nature of the curve, being steeper with the receiver between the two coils and flatter when aligned. Since the switching point is where the transmitter and receiver are aligned, it provides unfortunately the lower sensitivity. This is a sufficient precision to switch the active transmitter, since there the contribution to the transferred power from the transmitter to be replaced is low (5% if the threshold is 0.95) and its real contribution is only to properly load the other inverter. Indeed, in each moment the inverters must operate as a couple, otherwise the inductive load would be different, losing the ZVS and damaging the inverter.

Note that the additional precision of the more rigorous method is minimal for a threshold based solution and the additional complications are probably not worth the trouble, but it is more stable and provides more predictable results, which could be of high value. The decision should be made based on which system will control the inverters and, if capable, it is advised to use the minimization of the variance, due to its superior stability. An additional use of the simplified method is to provide a way of updating the α_1: the simple measure of the idle currents can be done periodically on stage to keep an eye on its drift.

2.4.7 Remarks

- The *virtual series* is able to maintain a constant output voltage, independent of load and position variations:
    - The series is obtained by forcing the same current via Coupled

  Load Independent Class EF Inverters;
  - The operating frequency is 6.78 MHz, providing sufficient coil quality factor to get high link efficiencies;
  - The output power is tested up to 100 W, with a peak dc-to-dc efficiency of 80%;
  - The inverter maintains the ZVS for each load and position;
  - An optimized Class E rectifier provides a load independent output voltage and reflected reactance to the inverter, which can sustain only resistive variations;
  - The variations of the output voltage with load and position changes are extremely reduced;

- The Coupled Load Independent Inverter allows the passive sensing of the receiver position by a simple readout of the currents in the input (dc) and in the transmitting coil (ac):
  - An estimator is provided, where the coefficients must be retrieved by an initial calibration;
  - A rigorous method minimizes the variance of the estimator; It requires a full initial calibration with a set of loads in different positions and a python implementation is proposed, which can be also translated to a lookup table for embedded systems;
  - A simplified method, suitable only for a threshold sensing because it does not provide the data to build the locating function $f_{(1,k)}$ is provided;
  - A possible hardware implementation for the sensing is outlined.

- The system is fully modular and can be adapted for any desired length:
  - Since the power bus is in dc, the parasitics doesn't limit the length;
  - A mechanism for the replacement of the active switch in the couple is provided.

2.4.7.1 Advantages over the Real-Series (section 2.3)

- The feeding of each module is in dc:
  - The parasitics of the lines are not influencing the link, which can be theoretically unlimited in length;
  - The resonance frequency does not change depending on the position;
- There is only one active switch (1 FET) instead of 3 (6 FETs), reducing sensibly the losses and therefore increasing the efficiency;
  - The parasitics of the single switch are included in the inverter;
  - There are no stray resonances or over-currents;
  - The switches are not required to be bidirectional (only two quadrants, as a FET and a parallel diode, instead of four quadrants);
  - Higher frequencies possible, with the limit being the FET and its driver;
- It is possible to sense the position of the receiver from the transmitting side;

2.5 High-Throughput Data Link

The simultaneous transfer of power and data to moving objects is still an open issue and significant research activity is dedicated to provide a reliable data link.

A possible solution is to use the Near Field Communication (NFC) and include the data link as a perturbation of the power link or to use a different frequency, but since the bandwidth is very narrow, the data rate is very low, below few Kb/s. Using the same means needs also to make a trade-off, between sending a single sinusoid that would maximize the efficiency of the power transfer and the waterfilling allocation, which is the optimal strategy for maximum communication rate [78].

A different method is to use a dedicated RF link, which has the capability to allow higher data rate. This could use a dedicated and simplified transceiver, which is still transferring few byte per second and is useful for niche applications [79], or use a fully fledged commercial solution, which can provide very high data rates and can be applied to general applications.

A typical commercial and cheap consumer solution is provided by a WiFi transmitter, capable of delivering hundreds of Mb/s. This kind of systems are not intended for industrial scenarios and therefore a high environmental noise and interference must be taken into account as they are not guaranteed to work in these conditions. To overcome the issue, the link must work with a very low link attenuation, providing enough received power and a sufficient signal to noise ratio. A design of such a system will be discussed in the following sections, initially on the electromagnetic part, where the antennas and the rf switch network are designed, to the network layer, which provides high data rate access to the elements in the network. Finally, the prototype of a data and power system is presented and tested.

2.5.1 RF Link and Antenna Design

This section discusses the electromagnetic design of the data link, built on the 802.11ac WiFi protocol over the 5 GHz band. The decision to adopt the 5 GHz band is based on the impressive data throughput, above 100 Mb/s, possible using cheap consumer hardware and on the requirements of a small

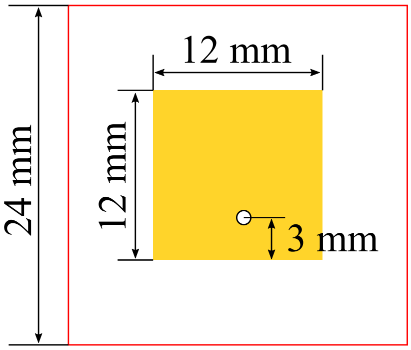

Figure 2.46: Layout of the patch antenna. The red square is the ground plane, while the yellow area is the the patch itself. The feeder is shown as a hole.

antenna.

The idea is to replicate the same mechanism implemented to activate the inverters, as in fig. 2.12, with a Multiple Input Single Output (MISO) link. Two transmitting antennas are connected and managed by a two port WiFi access point, which is in charge to exploit the MISO channel with the single antenna receiver. Unfortunately, this solution does not allow to inspect the algorithm for the diversity scheme in the access point, due to its closed source nature, and therefore we must trust the access point vendor to have an algorithm which is suitable to our scheme. There could be some possibilities of interacting with the algorithm using OpenWrt [80], but it is outside the goal of this project and overly complicated for the possible additional benefits.

The design of the antenna is very simple and focused on reducing costs. The choice is for a square patch antenna, operating at 5.24 GHz and placed in the center of the coils, which basically behave as an open circuit at the IPT frequency of 6.78 MHz and therefore the mutual interference between the RF and power part is minimum. Both structures are planar and designed to be realized on the same FR-4 substrate ($\tan\delta = 0.025$, $\varepsilon = 4.5$), which provides a cost effective structure. The antenna has a bandwidth of 237 MHz (reference fixed at -10 dB) around a frequency of interest of 5.24 GHz. The length of each side is 12 mm, small enough to expect no interference with

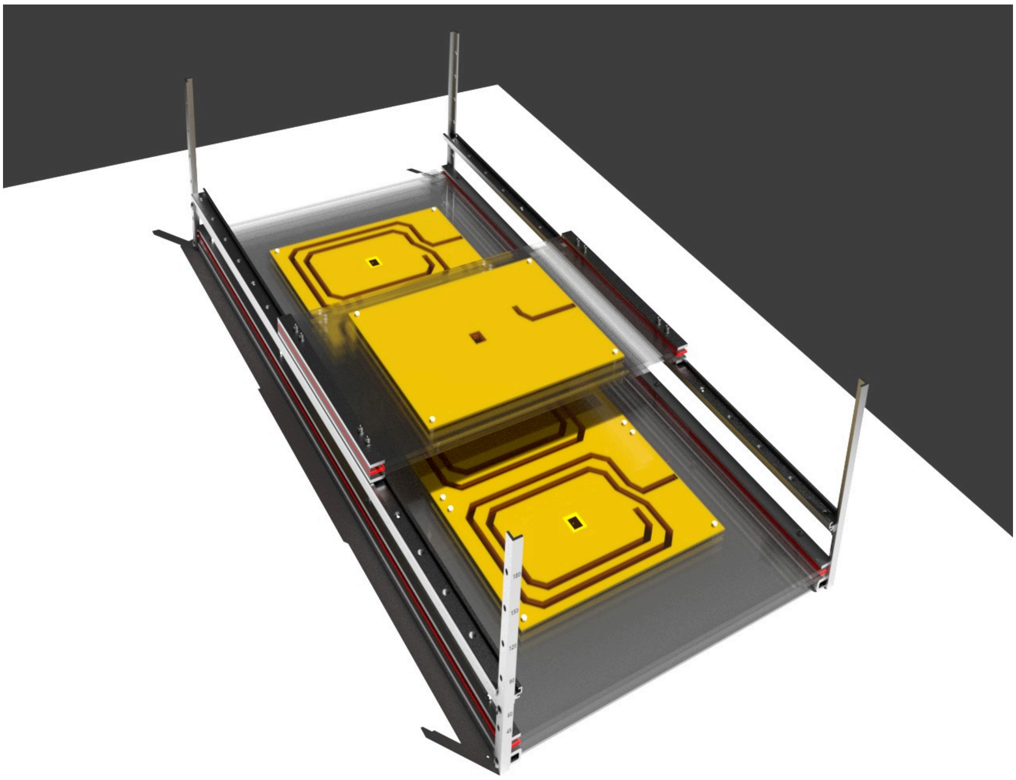

Figure 2.47: A Blender (Cycles) [81] render of the 3D model made in FreeCAD [82], used for the (in-house) mechanical realization, shown in fig. 2.52. The antennas are in the center of each coil and the transmitting ones are activated as a couple, the same as the active inverters.

the power part, with the feeding provided through a coaxial in a ground plane hole at 3 mm from the outline, as in fig. 2.46.

The choice of FR4 dramatically decreases the efficiency of the antenna, since the substrate is very lossy and variations of permittivity are not negligible at 5 GHz, but the effects on the performances should be minimal. Indeed, as shown in fig. 2.47, the distances between the transmitters and receiver are much smaller than usual WiFi links, with a maximum of 25 cm (see also fig. 2.26), that can have a range up to hundreds of meters. This provides a very low link attenuation and therefore a very strong signal, which yields a high Signal to Noise Ratio (SNR) even in presence of strong noise or interference in industrial scenarios.

The receiving coils slides as in section 2.1, from the receiver aligned with the transmitter to the midpoint, with the dimensions exactly as in section 2.4. In fig. 2.48 the link attenuation is compared in different position and it is possible to see that there is a compensation between the two antennas. The measurements, done with an Agilent FieldFox N9923A Vector Network Analyzer, show a similar behaviour but with a quite higher attenuation, which is probably due to tolerances in the substrate, which is not designed for RF applications, and to the effect of the environment and the metallic structure. The behaviour is consistent between simulated and measured

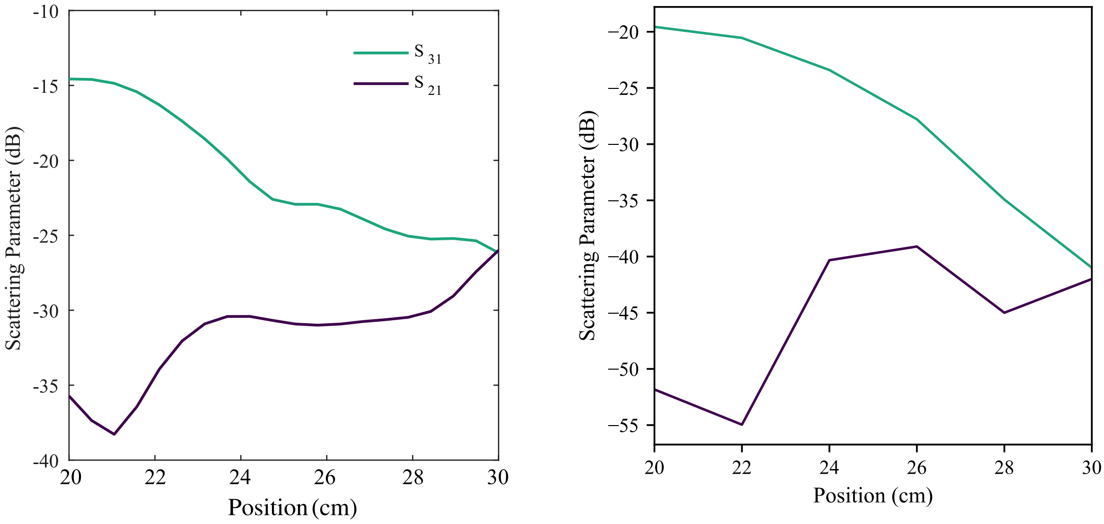

Figure 2.48: Simulated (left) and measured (right) 5.24 GHz link budget from each transmitter to the receiver. The translation is the same as in section 2.1, from both centers aligned to the receiver in the midpoint. The remaining (missing) half is the mirrored version of the first half.

data, where there is an increase of the attenuation when the distance is increased due to the movement.

With 20dBmW in input (100 mW as per WiFi regulations), the received power is always over −20 dBmW, which means a very high margin, more than 30 dB over the sensitivity for the 256-QAM modulation with a channel bandwidth of 160 MHz, the most demanding case with the higher data throughput, or a very high 60 dB for the BPSK with a 20 MHz channel [83].

A block diagram, representing a slice of the system, is shown in fig. 2.49. The WiFi Access Point must be 802.11ac compliant, operating on the 5 GHz band and with two ports (Multiple Input). Each port is connected to a different line, to feed the even or odd module. The RF line is designed as a chain, which, if not powered, passes the signal to the following block. The drawback of this choice is an additional attenuation, which would require few repeaters along the track to restore the signal.

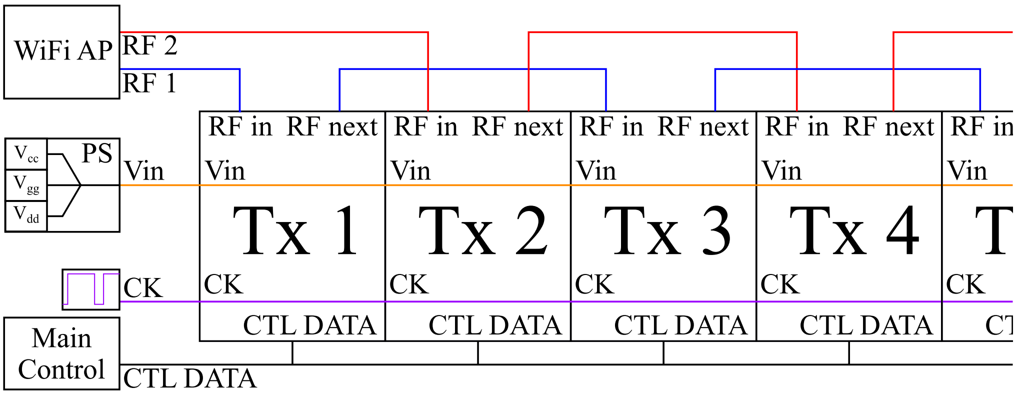

Figure 2.49: Block diagram representing a slice of the system, where each transmitter is a module. Each module is identical and shown in fig. 2.50.

A possible, but more expensive, alternative is to include a single antenna access point in each module using the same network SSID. A possibility is also to reduce the number of access points to every few modules, which should still provide a reliable channel, but it is a different architecture. Anyway, those alternatives are just hypothesis and they were not developed, as we think the single transmitter method is superior.

The power bus (orange line) consists in three supply lines, one for the logic ($V_{cc} = 5\,\mathrm{V}$), one for the GaN gate ($V_{gg} = 5\,\mathrm{V}$) and one for the power input ($30\,\mathrm{V} < V_{dd} < 70\,\mathrm{V}$). The clock line supports a square wave with 73% duty-cycle between 0 and 4 V at 6.78 MHz. The control data (CTL DATA) is intended for signaling between the inverters and the main control, for example using the CAN-BUS. This is used to activate the right inverters and to compute the coefficients, which can be stored in the main controller. In the prototype the designed main controller is provided by a RaspberryPi3 [84], but the control part inside each module is missing due to time constraints.

Each transmitter is an identical module, as shown in fig. 2.50, and consists of an IPT and a RF part. The IPT is made by the inverter and the coil, while the RF by the switch and the antenna. There is a micro-controller

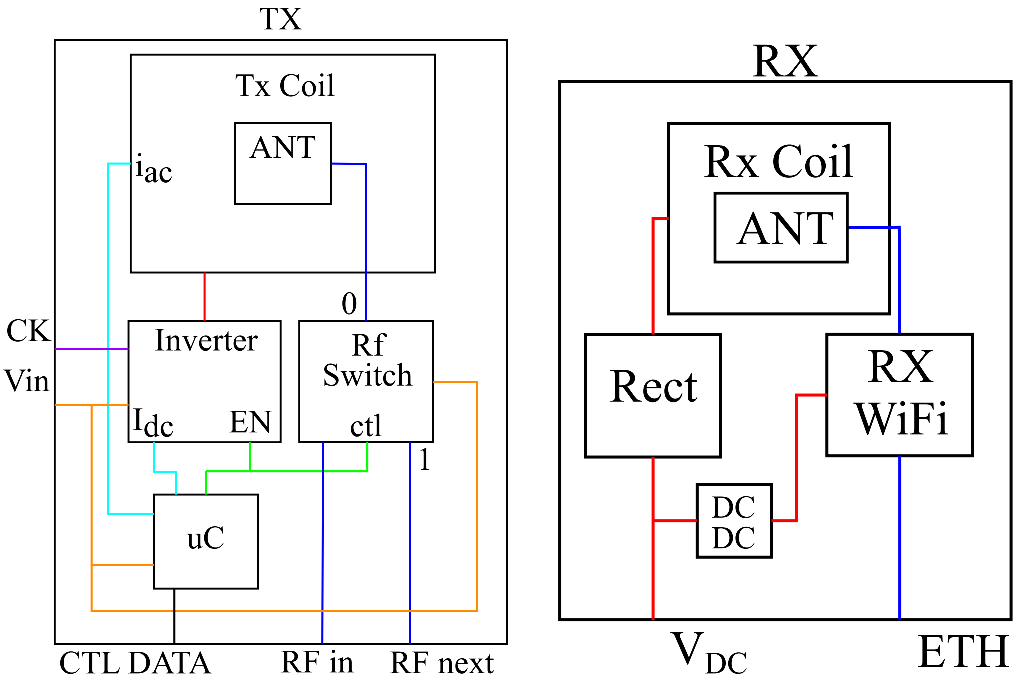

Figure 2.50: On the left is a block diagram of a transmitting module, while on the right is the receiving one.

which has the duty to activate the inverter, to read its currents and to connect the antenna when instructed via the control bus (CTL DATA). The switch has the duty to connect the RF signal to the antenna, when the antenna has to be powered, or to pass the signal to the next module.

The receiving module is also composed of the IPT part, consisting in the coil and the rectifier, and the RF part, which is the WiFi receiver and its antenna. The additional DC-DC converter is to power the WiFi receiver from the received power. The outputs of the receiver are the received power and the data, for example via an ethernet cable, as will be shown in section 2.5.2.

Unfortunately, in the prototype shown in fig. 2.52, the RF switch network, the control system and the additional DC-DC in the receiver were not included. Time constraints and less scientific interest, were the reason for using only a couple of modules and for connecting directly the antennas to the access point.

2.5.2 Network Layer and LAN Infrastructure

This section discusses the implementation of the network side, which leverages the data part to provide a complete solution.

Figure 2.51 shows the configuration of the network layer, built around the link made of the two transmitters and the receiver. The access point is connected directly to the transmitting antennas, on RF side, and to the router, on the LAN side.

The RPi3 (2) acts as the main controller, in charge of configuring and commanding the transmitters. It is connected to the data network, therefore accessible for its configuration or to impart commands. On the prototype, it is used as a server to test the link speed.

The router provides to the local network with access to the Internet, in a sort of Internet of Things.

On the receiving side the WiFi receiver is a usb dongle connected to the RPi3 (1), which acts as the brain of the mover. This computer has full access to the network and to the Internet, independently of the position. In an industrial scenario, this RPi3 (2) can be seen as any IoT system, for example a robotic arm. This mover can be remotely controlled, even from

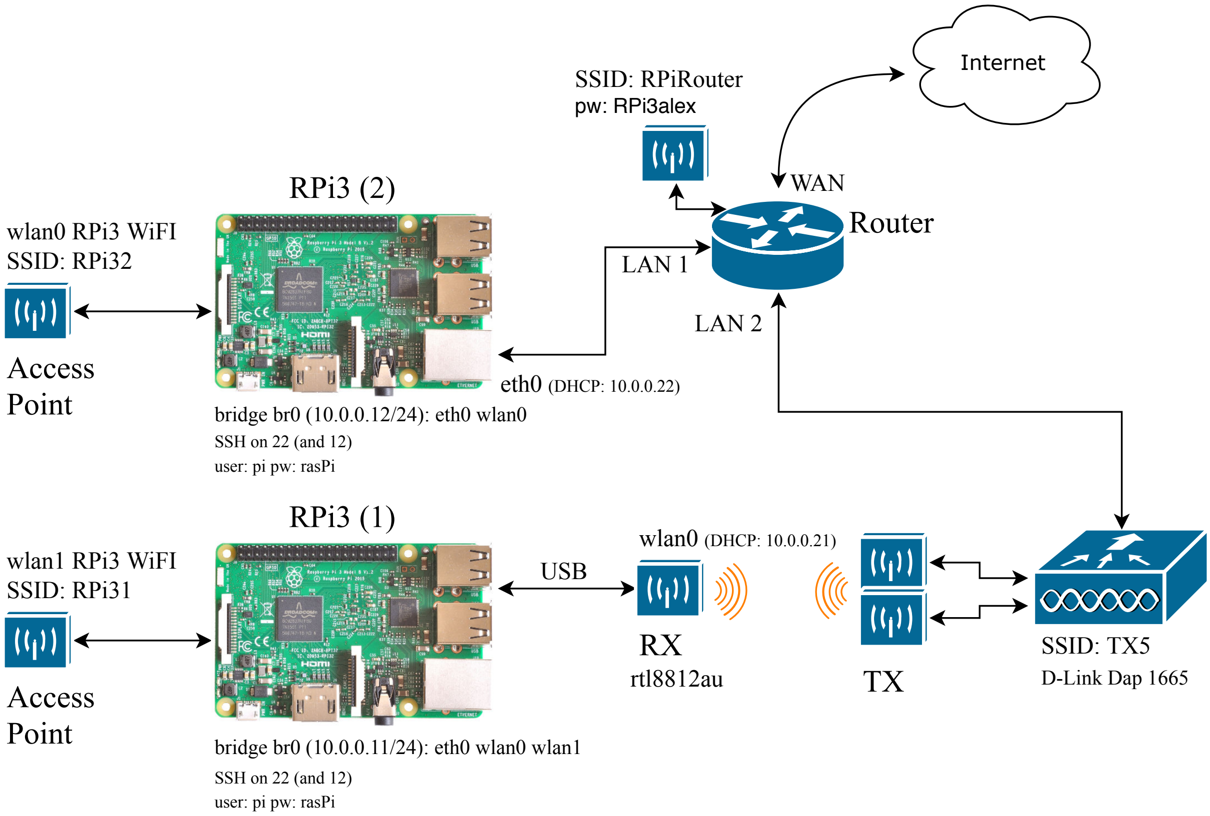

Figure 2.51: Network configuration of the prototype. The mover can access Internet independently of the position with a 100Mb/s link.

the outside, and knows its position via the main controller, which has the information from the power part. Indeed, the receiver does not know its position directly, but relies on the main controller sending the position via the RF link. The main controller can also send position dependent data or tasks. Furthermore, an Internet service can access both the position information and the mover, implementing de-facto a remote operated mover. For example, accessing the network via the RPiRouter SSID or via the Internet, gives `ssh` access to the two RaspberryPi, which is a way to operate remotely a Linux box (for example embedded in the robotic arm).

2.5.3 Measurements of the Data and Power Transfer Link

The measurement setup is shown in fig. 2.52 and consists of an aluminum and polycarbonate structure, which supports the coils and properly protects against voltage hazards. The separation between transmitters and the receiver is 6 cm, but can be varied if necessary.

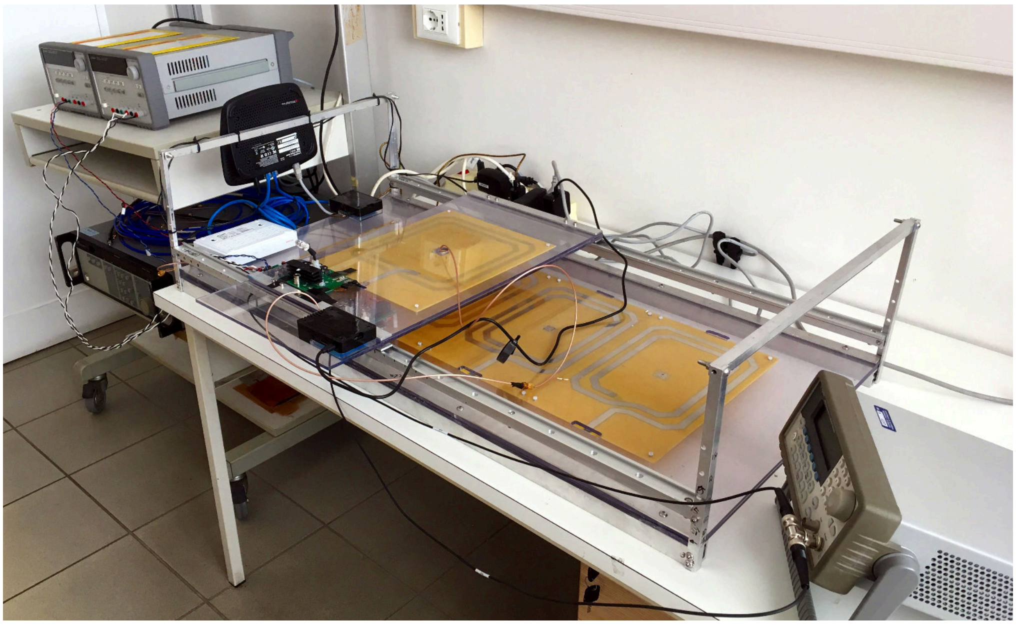

Figure 2.52: In-house realization of the measurement setup, based on the mechanical model shown in fig. 2.13, with the structure composed of polycarbonate and aluminum. The antennas are in the center of each coil and the transmitting ones are activated as a couple, the same as the active inverters.

The goal of this measurement campaign is to demonstrate that the WiFi link is not influenced by the IPT one, and vice-versa.

As discussed in the previous sections, the inverters are manually operated and only two of them are included in the setup. Additionally, the access point is directly connected to the antennas, without any rf switch.

The measurement consists in powering the two transmitters with a fixed load on the receiver and testing the data throughput of the link in each position using `iperf3`, an open source tool that run on the RasperryPi3 and is designed to test networks speeds. The RPi3 at the transmitting side acts as the `iperf3` server, while the one at the receiving side is acting as a `iperf3` client.

The measurements provides a stable and reliable 100 Mb/s data link, independent of the position and dc power. The bottleneck of the data link is represented by the ethernet cable connection to the router, which is rated for 100 Mb/s. Using a Gigabit ethernet connection higher throughput are expected. Furthermore, the `iwconfig` Link Quality and Signal Level was always 100%, confirming the very conservative design, which provides enough margin to operate with high interference. Note that the chipset of the receiver (rtl8812au) do not provide a Signal Level in dBm but as a percent, probably for some limitations of the driver.

2.5.4 Remarks

- An additional RF link based on consumer 802.11ac hardware can provide over 100 Mb/s of data bandwidth:
  - The antenna is made on the same FR4 substrate of the IPT coil, minimizing the cost;
  - The received signal has very high SNR and therefore can work in very noisy environments.
- A network implementation has been proposed, able to provide access to each element from any element of the network;
- Each element is also accessible from the outside of the LAN.

Chapter 3

Inductive Power Transfer for Medical Implants

"In questions of science, the authority of a thousand is not worth the humble reasoning of a single individual."

\- Galileo Galilei -

In recent years, the problem of wireless powering implants has been addressed with increasing interest [85], which would provide a safe and less invasive alternative to the replacement of batteries through surgery. A number of issues related to system reliability are still under investigation, for both near-field (reactive) and far-field (radiative) implementations. An interesting alternative with uses the mid-field is also under investigations and is quite promising, increasing the efficiency for longer distances [19].

In this chapter, a near-field inductive powering system at 6.78 MHz for an implanted capsule is designed with the goal of being initially insensitive to the Rx rotation on one axis, which is usually unknown, and eventually to both axes (azimuth and elevation).

Previous attempts to solve this problem are available in the literature [86], but miniaturization constraints, necessary for implantable devices, are not addressed. High efficiencies have been demonstrated in [87], in particular for short distances between the coils. However, most proposed links are optimized for static and known positions, rarely taking into account possible movements or misalignments. Indeed, when the coils rotate, the shared flux varies significantly and thus the output power and voltage [88]–[90].

The system design, from the Tx coil to the Rx dc-load, is carried out by means of EM/nonlinear co-simulation. The experimental results are performed for several distances in open air, confirming that the proposed solution allows to remotely provide the minimum required dc-power and voltage to energize the implantable device.

3.1 IPT Independent to Rotation on a 2D plane

To realize an almost constant output dc- voltage and power, for any possible receiver rotation on one axis, a 3-D configuration at the Rx side is adopted. It consists of two orthogonal coils wrapped around an ellipsoid plastic capsule, as in fig. 3.1; each one is connected to its own rectifier circuit and their dc outputs are series-connected. In this way a reduced output voltage ripple is obtained for any possible Rx rotation, ensuring continuous powering of the implant.

3.1.1 RF-to-dc Link design

In order to get rid of dark angles (or angles where a possible receiver is not provided with sufficient voltage), the design of the WPT link starts from the Tx coil input, excited by an ideal power source at 6.78 MHz. Figure 3.2 shows the equivalent circuit model of the designed IR-WPT system, while fig. 3.1 shows the first prototype photo.

A large transmitter is optimized to maximize the shared flux, and thus the kQ, in the direction of the miniaturized Rx receiver axis location. The optimized geometrical parameters are: h, w_1, w_2 and are chosen in such a way to obtain a conformal coil adaptable to be lean on the human body, for example the abdomen, to energize an implantable device in the digestive tract.

The Rx side consists of a 3-D structure with orthogonal coils wrapped around an ellipsoid plastic capsule of fixed dimensions (see fig. 3.1). From

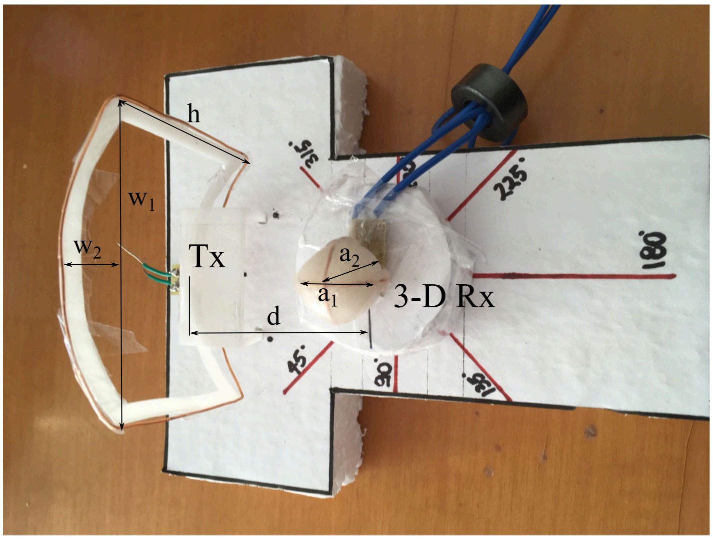

Figure 3.1: Picture of the realized prototype. Two orthogonal coils are wrapped around an ellipsoid plastic capsule with major and minor axes of $a_1 = 24\,\text{mm}$ and $a_2 = 18\,\text{mm}$ mm, respectively. The other dimensions are: $h = 52\,\text{mm}$, $w_1 = 78.54\,\text{mm}$, $w_2 = 12\,\text{mm}$ and $d = 5\,\text{cm}$ to $7\,\text{cm}$ with a $1\,\text{cm}$ step.

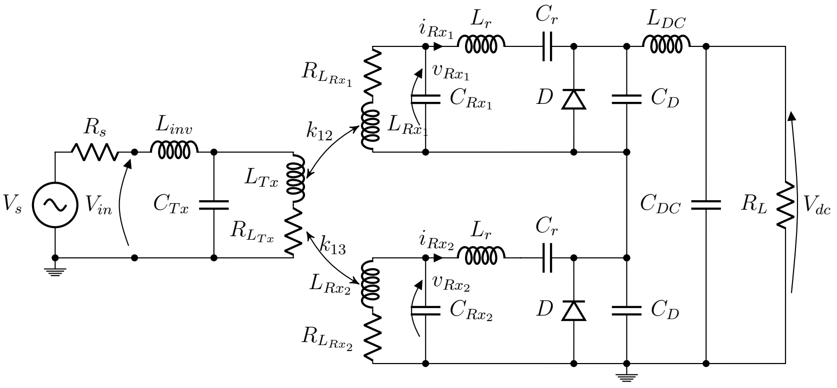

Figure 3.2: Circuit equivalent of the RF-to-dc link, the parallel compensation at the receiver side provides higher voltages to the diode.

the EM simulations of a set of RF-to-RF links, one for any possible rotation (a 0 degree rotation corresponds to one coil facing the transmitter and the other one orthogonal to it), the associated equivalent circuits parameters of fig. 3.2, including the losses, are derived and are listed in table 3.1. While the self-inductances are unchanged, the coupling coefficients clearly show the different operating conditions of each Rx coil with respect to its position: for a 0 deg rotation the k_{12} is maximum but k_{13} is negligible, while for a 90 deg rotation the coupling coefficients are almost interchanged.

A first idea could be to series connect the two Rx coils, but this would simply shift the problem of zero-coupling to other rotations, where k_{12} and k_{13} have the same absolute value with opposite signs, leading to an almost zero-coupling. This is shown in fig. 3.3 where the coupling coefficients of the series-connected coils [2] are plotted against rotation for several distance d.

Table 3.1: Equivalent circuit parameters of the RF-to-RF link, for various Rx rotations

Rotation (°)	k_{12}	k_{13}
0	1.85×10^{-2}	-1.4×10^{-5}
45	1.34×10^{-2}	1.34×10^{-2}
90	-1.88×10^{-5}	1.86×10^{-2}
135	-1.32×10^{-2}	1.35×10^{-2}
180	-1.84×10^{-2}	-3.0×10^{-6}
225	-1.32×10^{-2}	-1.33×10^{-2}
270	1.5×10^{-5}	-1.81×10^{-2}
315	1.34×10^{-2}	-1.33×10^{-2}

L_{Tx}	135 nH
L_{Rx_1}	47 nH
L_{Rx_2}	47 nH
$R_{L_{Tx}}$	45 mΩ
$R_{L_{Rx_1}}$	30 mΩ
$R_{L_{Rx_2}}$	30 mΩ

A suitable receiver topology can be realized by connecting each Rx coil with its own rectifier and by connecting in series the dc outputs. In this way, large output voltage variations and zero-zones are avoided. A class-E rectifier, shown in fig. 3.2, is connected to the Rx coil through an LC filter, in order to guarantee a sinusoidal input current. The rectifiers outputs share the same low-pass filter. The transmitter equivalent circuit is represented with a 50 Ω voltage source connected to the resonant Tx coil through the inductance L_{inv}: in this way the RF-to-RF link acts as a transformer so that source load is proportional to the system load. This

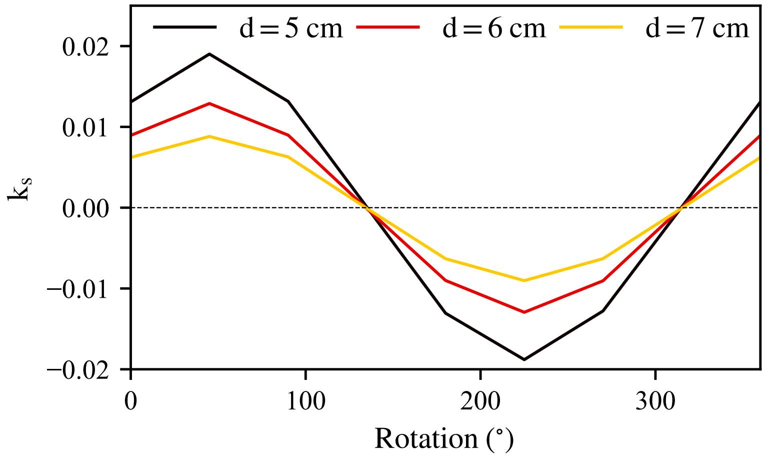

Figure 3.3: EM simulations of the coupling coefficient of the RF-to-RF link, resulting from series connection of the two Rx coils, versus Rx rotations.

solution is suitable for sources with high internal series resistance, as in the case of low-power devices powering. All the circuit elements, including the capacitances C_D, connected at the rectifiers outputs, and the dc load, are optimized by means of Harmonic Balance technique, using 7 harmonics plus dc. This is a multi-circuit non-linear optimization since, for each rotation, different coupling factors are used in the equivalent circuit. The optimization goals in ADS are to maximise the output voltage and minimise the variance. Furthermore, several voltage source amplitudes are considered. The optimum obtained load is 320 Ω.

3.1.2 Simulated and Measured Results

A first prototype, resulting from the multi-circuit optimization, that is from the Tx input port to the dc output, is built and a photo is reported in fig. 3.1. The final component values are listed in table 3.2: the resistances representing the coils losses are verified measuring the quality factor from the 3dB bandwidth of the unloaded series resonator through the two port measurement using a VNA [91]. The measurement setup is shown in fig. 3.4:

the Tx input is connected to a 6.78 MHz voltage source and the dc output to a multimeter. An oscilloscope controls input voltage and the voltage across $R_{L_{inv}}$.

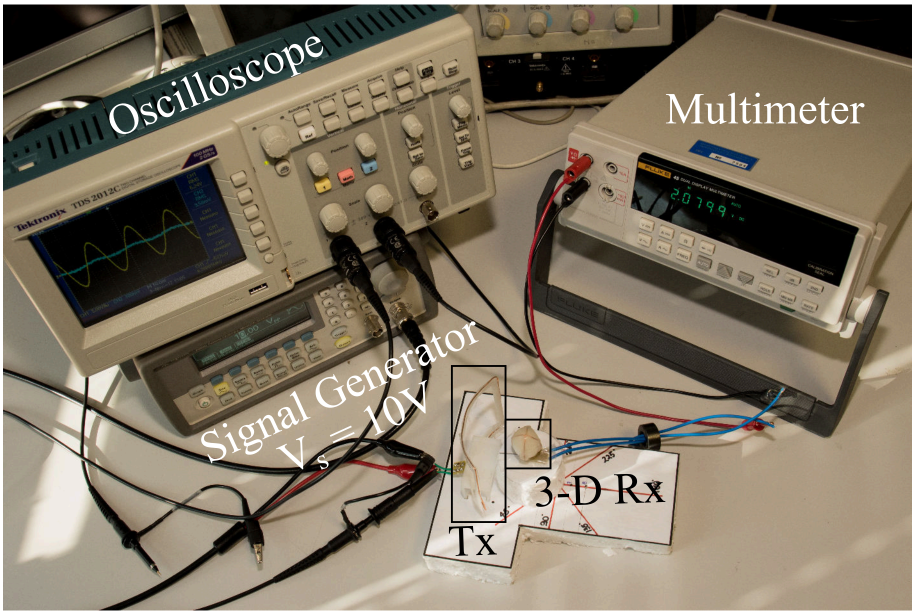

Figure 3.4: Measurement setup.

Table 3.2: Prototype components values

L_{inv}	140 nH
$R_{L_{inv}}$	1 Ω
L_{Tx}	141 nH
C_{Tx}	3.9 nF
L_{Rx_1}	53.2 nH
L_{Rx_2}	55.1 nH
C_{Rx_1}	10.3 nF

C_{Rx_2}	10 nF
$R_{L_{Tx}}$	50 mΩ
$R_{L_{Rx_1}}$	35 mΩ
$R_{L_{Rx_2}}$	35 mΩ
L_r	140 nH
R_{L_r}	1 Ω
C_r	3.9 nF
f	6.78 MHz

D	HSMS-2822
C_D	50 pF
L_{DC}	50 µH
$R_{L_{DC}}$	2 Ω
C_{DC}	20 µF
R_L	320 Ω
R_s	50 Ω

Figure 3.5 reports the simulated and measured dc-voltage on the Rx optimum load, for a Tx-to-Rx distance of 5 cm and a voltage source V_s

of 10 V: both show the effectiveness of the proposed design which ensures reduced outputs variation with capsule rotation. This is highlighted by the comparison with the results obtained with a one-coil configuration which shows several rotations where providing a rectified voltage is not possible.

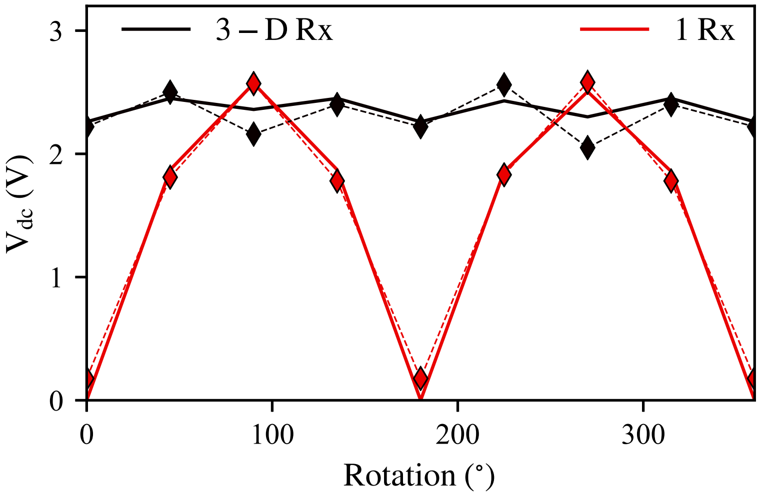

Figure 3.5: Rectified output voltage obtained by a system with one Rx coil (red) and by the proposed solution (black). The distance d is 5 cm, diamonds represent measurements. $V_s = 10\,\text{V}$.

On the other hand, the proposed 3-D Rx configuration results in a limited voltage variation (less than 20%) with values always above 2 V, therefore sufficient to power an implant in every rotation.

In fig. 3.6 the overall efficiency η_{TOT} is tested over rotation, for various distances (d), and defined as:

$$\eta_{\text{TOT}} = \eta_{\text{RF-RF}} * \eta_{\text{RF-dc}} = \frac{P_{\text{dc}}}{P_{\text{in}}}, \tag{3.1}$$

with:

$$\eta_{\text{RF-RF}} = \frac{P_{\text{Rx}_1} + P_{\text{Rx}_2}}{P_{\text{in}}}, \tag{3.2}$$

$$\eta_{\mathrm{RF-dc}} = \frac{P_{\mathrm{dc}}}{P_{\mathrm{Rx_1}} + P_{\mathrm{Rx_2}}}. \tag{3.3}$$

and

$$P_{\mathrm{Rx_i}} = \mathrm{Re}\left\{\frac{v_{\mathrm{Rx_i}} i^*_{\mathrm{Rx_i}}}{2}\right\} \text{ with } i = 1, 2. \tag{3.4}$$

where P_{in} is the RF power entering the Tx coil and P_{dc} is the power

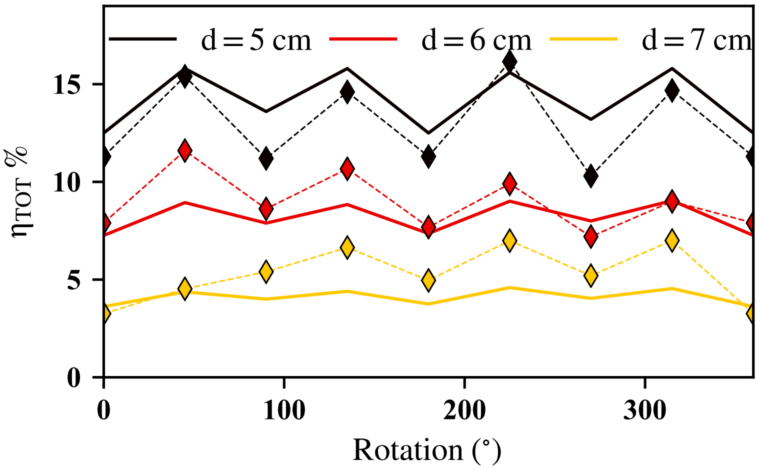

Figure 3.6: η_{TOT} predicted and measured for increasing Tx-Rx distances: diamonds are measurements ($V_s = 10\,\mathrm{V}$).

delivered to the Rx load. As the distance increases, the efficiency decreases since the coupling coefficient decreases, but the variability with rotation is limited.

Finally the system efficiency, varying V_{in}, is tested and the results are summarized in fig. 3.7, where the predicted and measured η_{TOT} are plotted for a 45 deg Rx rotation: better performances are obtained once V_{in} is well above the diodes threshold ($\sim 1\,\mathrm{V}$). At lower levels of the source, η_{RF-RF} is low because the rectifiers input impedances are far from the designed one. While at higher levels of the source, the rectifiers input impedance does not change significantly and the efficiency is maximized, according to kQ [34].

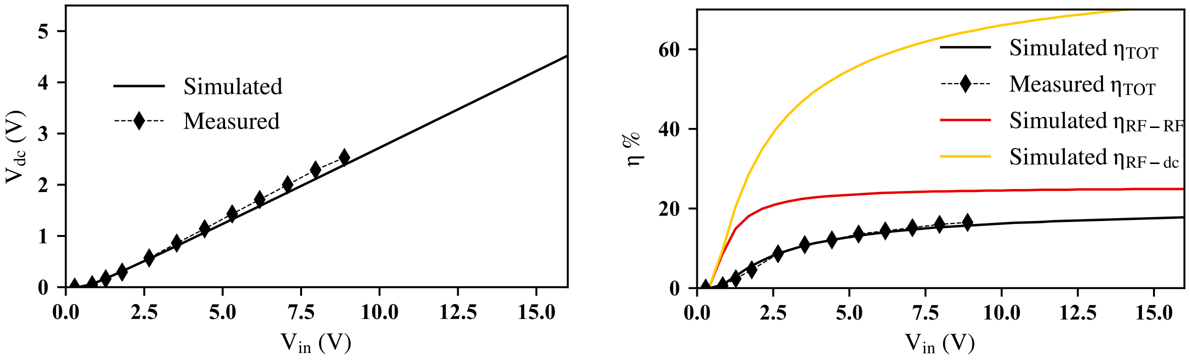

Figure 3.7: Left side, simulated and measured V_{dc} for different V_{in}, right side, η_{TOT}, η_{RF-RF} and η_{RF-dc} for different V_{in} at 45° and $d = 5\,\text{cm}$.

3.2 Rotation Insensitive IPT on Two Axes

In the previous section, the stabilization of the output voltage for a rotation in a 2-D plane was demonstrated, but the same principle can be applied to rotations in a 3-D space.

In this section, we describe the extension of the system is extended to be insensitive of each rotation around its center, therefore on both azimuthal and polar angle. To improve the efficiency with a reduced size, the system operates at 13.56 MHz. The volume of the receiver is in the order of a cubic centimeter, with a ball-like shape (see fig. 3.8) and composed of three orthogonal coils.

A large transmitter is geometrically optimized to maximize the shared flux in the direction of the miniaturized Rx receiver axis and at the distance of 5 cm, similarly to the previous section, but 3D printed, as in fig. 3.8. By full-wave EM simulation, during which the RX position has been varied by rotating the receiver around the three orthogonal axes, different sets of RF-to-RF links are calculated. The full exploitation of the 3-D Rx rotations highlights several θ-ϕ combinations, as in fig. 3.9. The equivalent circuit parameters of fig. 3.10 are derived and the coupling coefficients are listed in table 3.3 and table 3.4 for $\theta = 45°$ and $\theta = 60°$, respectively. Although the self-inductances do not vary, the coupling coefficients clearly

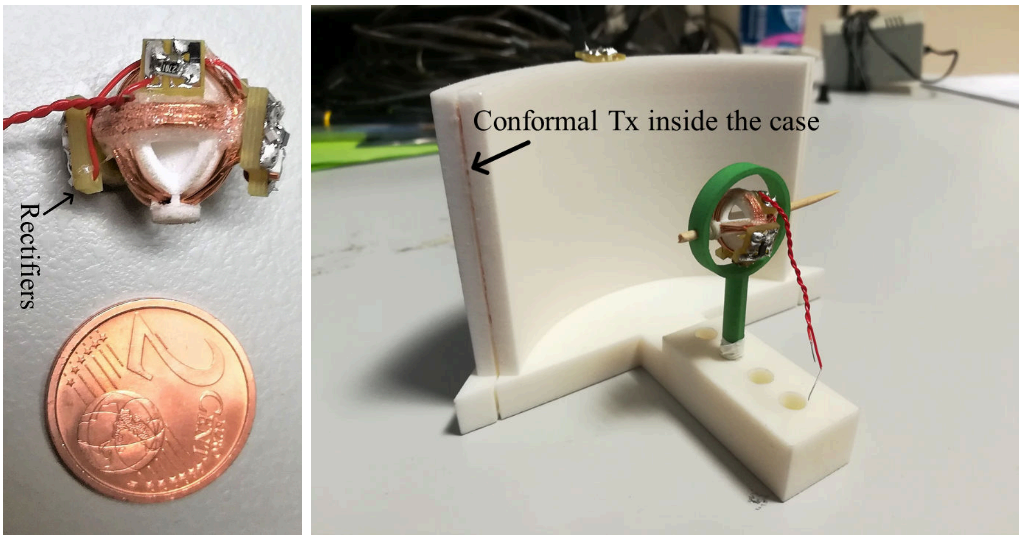

Figure 3.8: Left side, miniaturized receiver compared to a 2 euro cent coin, right side, picture of the realized prototype with the 3-D printed hosting setup.

show significant different operating conditions. This behaviour is overcome by the proposed 3-D structure and the rectifiers topologies, which guarantee an almost constant overall Tx-to-Rx coupling, regardless the Tx and Rx reciprocal orientation.

Table 3.3: Equivalent circuit parameters of the RF-to-RF link at θ= 45°, for various ϕ.

ϕ	k_{12}	k_{13}	k_{14}
0	-5.05×10^{-3}	-4.82×10^{-6}	-4.95×10^{-3}
45	-3.48×10^{-3}	-5.09×10^{-3}	-3.48×10^{-3}
90	3.19×10^{-6}	-0.707×10^{-2}	1.00×10^{-5}
135	3.48×10^{-3}	-4.82×10^{-3}	3.59×10^{-3}
180	5.04×10^{-3}	1.94×10^{-6}	5.14×10^{-3}
225	3.62×10^{-3}	4.97×10^{-3}	4.97×10^{-3}
270	-5.09×10^{-6}	0.71×10^{-2}	-0.83×10^{-6}
315	-3.61×10^{-3}	5.09×10^{-3}	-3.53×10^{-3}

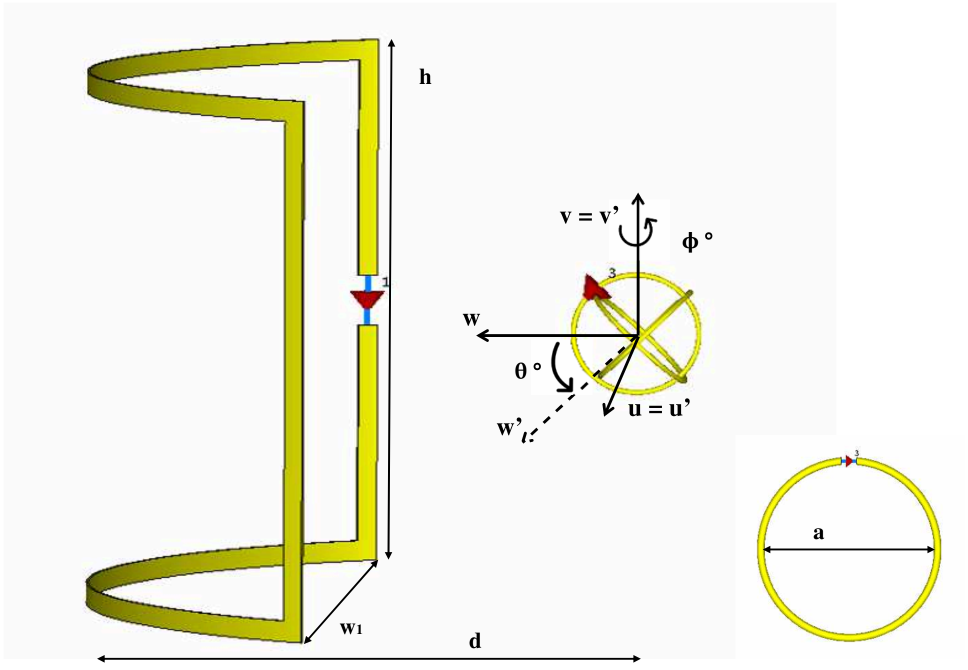

Figure 3.9: Rotation angles θ-ϕ. The Tx dimensions are: $h = 52\,\text{mm}$, $w_1 = 100\,\text{mm}$. The Rx coil dimensions are: $a = 12\,\text{mm}$ and the operating distance is $d = 50\,\text{mm}$. Single-loop receiving coils are displayed only for visualization purposes, to enable a clearer description of the angles.

The receiver consists of three orthogonal coils wrapped around a plastic sphere, which acts as the capsule; each coil is connected to its own optimized class-E rectifier and the three dc outputs are series-connected, see fig. 3.10. For this version of the prototype the rectifiers are mounted on pcb and glued on the coils. In the ultimate version the circuitry would be hosted inside the sphere.

A proper receiver topology can be realized by connecting each Rx coil with its own rectifier and then connecting the dc outputs in series. With this approach, the output voltage dark-zones are avoided and fluctuations are strongly reduced. The RF-to-dc conversion is performed by a Class-E

Table 3.4: Equivalent circuit parameters of the RF-to-RF link at θ= 60°, for various ϕ

ϕ	k_{12}	k_{13}	k_{14}
0	3.58×10^{-3}	-5.22×10^{-6}	-6.03×10^{-3}
45	-2.48×10^{-3}	-5.12×10^{-3}	-4.32×10^{-3}
90	1.84×10^{-6}	-0.71×10^{-2}	0.924×10^{-5}
135	2.50×10^{-3}	-4.94×10^{-3}	4.41×10^{-3}
180	3.60×10^{-3}	-1.00×10^{-5}	6.26×10^{-3}
225	2.54×10^{-3}	4.96×10^{-3}	4.41×10^{-3}
270	-4.36×10^{-6}	0.71×10^{-2}	6.75×10^{-7}
315	-2.58×10^{-3}	5.16×10^{-3}	-4.32×10^{-3}

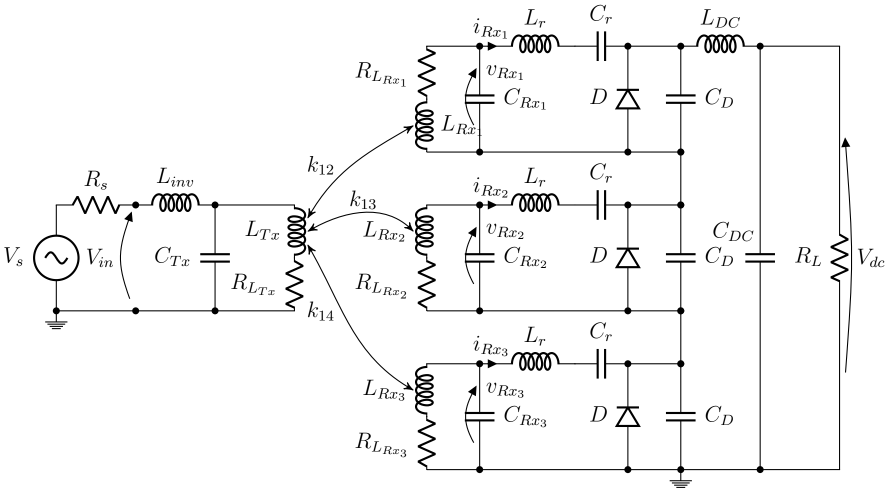

Figure 3.10: Circuit equivalent of the RF-to-dc link.

rectifier, shown in fig. 3.10, connected to each receiving coil through a LC filter, which ensures a sinusoidal input current. The three outputs are then dc-combined and share the same dc filter, where the inductance L_{DC} provides also a high RF impedance of the dc-combining path. This allows to separate the PCBs of the three rectifiers and thus to freely position the dc filter, without any unwanted spurious RF coupling from the dc line. The equivalent circuit of the transmitter consists in a $50\,\Omega$ voltage source,

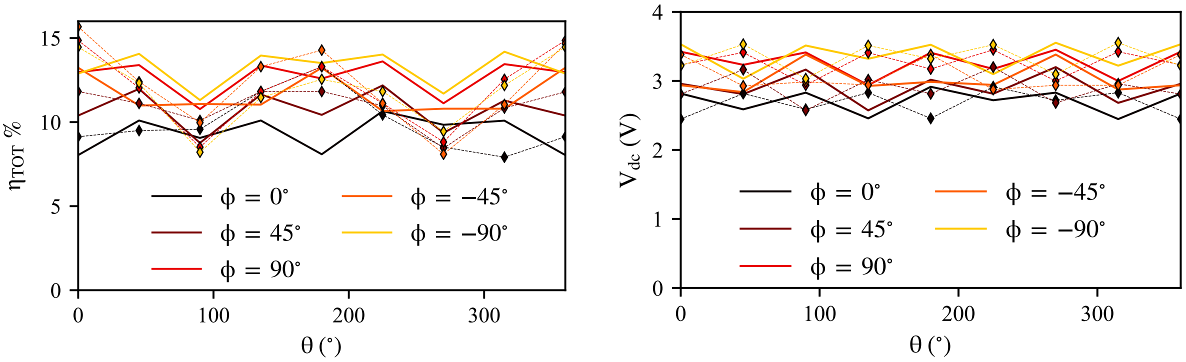

Figure 3.11: Left side, total efficiency (η_{TOT}), right side, output dc voltage (V_{dc}). Both are relative to $V_s = 10\,\mathrm{V}$. The measured data are included using diamonds.

linked to the resonant Tx coil through the inductance L_{inv}: in this way, the RF-to-RF link acts as a transformer, thus obtaining the source load proportional to the system load. This solution is suitable for sources with high internal series resistance, as in the case of low-power devices powering.

The three identical rectifiers are optimized, by means of the Harmonic Balance technique, embedded in the rest of the WPT system, thus accounting for the actual termination impedances. The nonlinear regime is described with 7 harmonics (plus dc), with the goals of maximizing the total efficiency (see eq. (3.5)) and of minimizing the output voltage (V_{dc}) variations for any possible angle. The optimization variables are C_D and the dc-load R_L, which resulted to be 10 pF and 2.7 kΩ, respectively. Finally, several voltage source amplitudes are considered to analyze the dynamic behaviour of the proposed design.

3.2.1 Simulated and Measured Results

An early prototype is designed as shown in fig. 3.8. The three-loop coils are wrapped around three 3D-printed orthogonal disks which are able to rotate around the 3 axis through a Cardan suspension. The optimized components are listed in table 3.5.

Table 3.5: Optimized components values

L_{inv}	140 nH	C_{Rx_3}	890 pF	f	13.56 MHz
$R_{L_{inv}}$	26 mΩ	$R_{L_{Tx}}$	200 mΩ	D	HSMS-2822
L_{Tx}	322 nH	$R_{L_{Rx_1}}$	100 mΩ	C_D	10 pF
C_{Tx}	430 pF	$R_{L_{Rx_2}}$	100 mΩ	L_{DC}	22 µH
L_{Rx_1}	155 nH	$R_{L_{Rx_3}}$	100 mΩ	$R_{L_{DC}}$	20 mΩ
L_{Rx_2}	155 nH	L_r	140 nH	C_{DC}	20 µF
L_{Rx_3}	155 nH	R_{L_r}	20 mΩ	R_L	2700 Ω
C_{Rx_1}	890 pF	C_r	1 nF	R_s	50 Ω
C_{Rx_2}	890 pF				

The results confirm that the proposed solution allows to remotely provide at least 2.7 V on every orientation, with 10 V in input, at 5 cm on an optimum load of 2700 Ohm, corresponding to a dc-power of 2.5 mW. These values are fully compatible with state-of-the-art implantable devices needs of power and turn-on voltage. The prototype and first experimental validations are provided.

In fig. 3.11 the overall efficiency η_{TOT} is plotted for various θ-ϕ rotations and computed starting from the simulated results and defined as as before but with:

$$\eta_{RF-RF} = \frac{P_{Rx_1} + P_{Rx_2} + P_{Rx_3}}{P_{in}}, \tag{3.5}$$

$$\eta_{RF-dc} = \frac{P_{dc}}{P_{Rx_1} + P_{Rx_2} + P_{Rx_3}}. \tag{3.6}$$

and

$$P_{Rx_i} = \mathrm{Re}\left\{\frac{v_{Rx_i} i^*_{Rx_i}}{2}\right\} \text{ with } i = 1, 2, 3. \tag{3.7}$$

where P_{in} is the RF power entering the Tx coil, which is always around 20 mW, and P_{dc} is the power delivered to the Rx load. Figure 3.11 shows the corresponding dc output voltage for any possible azimuthal and longitudinal rotations.

Finally, fig. 3.12 considers a reference RX configuration, with $(\theta, \phi) = (45°, 45°)$ and the efficiency obtained by varying the V_{in} is plotted: when V_{in} is above the diodes threshold ($\sim$ 1.5 V) the performances strongly

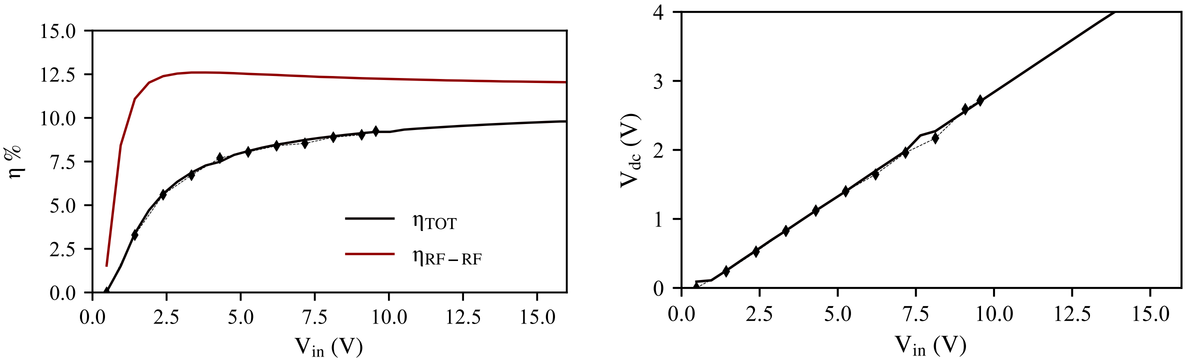

Figure 3.12: Left side, simulated (lines) and measured (dots) η_{RF-RF} and η_{TOT}, right side, simulated and measured output dc voltage (V_{dc}). Both are obtained for different V_{in} at $(\theta, \phi) = (45°, 45°)$ and $d = 5\,\text{cm}$.

improve, while if it exceeds 10 V the improvements are reduced due to the diodes nonlinear behaviour. For very low voltage source values, the η_{TOT} degradation is unavoidable, since the rectifiers input impedances are far from the optimum ones. On the other hand, when higher source voltages are provided, the rectifiers input impedance has no significant variations and the efficiency is maximized, according to kQ [34]. In the same figures the preliminary measurement results are superimposed and compared with the predicted ones, confirming the accuracy of the design procedure.

3.3 Remarks

- A omni-directional IPT solution for body implants is proposed;
- The link maintains a consistent output voltage over 2 V, independent of the rotation of the implant;
- Sufficient efficiency is obtained for couplings under 1%:
    - The transmitter uses a conformal shape to maximize the shared flux for the designed receiver and at the designed distance;

  - The optimized class E rectifier provides a RF-to-dc conversion efficiency over 60%;
  - Increasing the frequency and the number of turns increases the quality factor of the coils and therefore the efficiency of the link;
  - Increasing the number of turns of the receiver increases also the output voltage, potentially increasing the RF-to-dc conversion efficiency;

- The system can be a safe and less invasive alternative to the replacement of batteries through surgery.

Chapter 4

Conclusions

"All truths are easy to understand once they are discovered;
the point is to discover them."

- Galileo Galilei -

This thesis demonstrates a framework for the modelling, analysis and design of a complete energy and data transfer system, which provides constant performances independently of the receiver position.

The first part is dedicated to industrial sliders, systems that move in one direction and need to be powered along the path.

First, the RF-to-RF link, consisting of an array of Tx coils and a moving Rx coil, is geometrically optimized, proving that there is a length of the receiving coil that maintains the same coupling coefficient, which requires the two transmitters to be simultaneously powered and connected in series.

Initially, the series connection is performed using solid state relays, resulting in a solution limited to low frequencies due to stray resonance introduced by the parasitics in the switches. Using mechanical relays could be a viable option for very high power needs.

The alternative is the virtual connection, which consists in feeding each transmitting coil with an independent current source implemented through a Coupled Load Independent Inverter. The advantage of this method is that the length of the path is theoretically unlimited, because each current source is fed in dc. Furthermore, the parasitics of the switch are included in the design of the inverter and the maximum frequency is limited only by the characteristics of the device and its driver. Last but not least, it provides higher efficiency and requires only two quadrant devices.

For this virtual series, which proved to be the best solution in the MHz frequency range, a Class E rectifier, built around the optimized receiving coil, is designed and embedded in the entire system to reflect a quasi-resistive RF load to the inverter while providing constant output voltage.

The result is an optimized and fully modular dc-to-dc WPT system, capable of operating for several different Rx loading conditions and positions, which can be lengthened or shortened according to the specific application, without any need for further design efforts. With a dc input voltage of 70 V, the dc-to-dc efficiency is 80% and the dc output power is 100 W. An additional benefit of the load independent inverter is the possibility to passively retrieve the position of the receiver, useful for activating the proper couple of inverters.

A high throughput data transfer link, capable of maintain 100Mb/s independently of the position, is finally designed around cheap consumer hardware. Taking advantage of the coil structure and the reduced distance, the data-link is demonstrated to provide high resistance to interference and noise margin. The data link was included in a network topology which allows to each device full network access.

The entire data and power system is designed as being fully modular, where each module is identical and repeated, without any reasonable limit on the maximum length and therefore high flexibility.

The second part was dedicated to medical implants and focused to minimize the output voltage variations due to a rotation on both axes. The proposed system was able to maintain an almost constant output voltage, above 2.5 V, and efficiency, around 10%, with coupling below 1% and a 10 V input source.

References

[1] A. Pacini, A. Costanzo, S. Aldhaher, and P. D. Mitcheson, "Load- and Position-Independent Moving MHz WPT System Based on GaN-Distributed Current Sources", *IEEE Transactions on Microwave Theory and Techniques*, vol. 65, no. 12, pp. 5367–5376, 2017. DOI: `10.1109/tmtt.2017.2768031`.

[2] A. Pacini, F. Mastri, R. Trevisan, D. Masotti, and A. Costanzo, "Geometry Optimization of Sliding Inductive Links for Position-Independent Wireless Power Transfer", in *2016 IEEE International Microwave Symposium*, Institute of Electrical & Electronics Engineers (IEEE), 2016. DOI: `10.1109/mwsym.2016.7540073`.

[3] A. Pacini, F. Mastri, R. Trevisan, A. Costanzo, and D. Masotti, "Theoretical and Experimental Characterization of Moving Wireless Power Transfer Systems", in *2016 10th European Conference on Antennas and Propagation (EuCAP)*, Institute of Electrical and Electronics Engineers (IEEE), 2016, pp. 1–4. DOI: `10.1109/eucap.2016.7481913`.

[4] A. Pacini, F. Mastri, D. Masotti, and A. Costanzo, "Criticality Mitigation in a Quasi-Constant Coupling Position Independent Resonant IPT Network", *International Journal of Microwave and Wireless Technologies*, pp. 1–10, 2018. DOI: `10.1017/S1759078718000788`.

[5] A. Pacini, A. Costanzo, S. Aldhaher, and P. D. Mitcheson, "Design of a Position-Independent End-to-End Inductive WPT Link for Industrial Dynamic Systems", in *2017 IEEE MTT-S International Microwave Symposium (IMS)*, 2017, pp. 1053–1056. DOI: `10.1109/MWSYM.2017.8058774`.

[6] A. Pacini, F. Benassi, D. Masotti, and A. Costanzo, "Design of a RF-to-dc Link for in-body IR-WPT with a Capsule-shaped Rotation-insensitive Receiver", in *2018 IEEE MTT-S International Microwave Symposium (IMS)*, 2018, pp. 1289–1292. DOI: `10.1109/MWSYM.2018.8439499`.

[7] A. Pacini, F. Benassi, D. Masotti, and A. Costanzo, "Design of a Miniaturized Omni-Directional RF-to-dc IR-WPT", in *2018 IEEE Wireless Power Transfer Conference (WPTC)*, 2018. DOI: `InPress`.

[8] D. Schneider, "Wireless power at a distance is still far away [electrons unplugged]", *IEEE Spectrum*, vol. 47, no. 5, pp. 34–39, May 2010. DOI: `10.1109/mspec.2010.5453139`.

[9] M. G. L. Roes, J. L. Duarte, M. A. M. Hendrix, and E. A. Lomonova, "Acoustic energy transfer: A review", *IEEE Transactions on Industrial Electronics*, vol. 60, no. 1, pp. 242–248, Jan. 2013. DOI: `10.1109/tie.2012.2202362`.

[10] M. Kazmierkowski and A. Moradewicz, "Unplugged but connected: Review of contactless energy transfer systems", *IEEE Industrial Electronics Magazine*, vol. 6, no. 4, pp. 47–55, Dec. 2012. DOI: `10.1109/mie.2012.2220869`.

[11] S. Sasaki, K. Tanaka, and K.-i. Maki, "Microwave Power Transmission Technologies for Solar Power Satellites", *Proceedings of the IEEE*, vol. 101, no. 6, pp. 1438–1447, Jun. 2013. DOI: `10.1109/jproc.2013.2246851`.

[12] Z. Popovic, E. A. Falkenstein, D. Costinett, and R. Zane, "Low-Power Far-Field Wireless Powering for Wireless Sensors", *Proceedings of the IEEE*, vol. 101, no. 6, pp. 1397–1409, Jun. 2013. DOI: `10.1109/jproc.2013.2244053`.

[13] H. J. Visser and R. J. M. Vullers, "RF Energy Harvesting and Transport for Wireless Sensor Network Applications: Principles and Requirements", *Proceedings of the IEEE*, vol. 101, no. 6, pp. 1410–1423, Jun. 2013. DOI: `10.1109/JPROC.2013.2250891`.

[14] B. Strassner and K. Chang, "Microwave Power Transmission: Historical Milestones and System Components", *Proceedings of the IEEE*, vol. 101, no. 6, pp. 1379–1396, Jun. 2013. DOI: `10.1109/jproc.2013.2246132`.

[15] K. Wu, D. Choudhury, and H. Matsumoto, "Wireless Power Transmission, Technology, and Applications [Scanning the Issue]", *Proceedings of the IEEE*, vol. 101, no. 6, pp. 1271–1275, Jun. 2013. DOI: `10.1109/jproc.2013.2257590`.

[16] J. Garnica, R. A. Chinga, and J. Lin, "Wireless Power Transmission: From Far Field to Near Field", *Proceedings of the IEEE*, vol. 101, no. 6, pp. 1321–1331, Jun. 2013. DOI: `10.1109/jproc.2013.2251411`.

[17] S. Dunbar and Z. Popović, "Low-power electronics for energy harvesting sensors", *Wireless Power Transfer*, vol. 1, no. 01, pp. 35–43, 2014. DOI: `10.1017/wpt.2014.5`.

[18] C. R. Valenta and G. D. Durgin, "Harvesting wireless power: Survey of energy-harvester conversion efficiency in far-field, wireless power transfer systems", *IEEE Microwave Mag.*, vol. 15, no. 4, pp. 108–120, 2014. DOI: `10.1109/MMM.2014.2309499`.

[19] J. S. Ho, S. Kim, and A. S. Y. Poon, "Midfield wireless powering for implantable systems", *Proceedings of the IEEE*, vol. 101, no. 6, pp. 1369–1378, Jun. 2013. DOI: `10.1109/jproc.2013.2251851`.

[20] A. Kurs, A. Karalis, R. Moffatt, J. D. Joannopoulos, P. Fisher, and M. Soljacic, "Wireless power transfer via strongly coupled magnetic resonances", *Science*, vol. 317, no. 5834, pp. 83–86, Jul. 2007. DOI: `10.1126/science.1143254`.

[21] N. Tesla, *Apparatus for transmitting electrical energy.* US Patent 1,119,732, Dec. 1914.

[22] J. T. Boys and G. A. Covic, "The Inductive Power Transfer Story at the University of Auckland", *IEEE Circuits and Systems Magazine*, vol. 15, no. 2, pp. 6–27, 2015. DOI: `10.1109/mcas.2015.2418972`.

[23] G. Covic and J. Boys, "Inductive Power Transfer", *Proc. IEEE*, vol. 101, no. 6, pp. 1276–1289, 2013. DOI: `10.1109/JPROC.2013.2244536`.

[24] J. Bolger, F. Kirsten, and L. Ng, "Inductive power coupling for an electric highway system", in *28th IEEE Vehicular Technology Conference*, IEEE, 1978. DOI: `10.1109/vtc.1978.1622522`.

[25] C. Zell and J. Bolger, "Development of an engineering prototype of a roadway powered electric transit vehicle system: A public/private sector program", in *32nd IEEE Vehicular Technology Conference*, IEEE, 1982. DOI: `10.1109/vtc.1982.1623054`.

[26] W. Loh and A. Renfrew, "Optimised microelectronic power control of an AC drive for an electric vehicle", *IEE Proceedings B Electric Power Applications*, vol. 133, no. 4, p. 291, 1986. DOI: `10.1049/ip-b.1986.0039`.

[27] M. Eghtesadi, "Inductive power transfer to an electric vehicle-analytical model", in *40th IEEE Conference on Vehicular Technology*, IEEE, 1990. DOI: `10.1109/vetec.1990.110303`.

[28] J. Bolger, "Urban electric transportation systems: The role of magnetic power transfer", in *Proceedings of WESCON '94*, IEEE, 1994. DOI: `10.1109/wescon.1994.403598`.

[29] Y. Jang and M. Jovanovic, "A contactless electrical energy transmission system for portable-telephone battery chargers", in *INTELEC. Twenty-Second International Telecommunications Energy Conference (Cat. No.00CH37131)*, IEEE, 1986. DOI: `10.1109/intlec.2000.884329`.

[30] A. Green, "10 kHz inductively coupled power transfer - concept and control", in *Proceedings of 5th International Conference on Power Electronics and Variable-Speed Drives*, IEE, 1994. DOI: `10.1049/cp:19941049`.

[31] O. Stielau and G. Covic, "Design of loosely coupled inductive power transfer systems", in *PowerCon 2000. 2000 International Conference on Power System Technology. Proceedings (Cat. No.00EX409)*, IEEE, 2000. DOI: `10.1109/icpst.2000.900036`.

[32] C.-s. Wang, G. A. Covic, and O. H. Stielau, "Power Transfer Capability and Bifurcation Phenomena of Loosely Coupled Inductive Power Transfer Systems", *IEEE Transactions on Industrial Electronics*, vol. 51, no. 1, pp. 148–157, 2004. DOI: `10.1109/TIE.2003.822038`.

[33] J. D. Crawford, "Introduction to bifurcation theory", *Reviews of Modern Physics*, vol. 63, no. 4, pp. 991–1037, Oct. 1991. DOI: `10.1103/revmodphys.63.991`.

[34] K. V. Schuylenbergh and R. Puers, *Inductive Powering: Basic Theory and Application to Biomedical Systems.* Springer, 2009.

[35] M. Pinuela, D. C. Yates, S. Lucyszyn, and P. D. Mitcheson, "Maximizing DC-to-load efficiency for inductive power transfer", *IEEE Transactions on Power Electronics*, vol. 28, no. 5, pp. 2437–2447, May 2013. DOI: `10.1109/tpel.2012.2215887`.

[36] S. Y. R. Hui, W. Zhong, and C. K. Lee, "A critical review of recent progress in mid-range wireless power transfer", *IEEE Transactions on Power Electronics*, vol. 29, no. 9, pp. 4500–4511, Sep. 2014. DOI: `10.1109/tpel.2013.2249670`.

[37] S. Li, W. Li, J. Deng, T. D. Nguyen, and C. C. Mi, "A double-sided LCC compensation network and its tuning method for wireless power transfer", *IEEE Transactions on Vehicular Technology*, vol. 64, no. 6, pp. 2261–2273, Jun. 2015. DOI: `10.1109/TVT.2014.2347006`.

[38] S. Li and C. C. Mi, "Wireless power transfer for electric vehicle applications", *IEEE Journal of Emerging and Selected Topics in Power Electronics*, vol. 3, no. 1, pp. 4–17, Mar. 2015. DOI: `10.1109/jestpe.2014.2319453`.

[39] R. Bosshard and J. W. Kolar, "Inductive power transfer for electric vehicle charging: Technical challenges and tradeoffs", *IEEE Power Electronics Magazine*, vol. 3, no. 3, pp. 22–30, Sep. 2016. DOI: `10.1109/mpel.2016.2583839`.

[40] D. Patil, M. K. McDonough, J. M. Miller, B. Fahimi, and P. T. Balsara, "Wireless power transfer for vehicular applications: Overview and challenges", *IEEE Transactions on Transportation Electrification*, vol. 4, no. 1, pp. 3–37, Mar. 2018. DOI: `10.1109/tte.2017.2780627`.

[41] Z. Zhang, H. Pang, A. Georgiadis, and C. Cecati, "Wireless power transfer—an overview", *IEEE Transactions on Industrial Electronics*, vol. 66, no. 2, pp. 1044–1058, Feb. 2019. DOI: `10.1109/tie.2018.2835378`.

[42] S. C. Cripps, *RF Power Amplifiers for Wireless Communications, Second Edition*. Norwood, MA, USA: Artech House, Inc., 2006, ISBN: 1596930187.

[43] Y. H. Sohn, B. H. Choi, E. S. Lee, G. C. Lim, G.-H. Cho, and C. T. Rim, "General unified analyses of two-capacitor inductive power transfer systems: Equivalence of current-source SS and SP compensations", *IEEE Transactions on Power Electronics*, vol. 30, no. 11, pp. 6030–6045, Nov. 2015. DOI: `10.1109/tpel.2015.2409734`.

[44] T. Ohira, "The kQ product as viewed by an analog circuit engineer", *IEEE Circuits and Systems Magazine*, vol. 17, no. 1, pp. 27–32, 2017. DOI: `10.1109/mcas.2016.2642698`.

[45] S. M. Mikki and Y. M. M. Antar, "A theory of antenna electromagnetic near field - part i", *IEEE Transactions on Antennas and Propagation*, vol. 59, no. 12, pp. 4691–4705, Dec. 2011. DOI: `10.1109/tap.2011.2165499`.

[46] S. M. Mikki and Y. M. M. Antar, "A Theory of Antenna Electromagnetic Near Field - Part II", *IEEE Trans. Antennas Propag.*, vol. 59, no. 12, pp. 4706–4724, Dec. 2011. DOI: `10.1109/TAP.2011.2165500`.

[47] L. Chen, S. Liu, Y. C. Zhou, and T. J. Cui, "An Optimizable Circuit Structure for High-Efficiency Wireless Power Transfer", *IEEE Transactions on Industrial Electronics*, vol. 60, no. 1, pp. 339–349, Jan. 2013. DOI: `10.1109/tie.2011.2179275`.

[48] N. Sokal and A. Sokal, “Class E - A new class of high-efficiency tuned single-ended switching power amplifiers”, *IEEE Journal of Solid-State Circuits*, vol. 10, no. 3, pp. 168–176, Jun. 1975. DOI: `10.1109/jssc.1975.1050582`.

[49] M. K. Kazimierczuk and D. Czarkowski, *Resonant Power Converters*, 2nd ed. Hoboken, N.J: John Wiley & Sons, 2012, ISBN: 978-0-470-90538-8.

[50] F. H. Raab, “Idealized Operation of the Class E Tuned Power Amplifier”, *IEEE Transactions on Circuits and Systems*, vol. 24, no. 12, pp. 725–735, 1977. DOI: `10.1109/TCS.1977.1084296`.

[51] F. H. Raab, P. Asbeck, S. Cripps, P. B. Kenington, Z. B. Popović, N. Pothecary, J. F. Sevic, and N. O. Sokal, “Power amplifiers and transmitters for RF and microwave”, *IEEE Transactions on Microwave Theory and Techniques*, vol. 50, no. 3, pp. 814–826, 2002. DOI: `10.1109/22.989965`.

[52] M. Kazimierczuk and K. Puczko, “Exact analysis of class E tuned power amplifier at any Q and switch duty cycle”, *IEEE Transactions on Circuits and Systems*, vol. 34, no. 2, pp. 149–159, 1987, ISSN: 0098-4094. DOI: `10.1109/TCS.1987.1086114`.

[53] S. Aldhaher, D. C. Yates, and P. D. Mitcheson, “Modeling and Analysis of Class EF and Class E/F Inverters With Series-Tuned Resonant Networks”, *IEEE Transactions on Power Electronics*, vol. 31, no. 5, pp. 3415–3430, May 2016.

[54] S. Aldhaher, D. C. Yates, and P. D. Mitcheson, “Load-Independent Class E/EF Inverters and Rectifiers for MHz-Switching Applications”, *IEEE Transactions on Power Electronics*, 2018. DOI: `10.1109/TPEL.2018.2813760`.

[55] U. Mishra, P. Parikh, and Y.-F. Wu, “AlGaN/GaN HEMTs - An overview of device operation and applications”, *Proceedings of the IEEE*, vol. 90, no. 6, pp. 1022–1031, Jun. 2002. DOI: `10.1109/jproc.2002.1021567`.

[56] B. Baliga, *Wide Bandgap Semiconductor Power Devices: Materials, Physics, Design, and Applications*. Elsevier Science, 2018, ISBN: 9780081023075.

[57] W. Liu, *Fundamentals of III-V Devices: HBTs, MESFETs, and HFETs/HEMTs*. Wiley, 1999, ISBN: 9780471297000.

[58] M. Meneghini, G. Meneghesso, and E. Zanoni, *Power GaN Devices: Materials, Applications and Reliability*. Springer International Publishing, 2016, ISBN: 9783319431994.

[59] G. Meneghesso, M. Meneghini, and E. Zanoni, *Gallium Nitride-enabled High Frequency and High Efficiency Power Conversion*. Springer International Publishing, 2018, ISBN: 9783319779942.

[60] F. Medjdoub, *Gallium Nitride (GaN): Physics, Devices, and Technology*. Taylor & Francis, 2015, ISBN: 9781482220032.

[61] B. R. Nag, *Physics of Quantum Well Devices*. Kluwer Academic Publishers, 2002. DOI: `10.1007/0-306-47127-2`.

[62] G. Meneghesso, M. Meneghini, and E. Zanoni, “Breakdown mechanisms in AlGaN/GaN HEMTs: An overview”, *Japanese Journal of Applied Physics*, vol. 53, no. 10, p. 100 211, Sep. 2014. DOI: `10.7567/jjap.53.100211`.

[63] X.-G. He, D.-G. Zhao, and D.-S. Jiang, “Formation of two-dimensional electron gas at AlGaN/GaN heterostructure and the derivation of its sheet density expression”, *Chinese Physics B*, vol. 24, no. 6, p. 067 301, Jun. 2015. DOI: `10.1088/1674-1056/24/6/067301`.

[64] B. Baliga, *Fundamentals of power semiconductor devices*. Springer, 2019, ISBN: 978-3-319-93988-9.

[65] Y. Hongyu, *Gallium Nitride Power Devices*, 1st ed. Pan Stanford Publishing, 2017, ISBN: 9789814774093.

[66] E. Bahat-Treidel, “GaN Based HEMTs for High Voltage Operation. Design, Technology and Characterization”, PhD thesis, Technische Universität Berlin, 2012. DOI: `10.14279/depositonce-3203`.

[67] B. J. Baliga, “Semiconductors for high-voltage, vertical channel field-effect transistors”, *Journal of Applied Physics*, vol. 53, no. 3, pp. 1759–1764, Mar. 1982. DOI: `10.1063/1.331646`.

[68] B. Baliga, “Power semiconductor device figure of merit for high-frequency applications”, *IEEE Electron Device Letters*, vol. 10, no. 10, pp. 455–457, Oct. 1989. DOI: `10.1109/55.43098`.

[69] J. P. C. Smeets, T. T. Overboom, J. W. Jansen, and E. A. Lomonova, “Comparison of position-independent contactless energy transfer systems”, *IEEE Transactions on Power Electronics*, vol. 28, no. 4, pp. 2059–2067, Apr. 2013. DOI: `10.1109/tpel.2012.2205404`.

[70] R. E. Collin, *Foundations for Microwave Engineering*, 2nd ed. Wiley-IEEE Press, Jan. 2001.

[71] Vishay VO14642A, `https://www.vishay.com/docs/81646/vo14642a.pdf`, (visited on 31/01/2019).

[72] *ADS advanced design system 2015*, `keysight.com`, Keysight Technologies.

[73] S. Aldhaher, P. D. Mitcheson, and D. C. Yates, “Load-independent Class EF inverters for inductive wireless power transfer”, in *2016 IEEE Wireless Power Transfer Conference (WPTC)*, May 2016, pp. 1–4, ISBN: 9781467379861. DOI: `10.1109/WPT.2016.7498864`.

[74] S. Aldhaher, D. C. Yates, and P. D. Mitcheson, “Design and Development of a Class EF2 Inverter and Rectifier for Multimegahertz Wireless Power Transfer Systems”, *IEEE Transactions on Power Electronics*, vol. 31, no. 12, pp. 8138–8150, Dec. 2016, ISSN: 0885-8993. DOI: `10.1109/tpel.2016.2521060`.

[75] M. K. Kazimierczuk, “Analysis of Class E Zero-Voltage-Switching Rectifier”, *IEEE Transactions on Circuits and Systems*, vol. 37, no. 6, pp. 747–755, 1990, ISSN: 00984094. DOI: `10.1109/31.55033`.

[76] J. Jozwik and M. Kazimierczuk, “Analysis and design of Class-E2 DC/DC converter”, *IEEE Transactions on Industrial Electronics*, vol. 37, no. 2, pp. 173–183, Apr. 1990. DOI: `10.1109/41.52968`.

[77] J. A. Santiago-Gonzalez, K. M. Elbaggari, K. K. Afridi, and D. J. Perreault, “Design of Class E Resonant Rectifiers and Diode Evaluation for VHF Power Conversion”, *IEEE Transactions on Power Electronics*, vol. 30, no. 9, pp. 4960–4972, Sep. 2015. DOI: `10.1109/tpel.2015.2398848`.

[78] P. Grover and A. Sahai, “Shannon meets Tesla: Wireless information and power transfer”, in *2010 IEEE International Symposium on Information Theory*, IEEE, Jun. 2010. DOI: `10.1109/ISIT.2010.5513714`.

[79] R. Trevisan and A. Costanzo, “A UHF near-field link for passive sensing in industrial wireless power transfer systems”, *IEEE Transactions on Microwave Theory and Techniques*, vol. 64, no. 5, pp. 1634–1643, May 2016. DOI: `10.1109/tmtt.2016.2544317`.

[80] OpenWRT, `http://www.openwrt.org`, (visited on 28/01/2019).

[81] Blender, `https://www.blender.org/`, (visited on 28/01/2019).

[82] FreeCAD, `https://www.freecadweb.org/`, (visited on 28/01/2019).

[83] “IEEE Standard for Information technology – Telecommunications and information exchange between systems—Local and metropolitan area networks – Specific requirements – Part 11: Wireless LAN Medium Access Control (MAC) and Physical Layer (PHY) Specifications – Amendment 4: Enhancements for Very High Throughput for Operation in Bands below 6 GHz”, *IEEE 802.11ac-2013*, Table 22-25, 2013.

[84] Raspberry Pi3, `https://www.raspberrypi.org/products/raspberry-pi-3-model-b/`, (visited on 28/01/2019).

[85] K. Agarwal, R. Jegadeesan, Y.-X. Guo, and N. V. Thakor, “Wireless power transfer strategies for implantable bioelectronics: Methodological review”, *IEEE Reviews in Biomedical Engineering*, pp. 1–1, 2017. DOI: `10.1109/RBME.2017.2683520`.

[86] G. Joung and B. Cho, “An energy transmission system for an artificial heart using leakage inductance compensation of transcutaneous transformer”, in *PESC Record. 27th Annual IEEE Power Electronics Specialists Conference*, IEEE, 1996. DOI: `10.1109/pesc.1996.548688`.

[87] R.-F. Xue, K.-W. Cheng, and M. Je, “High-efficiency wireless power transfer for biomedical implants by optimal resonant load transformation”, *IEEE Transactions on Circuits and Systems I: Regular Papers*, vol. 60, no. 4, pp. 867–874, Apr. 2013. DOI: `10.1109/tcsi.2012.2209297`.

[88] C. Zhang, D. Lin, and S. Y. Hui, “Basic Control Principles of Omni-Directional Wireless Power Transfer”, *IEEE Transactions on Power Electronics*, pp. 1–1, 2015. DOI: `10.1109/tpel.2015.2479246`.

[89] D. Lin, C. Zhang, and S. Y. R. Hui, “Mathematical Analysis of Omnidirectional Wireless Power Transfer—Part-I: Two-Dimensional Systems”, *IEEE Transactions on Power Electronics*, vol. 32, no. 1, pp. 625–633, Jan. 2017. DOI: `10.1109/tpel.2016.2523500`.

[90] D. Lin, C. Zhang, and S. Y. R. Hui, “Mathematic Analysis of Omnidirectional Wireless Power Transfer—Part-II Three-Dimensional Systems”, *IEEE Transactions on Power Electronics*, vol. 32, no. 1, pp. 613–624, Jan. 2017. DOI: `10.1109/tpel.2016.2523506`.

[91] W. B. Kuhn and A. P. Boutz, “Measuring and Reporting High Quality Factors of Inductors Using Vector Network Analyzers”, *IEEE Transactions on Microwave Theory and Techniques*, vol. 58, no. 4, pp. 1046–1055, Apr. 2010. DOI: `10.1109/tmtt.2010.2042843`.

This page was intentionally left blank.

List of Figures